Dissertation

SUBMITTED TO THE

Combined Faculties of the Natural Sciences and Mathematics
of the Ruperto-Carola-University of Heidelberg, Germany

FOR THE DEGREE OF

Doctor of Natural Sciences

Put forward by

Helen Poon (潘凱琳)

Born in: Hong Kong

Oral examination: 03.02.2016

H.E.S.S. observations of Sgr A*

Referees: **Prof. Dr. Werner Hofmann**
Prof. Dr. Stefan Wagner

Zusammenfassung

Das Galaktische Zentrum wird seit über zehn Jahren mit dem High Energy Stereoscopic System (H.E.S.S.) untersucht und zeigt eine helle, komplexe Morphologie im Bereich der hochenergetischen Gammastrahlung. Neben einer starken Punktquelle an der Position des supermassiven Schwarzen Loches Sgr A* haben frühere Analysen eine diffuse Kante von Gammastrahlenemission entdeckt, was auf einen kraftvollen Beschleuniger kosmischer Strahlung in dieser Region hindeutet. Dies wurde ausführlich in verschiedenen Wellenlängen untersucht, wo dann auch Flares im Radio- und im Röntgenbereich beobachtet werden konnten, der Gammabereich aber stabil blieb. Eine Gaswolke namens G2 wurde 2011 dabei beobachtet, wie sie sich gradlinig auf das Galaktische Zentrum zubewegte. Es wurde angenommen, dass die Akkretionsrate steigen und dies zu Flares in verschiedenen Wellenbändern führen würde.

Das Hinzufügen eines fünften Teleskops mit 600 m^2 Spiegelfläche in das Zentrum der vier H.E.S.S.-Teleskope hat den zugänglichen Energiebereich erweitert, sodass Beobachtungen nun bis zu 100 GeV und niedriger durchgeführt werden können. Die Sensitivität wurde auch verbessert, wodurch nun hochenergetische Flares von dem Galaktischen Zentrum besser detektiert werden können. In dieser Arbeit wird eine Langzeitstudie von Sgr A* mit H.E.S.S.-I-Daten und Daten von H.E.S.S. II von der Zeit des Durchgangs des Perizentrums von G2 präsentiert. Variabilitätstests wurden auch durchgeführt, um nach transienten Ereignissen zu suchen. Das gesamte Spektrum und die Spektren einzelner Jahre sind über die Jahre stabil geblieben und die Ergebnisse der Variabilitätstest zeigen auch einen stabilen Fluss.

Abstract

The Galactic Centre has been studied with the High Energy Stereoscopic System (H.E.S.S.) for over 10 years, showing a bright, complex gamma-ray morphology. Other than a strong point-like very-high-energy gamma-ray source coincident with the supermassive black hole Sgr A*, previous analyses also revealed a diffuse ridge of gamma-ray emission, indicative of a powerful cosmic-ray accelerator in this region. It has been widely studied in the multiwavelength, exhibiting flares from radio to X-ray, but in the VHE regime it has always been stable. A gas cloud called G2 was found travelling straight to the Galactic Centre in 2011. Accretion rate was expected to increase which might possibly lead to flares in different wavebands.

The addition of a fifth telescope with 600 m^2 mirror area to the centre of the H.E.S.S. array has increased the energy range accessible, allowing observations to take place down to 100 GeV and potentially below. The sensitivity is also increased which means it has better ability to detect VHE flares from the Galactic Centre. In this work, long-term study of Sgr A* with H.E.S.S. I and data involving H.E.S.S. II around pericentre passage time of G2 is presented. Varibility tests are also applied to check for transient events. The overall spectrum and spectra for individual years have been stable over the years. The results of variability tests also revealed stability in the flux.

Contents

List of Figures

List of Tables

Chapter 1

Gamma Ray Astronomy

Gamma-ray astronomy is the study of astronomical objects using the most energetic photons with over 10,000 times more energy than visible light photons in the electromagnetic spectrum. Since these highly energetic photons can travel long distances in the universe without absorption by intergalactic dust, they can probe obscured regions of our Galaxy and distant regions of the universe. If you see the sky in gamma-rays, the night sky would look unfamiliar and strange. Stars and galaxies which are constantly shining would be replaced by something violent and ever-changing. Gamma rays can look through the hearts of solar flares, supernovae, neutron stars, and active galaxies. Scientists are now working hard to search for new physics, testing theories and performing experiments by exploring the universe at these high energies. Gamma-ray astronomy has been an important and exciting field in the last two decades, with many major discoveries made by both space-based and ground-based experiments. In this section, a summary of the production mechanisms of γ-rays, a brief review of the history of gamma-ray astronomy, space-based and ground-based detectors and an introduction of different γ-ray sources are given.

1.1 Production mechanisms of gamma-rays

The hottest objects observed in the universe, e.g. accretion discs, emit thermal radiation as energetic as hard X-rays in the range up to $\approx$ 10 keV. Hence, it is evident that any radiation exceeding these energies must be generated by non-thermal processes. These processes typically involve 1) interactions with matter, 2) interactions with photon fields, and 3) interactions with magnetic fields. A nice summary of the important processes and their implication is found in [38]. An overview of these processes is given below.

Interactions with matter

These include Bremsstrahlung and neutral pions decay by relativistic protons. Bremsstrahlung is due to the radiation emitted by accelerating charged particles deflected by a nucleus. A more detailed discussion is found in Section 3. When protons collide with protons in gas nuclei, neutral pions are produced and they subsequently decay into two γ-rays. A more detailed discussion of this process is found in 3.1.2.

Interactions with photon fields

The interaction of relativistic electrons with low-energy photons through Inverse Compton (IC) scattering is one of the most important mechanisms in producing γ-rays. Relativistic electrons up-scatter ambient low energy photons to γ-ray energies. Since astrophysical objects offer plenty of such photons, IC works efficiently everywhere, from compact objects like AGNs or pulsars to extended supernova remnants.

Interactions with magnetic fields

Due to Lorentz force, charged particles spiral around magnetic fields, producing synchrotron radiation. It is argued that synchrotron radiation from ultra-relativistic protons in a strong magnetic field is resposible for the TeV emission from blazars [40] [41].

1.2 A Brief History of Early Development of Gamma-ray Astronomy

The French physicist Paul Villard is considered to be the one who first discovered gamma rays. Back in 1900, he was performing experiments with radium salts. Though he shielded the radiation from the source with lead, he still found some remaining radiation consisting of a second and third type of rays. One showed deflection in a magnetic field which was Rutherford's beta rays. The other type was very penetrating. He did not suggest a specific name for this type of radiation. It was not until 1903 that Rutherford proposed to call this "gamma rays" to differentiate them from alpha and beta rays. Later in 1914, Rutherford and Andrade [1] showed that gamma rays reflected from rock salt crystals behaved like waves. This demonstrated the wave nature of gamma rays.

The idea of cosmic γ rays originated from Milikan. He is the one who first suggested there should exist cosmic γ-ray sources and that cosmic rays are actually gamma rays. But this idea was soon disproved. For example, Clay [2] in 1932 showed that cosmic rays did not have electromagnetic nature through the establishment of latitude effect and hence to the influence of the Earth's magnetic field on the incident particles. The idea of cosmic γ-ray sources was abandoned until the 50s. In 1935, Yukawa [3] predicted the existence of mesons which mediate the strong force in the atomic nucleus. In 1948, neutral pions were artificially produced at the University of California's cyclotron in Berkeley [4]. These led to the revival of the idea of cosmic γ-ray sources. Feenberg and Primakoff [5] discussed the collision processes between cosmic ray primaries (protons and electrons) and the thermal photons of sunlight and starlight. They found that the number of collisions between primary particles and thermal photons as they traverse the solar system and the local galaxy is not large enough to cause considerable energy loss to the particles.

Hayakawa [6] predicted that interactions of cosmic rays with interstellar matter would lead to diffuse γ-ray emission. Hutchinson [7] estimated γ-ray emission from cosmic Bremsstrahlung. The birth of gamma astronomy came with Morrison [8]. He performed calculations estimating γ-ray fluxes from a number of astronomical sources. He showed that a number of different processes occurring in the Universe would result in γ-ray emission. These processes included supernova explosions, interactions of energetic electrons with magnetic fields and cosmic ray interactions with interstellar gas. However, due to insensitivity of the early instruments and poor background rejection abilities, there was not much hope of discovering γ-rays at that time.

1.3 Space-based Gamma-ray Detectors

Since γ-rays coming from the universe are mostly absorbed by the Earth's atmosphere, γ-ray astronomy could not develop until balloons or spacecraft could be sent above the atmosphere. It was not until the 1960s that the ability to actually detect γ-ray emissions from the universe came to pass. γ-rays span a large energy range. The whole range is subdivided into different categories:

- High Energy (HE): 30 MeV- 10 GeV [9]
- Very High Energy (VHE): 10 GeV-100 TeV [10]
- Ultra High Energy (UHE): 100 TeV-100 PeV
- Extremely High Energy (EHE) 100 PeV-100EeV

Different detectors cover different ranges of γ-rays. A brief summary of space-based

γ-ray detectors is given in this section.

NASA's Explorer 11 was the first space-bourne γ-ray telescope launched in 1961. It aimed to map the direction of gamma-rays with emphasis on the Galactic Plane, the Galactic Centre, the sun, and other known radio noise sources. It is sensitive to energies above 50 MeV. The satellite detected some 100 cosmic γ-ray photons from our galaxy, but the results were inconclusive.

OSO1, the first in a series of 8 Orbiting Solar Observatories was launched in 1962. The primary goals of the mission were to measure the electromagnetic radiation from the sun in the UV, X-ray, and gamma-ray range. One instrument on board called the University of Minnesota Gamma-ray Experiment, was designed to provide preliminary measurements of the intensity and directional properties of low-energy gamma-rays (50 keV - 3 MeV) in space. However, no such radiation was detected.

In 1967, gamma-ray bursts were accidentally discovered by the Vela program, which was a set of satellites equipped with 18 internal neutron and gamma-ray detectors and 12 external X-ray detectors. The X-ray detectors could directly sense the flash of X-rays from a nuclear blast while the gamma-ray detectors could provide a confirming signature of a nuclear event. The devices were designed for military purposes rather than scientific ones. However, γ-ray bursts signals were first detected by one of the satellites.

Significant γ-ray emission was first detected from our Galaxy with the OSO-3 satellite in 1967 [11]. 621 events were detected. In the 70s, a great leap forward was made by the Small Astronomy Satellite 2 (SAS-2) and the COS-B satellites. The SAS2 was the second in the series of small spacecraft launched in 1972. SAS is a NASA project designed to study the IR, visible, ultraviolet, X-ray, and γ-ray regions of the electromagnetic spectrum. The primary goal of the SAS2 was to measure the spatial and energy distribution of primary galactic and extragalactic γ radiation in the range of 20 to 300 MeV. SAS-2 revealed that the γ-ray radiation from the Galactic Plane has a strong correlation with galactic structural features [12]. The SAS-2 results not only clearly established a high energy component to the diffuse celestial radiation but also saw high-energy γ-ray emission from discrete sources such as the Crab and Vela pulsars. It is generally acknowledged that SAS-2 provided the first detailed information of the gamma-ray sky and indicated a promising future of gamma-ray astronomy.

COS-B is an ESA mission from 1975-1982 carrying a single large experiment, the Gamma-Ray Telescope. Its mission is to study in detail the sources of extra-terrestrial γ-ray radiation at energies above 30 MeV. Its results created a catalogue known as the 2CG catalogue, which listed around 25 γ-ray sources and a complete γ-ray map of the disc of our Galaxy.

The Compton Gamma Ray Observatory (CGRO) was the second in NASA's program of orbiting "Great Observatories" in operation from 1991 to 2000, following the Hubble Space Telescope. It could detect γ-rays from 20 keV to 30 GeV. There were four main instruments on board:

1) Burst And Transient Source Experiment (BATSE) for the study of the phenomenon of γ-ray bursts

2) Oriented Scintillation Spectrometer Experiment (OSSE), which consists of four NaI scintillation detectors. Each of the detectors can be individually pointed which allows observations of a γ-ray source to be alternated with observations of nearby background regions.

3) Imaging Compton Telescope (COMPTEL), which reconstructs an image of a γ-ray source in the energy range 1 to 30 MeV by utilizing the Compton Effect and two layers of γ-ray detectors.

4) Energetic Gamma Ray Experiment Telescope (EGRET), which works in the range of 20 MeV to 30 GeV. It is 10 to 20 times larger and more sensitive than previous detectors operating at these high energies. The main scientific goals are to perform an all-sky survey of high-energy γ-ray emission and make detailed studies of high-energy γ-ray emitting sources. Its major discoveries include the identification of a type of AGNs called blazars. The observations of the LMC and SMC were used to confirm the Galactic origin of cosmic rays. Since EGRET could reject background efficiently, it has obtained the first sensitive map of the diffuse γ-ray emission of the Milky Way.

Several instruments came online in 2000s. These included International Gamma-Ray Astrophysics Laboratory (INTEGRAL), Swift and Fermi. With these instruments, γ-ray astronomy has entered its golden age.

INTEGRAL is the successor of the ESA γ-ray observatory Cos-B and the NASA γ-ray Observatory CGRO. With its high spectral (E/E = 500) and spatial resolution (angular resolution: 12 arcmin FWHM), it is dedicated to fine spectroscopy and fine imaging of celestial gamma-ray sources in the energy range 15 keV to 10 MeV. Equipped with X-ray (3-35 keV) and optical detectors (V-band, 550 nm), it could also provide simultaneous observations in these wavebands. There are four instruments on board:

1) Spectrometer on INTEGRAL (SPI)

It performs spectral analysis of γ-ray point sources and extended regions in the energy range 20 keV - 8 MeV with an energy resolution of 2 keV (FWHM) at 1 MeV.

2) Imager on Board the Integral Satellite (IBIS)

It provides diagnostic capabilities of source identification, fine imaging and spectral sensitivity to both continuum and broad lines over a broad (15 keV - 10 MeV) energy range.

3) The Joint European X-Ray Monitor (JEM-X)

It is a supplement to IBIS and SPI, and plays a crucial role in detecting and identifying the γ-ray sources and in the analysis and scientific interpretation of Integral γ-ray data.

4) The Optical Monitoring Camera (OMC)

It consists of a passively cooled CCD working in frame transfer mode. The CCD is located in the focal plane of a 50 mm (diameter) lens including a Johnson V-filter to cover the 500 - 850 nm wavelength range.

As of the time of writing, INTEGRAL is still in operation. Up to now, INTEGRAL has aided our understanding of some of the most fundamental processes at work in the Universe. Some of the major contributions include mapping of the Galactic plane in γ rays, resolving diffuse γ-ray emission from the Galactic Centre and detection of γ-ray bursts, including one of the closest and faintest on record (GRB 031203).

Swift is a NASA mission, a multi-wavelength space observatory dedicated to the study of γ-ray bursts. It has three intruments which work together to observe GRBs and their afterglows in the γ-ray, X-ray, ultraviolet, and optical wavebands. The three instruments are 1) Burst Alert Telescope (BAT) , which detects GRB events and computes its coordinates with fast speed in the sky, 2) X-ray Telescope (XRT), which takes images, perform spectral analysis of the GRB afterglow and perform long-term monitoring of GRB afterglow light-curves, and 3) Ultraviolet/Optical Telescope (UVOT), which is used to detect an optical afterglow.

Within seconds of detecting a burst, Swift relays its location to ground stations so that both ground-based and space-based telescopes around the world can observe the burst's afterglow. Typically, three or four bursts were detected every week. This greatly increased the number of GRBs with observations in optical afterglows and spectra obtained, improving our understanding of these enigmatic and powerful events.

Fermi is the latest space-based telescope launched in 2008. The mission is a joint venture of NASA, the United States Department of Energy, and government agencies in France, Germany, Italy, Japan, and Sweden. On board there are two scientific instruments, the Large Area Telescope (LAT) and the Gamma-ray Burst Monitor (GBM).

The GBM consists of 14 scintillation detectors with sensitivity from 150 keV to 30 MeV. It can detect gamma-ray bursts not blocked by the Earth across the whole sky.

The LAT is an imaging γ-ray detector with a FOV of about 20% of the sky. It is designed to detect photons from 10 MeV to 300 GeV. It scans the entire sky every 3 hours. Up to now, it has discovered thousands of high-energy γ-ray sources. These include pulsars, pulsar wind nebulae, supernova remnants, several classes of active galaxies, binary sources and γ-ray bursts. The data obtained over the past years not only discovered new sources and source classes, but also revealed new things about known sources such as the Crab nebula. Fig. 1.1 shows the Fermi sky based on 5 years of data.

In 2015, Fermi presented the third Fermi Large Area Telescope (LAT) source catalog (3FGL) which is based on the first 4 yr of science phase of the mission. This catalog includes 3033 sources above 4σ significance, detected and characterized in the 100 MeV to 300 GeV range. 1010 of the sources are unidentified, meaning that no plausible counterparts are found at other wavelengths. More than 1100 of the identified ones are blazars. Pulsars are the most populated source type among the Galactic sources.

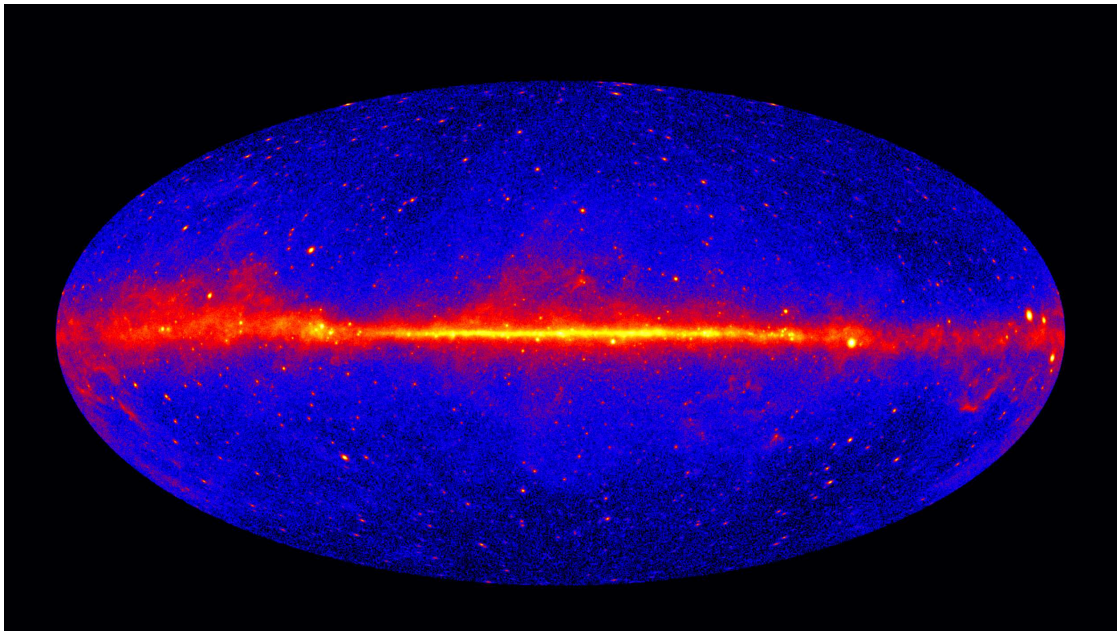

Figure 1.1: The entire sky at energies larger than 1 GeV based on 5 years of data from Fermi LAT. Image Credit: NASA/DOE/Fermi LAT Collaboration

1.4 Ground-based Gamma-ray Detectors

Ground-based gamma-ray detector has been in rapid development over the past two decades. They made some important discoveries which significantly deepen our understanding of the universe. This section gives a brief introduction of the major IACTs, namely Whipple, HEGRA, VERITAS and MAGIC. For an introduction of HESS, see Section 4. For some earlier history of IACTs, see Section 3.1.3.

Whipple

It is the first purpose-built instrument for γ ray astronomy constructed in 1968 on the slopes of Mount Hopkins in Arizona. It consisted of a single 10 m γ-ray telescope. With then a high resolution camera (1/4 °, the TeV emission from the Crab Nebula was first detected at a significance level of 20 σ in 30 hours [13]. This is the pioneering work of IACT. In 1994, Whipple[14] detected flaring activity from Mrk 421. It was the first clear detection of flaring activity in the VHE emission from an AGN.

HEGRA

It was located in the Canary island of La Palma and was the first IACT system adopting a stereoscopic approach. It came into full operation in 1996. The full system consisted of 5 identical telescopes, each of which has a 8.5 square meters mirror reflector area and a camera of 271 pixels. The stereoscopic technique improved flux sensitivity by an order of magnitude higher and the energy threshold was reduced down to 100 GeV.

A remarkable achievement made by HEGRA was the detection of the most energetic photons observed from an extragalactic object Mrk 501 at 16 TeV.

VERITAS

It consists of four 12 m diameter telescopes located in Arizona, USA, at the same site as Whipple. It saw its first light in summer 2007. In 2012, all of the telescope detectors were replaced with more sensitive, "super-bialkali" devices. These instrument increased the Cherenkov light yield by 50%, reduced the energy threshold by 30% and improved sensitivity for soft spectrum sources.

MAGIC

It started observation in La Palma in 2004. At first, there was a single 17 m diameter telescope. A second telescope, MAGIC-II, began taking data in 2009. These two telescopes together form a stereoscopic system.

In 2007, a new analog Sum-Trigger was installed in the MAGIC I telescope. The trigger threshold was then lowered from 55 GeV to 25 GeV. Subsequent upgrades included a continuously variable analog delay line and a much larger trigger area consisting of a fully revised configuration of overlapping summing patches. These brought significant improvement in the sensitivity of the very low energy regime of 20 to 100 GeV, which is crucial for detailed pulsar studies, as well as the observation of high-redshift AGNs and distant GRB events [15].

1.5 Gamma-ray Sources

With the rapid development in both space-based and ground-based γ-ray detectors, many γ-ray sources of different types have been discovered in the past two decades. Figure 1.2 shows the current VHE sky from the TeV catalogue. Each source type has a different colour and symbol which is illustrated in the legend. As can be seen in the figure, the Galactic Centre is a crowded region with different types of sources found. In the Galactic Plane, PWNe are the most populated. In the extragalactic region, blazars are the most common type. In this section, different known VHE source types and some open questions are discussed.

1.5.1 Pulsar Wind Nebulae (PWNe)

PWNe are the largest single class of identified Galactic VHE γ-ray sources. In the centre of a PWN, there lies a rapidly spinning neutron star which produces a relativistic wind of electrons and positrons that transports its spin-down energy to the surrounding nebula. PWNs are seen from radio to gamma-rays. The Crab Nebula is the prototype of this

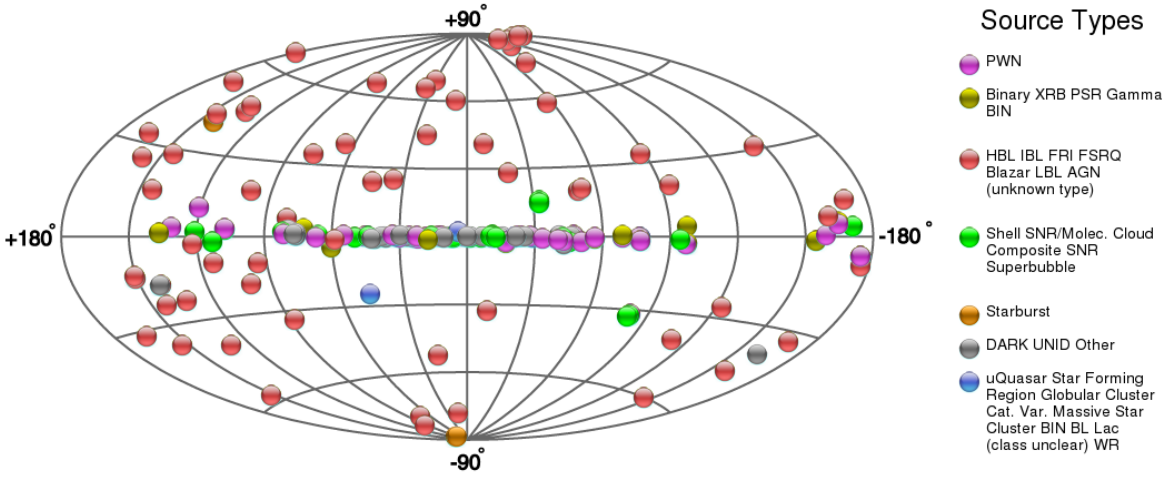

Figure 1.2: The VHE sources in the sky as of 2015-09-07 (Image taken from http://tevcat.uchicago.edu/). The different colours and symbols used for each type of the source are listed in the legend.

class. It is considered the "standard candle" for high energy astrophysics because of its constant and strong VHE flux.

They are interesting because of several reasons. They are close and bright, rendering themselves the best-suited laboratories for the physics of relativistic astrophysical plasmas. They are the only sources showing direct evidence for PeV particles. Moreover, PWNe have the highest speed shocks in nature. This can effectively accelerate particles (For a review of PWNe, see [16] and references therein). These show they are the most efficient accelerators observed in the nature. However, the exact acceleration mechanisms and the sites of acceleration are unknown. There are several mechanisms proposed involving Fermi mechanism (e.g. [17] [18]), resonant cyclotron absorption in ion doped outflow (e.g. [19] [20]) and driven magnetic reconnection (e.g. [21], [18]). Another interesting question is about the interaction between the host SNR and its PWN, and how much of the γ-ray emission is produced by the SNR.

1.5.2 Supernova Remnants (SNRs)

These objects are the relics of the explosion of massive stars. They are thought to be the sources of cosmic rays up to the knee, a point of an energy of a few PeV, and of TeV photons. Based on whether they have a filled centre, SNRs are classified into three categories, namely shell-type, plerion-type and composite. Shell-type SNRs have limb brightened morphology in both X-ray and radio bands. X-ray emission can be thermal or non-thermal. Some examples are Cassiopeia A, Tycho, and Kepler. Plerion-type shows non-thermal emission with centre-filled morphology. Examples include the Crab Nebula, G21.5-0.9 and 3C 58. In a composite SNR, both shell-like and centre-filled morphology can be seen. Vela SNR, G11.2-0.3 and CTB 109 are some examples. VHE emission from all types have been detected. Among them, plerion-type SNRs are the most populated. For a review of SNRs, see [22] and [23].

There are two models of leptonic and hadronic origin which can explain the γ-ray emission of SNRs. In the leptonic scenario, relativistic electrons produce the synchrotron X-ray emission and scatter ambient photons to produce TeV emission by inverse Compton scattering. In the hadronic scenario, γ-rays can be produced by neutral pion decay due

to proton-proton interaction between cosmic rays produced by SNRs and the ambient interstellar medium (e.g. [24] [25] [26]).

For cosmic ray acceleration to happen, the acceleration in diffusive shocks has to move fast enough so that particles can reach PeV energies before the SNR has swept up much of the interstellar medium. In order for the acceleration to proceed fast enough, strong magnetic fields which are 100 -1000 times higher than the interstellar medium value are required [27]. Such high values of the magnetic fields argues against a leptonic origin for the observed γ-ray emission. The expected synchrotron radiation from relativistic electrons would exceed the measured X-ray emission. Such an amplification of the magnetic field might be induced by the CRs themselves. High resolution X-ray observations of SNR shocks have found some evidence in this scenario [28]. However, their interpretation is under debate. Thus, an accurate determination of the intensity of the magnetic field at the shock is of crucial importance in order to distinguish between the leptonic and hadronic scenario for γ-ray emission. Other than the debate on the nature of the VHE emission, there are some other important questions related to the acceleration mechanisms. For example, the maximum energy that particles can reach throughout the SNR evolution is still not known .

1.5.3 Active Galactic Nuclei (AGNs)

Active Galactic Nuclei (AGNs) are galaxies with a compact nucleus, a black hole, which have high luminosities across the whole electromagnetic spectrum. They are thought to be powered by accreting matter onto the central black hole. Because of conservation of momentum, the accreting materials circulate around the black hole without falling in directly. A disk around the core is formed and produces continuum emission from UV to soft X-rays. AGNs are observed with two opposite jets consisting of relativistic particles that are aligned perpendicular to the accretion disk. These jets are believed to be particle acceleration sites. AGNs were one of the first sources detected at TeV energies and have remained the largest source population for TeV gamma-ray astronomy. For a review, see [29].

Most of the TeV AGNs are blazars, which are highly variable across the entire electromagnetic spectrum, producing flares of different durations from a few minutes to many months. There are several models proposed to explain the broadband SED. For the low energy part of the SED, both the leptonic and hadronic models attribute it to synchrotron radiation from relativistic electrons in the jets. The seed photons in the leptonic model may be of an internal or external origin. In the internal scenario, the seed photons producing the low energy peak by synchrotron radiation are upscattered by the same population of electrons, producing the high energy peak. This model is called self-synchrotron Compton (SSC) model (e.g., [30] [31]). In the other scenario, the photons producing the high energy peak is external to the jet (e.g., [32] [33]). These simple homogeneous models were motivated by the apparent correlation between X-ray and TeV flares. However, observations have shown that the correlation between flares of both energy bands are quite loose and either one can appear alone. Thus, inhomogeneous models have been proposed [34]. Further observations are required to tell whether they can account for all of the observed properties of TeV blazars.

One of the hadronic models proposed is due to neutral pion decay produced by proton-induced cascade [35] or pp collisions [36] [37] [39]. Another model proposed to explain the TeV emission invokes the synchrotron radiation from ultra-relativistic protons in a strong magnetic field [40] [41]. One main challenge faced by the hadronic models is that they cannot explain the stand-alone TeV γ-ray flares.

The jets which come with black holes are another puzzle. Some astronomers think they are made of plasma, while some think they are made of electrons, positrons, and/or protons. The proportions that each of these particles account for in the jets are not certain. Furthermore, how the jets are launched is also unknown. Perhaps it is due to the Blandford-Znajek process, which is related to the magnetic field of the accretion disk, or by the Penrose process, which relies on a spinning black hole.

1.5.4 X-ray Binaries

X-ray binaries have played an important role in the development of TeV γ-ray astronomy historically. Though γ-ray emission were claimed to have been detected in the 70s and 80s, none of the early claims is now considered credible since the sources were not seen with the newer and much more sensitive experiments over the past two decades. For a review, see [42] and [43].

The study of binary systems containing compact objects at VHE is important. These systems are highly complicated and they enable us to probe several important physical processes. For example, these systems are extremely efficient accelerators. Within present theoretical framework, such a high efficiency is not easy to explain. This calls for a revision of particle acceleration theory.

The first definitive detection of an X-ray binary (PSR B1259-63) was made by HESS [50]. This binary system consists of a neutron star and a Be star. Be stars rotate fast enough to produce a dense equatorial wind. Accretion is enhanced onto the neutron star when it passes through the wind and capture it. This leads to X-ray and γ-ray activities. On the other hand, a strong shock results if stellar wind collides with pulsar wind. The observed TeV γ-rays for this system may be leptonic or hadronic. They may be due to relativistic electrons accelerated by the strong shock via inverse-Compton scattering. The hadronic model involves neutral pion production by the pp process [44].

The orbital modulation of the GeV flux of both LS I +61 303 [45] [46] and LS 5039 [47] [48] showed anti-correlation with the modulation observed at TeV energies. Both sources showed an exponential cut-off power-law shape in their spectrum. It has been proposed that the γ-ray emission may be magnetospheric in nature. However, how such emission would be modulated by the orbital period of the binary is not clear.

1.5.5 Gamma-ray Bursts

Gamma-ray bursts (GRBs) are extremely energetic explosions that occur at cosmological distances in the universe. The intensity of the bursts is greater than all other γ-ray sources. Though discovered several decades ago, they are still one of the biggest mysteries in astronomy. They last for a very short time, from a few milliseconds to several minutes. Since they are uniformly distributed in the universe, it is suggested that they have an extragalactic origin. For a review of gamma-ray bursts, see Piran (2005).

Observationally they are divided into two classes according to the duration. Short γ-ray bursts last for at most 2 seconds while long γ-ray bursts last for longer. The difference in the duration is presumably the result of different progenitor systems. Generally long GRBs are considered to be due to the collapse of massive, rapidly rotating stars into black holes. As for short GRBs, the origin is less certain. One favourable candidate is neutron star merger events. Observing the VHE emission from GRBs can help solve the enigma of the nature of it. For example, what types of stars die as GRBs? Do they signal the birth of a black hole in a massive stellar explosion? How is the burst duration determined? Do GRBs have a unified source or there are more than one type

of phenomena that cause GRBs?

1.5.6 Unidentified Sources

One of the most intriguing recent developments in the field of TeV astronomy is the discovery of γ-ray sources with seemingly no counterparts at other wavelengths. For a moderately strong point sources, IACTs are able to locate them with precision. Extragalactic TeV sources can usually be identified with a counterpart at other wavelengths. The presently unidentified TeV γ-ray sources are around the Galactic plane. The diffuse emission lies mainly in the GeV regime, which does not contribute to the unidentified sources. Most of the TeV γ-ray sources are spatially extended, indicating an association with unseen PWNe or SNRs. One explanation for such unidentified VHE gamma-ray emitters is that there is simply not sufficient multi-wavelength data available to make a positive identification in longer wavelengths. Indeed, some of the previously unidentified γ-ray sources were subsequently found to be associated with SNRs or PWNs [50] [51] [52] [53].

A second explanation for the unidentified sources is that there exists another type of VHE emitter which emits more strongly in the VHE band than any other bands. Such a scenario is possible in some high-energy proton models, and may even be predicted for exotic phenomenon like γ-ray bursts [54]. In this case considerable constraints on theoretical models of VHE γ-ray production can be placed by making VHE observations.

Other than the above-mentioned VHE γ-ray source types, the Galactic Centre is a unique source of γ-rays. The next section will give an overview of the VHE emission from Sgr A*.

Chapter 2

The Galactic Centre

2.1 The Supermassive Black Hole

Back in the 1930s, Jansky found 3.6 cm radio emission from the inner few parsecs of our Galaxy. In 1971, Lynden-Bell and Rees [55] applied the then very speculative black hole model for quasars to the Galactic Centre and proposed that it should also contain a supermassive black hole which might be detectable with radio interferometry. In 1974 , strong radio emission from the inner 1pc core of galactic nucleus was detected with the National Radio Astronomy Observatory (NRAO) interferometer [56]. The brightness temperture was found to be $\sim 10^7$ K and the structure was unresolved at the level of ~ 0.1"(arcsec). Eight years later, Brown [57] named it Sgr A* to make it unique and to distinguish it from Sgr A complex, which is more extended. Subsequent VLA observations [58] with higher precision showed that it was located near the dynamical centre of the gas streamers in the Galactic nucleus (Fig. 2.1). All these observations demonstrate that Sgr A* is extraordinary.

Since discovery, astrophysicists have been working hard for the observation of Sgr A* at radio, optical, and near-infrared wavelengths. The high velocity (up to 1400 km/second) of gas and stars swirling around Sgr A* make them suspect that there is really a supermassive black hole in it. However, a cluster with millions of closely packed stars could also lead to the fast moving gas and stars. X-ray observations can provide a definitive answer here. Just before matter is finally accreted onto the black hole, it is heated up to high temperatures which allows it to emit X-ray radiation. Moreoever, only X rays have the power to penetrate the thick gas and dust around the Sgr A*. Using the Einstein X-ray Observatory, well-defined source of X rays close to Sgr A* were found [60]. However, due to limited resolution, it could not be concluded that the emission originated from the compact central source Sgr A*. The highlight came in early 2000 when Chandra pinpointed a source of X rays coming from a location which coincided with Sgr A* within 0.35 arcsec [61] (Fig. 2.2). However, this revealed another problem. The X-ray luminosity was only a fifth of what was predicted in theory.

From high-resolution near-infrared data taken with the 10-m Keck telescope on Mauna Kea and 8-m VLT telescopes in Chile, two groups tracked the change in positions of about two dozen stars that are within a few light-weeks of Sgr A* [62] [63]. Using data of more than a decade, they were able to plot detailed orbits for each of the stars in their studies (Fig. 2.3). From the motions of the stars, both groups found that they were orbiting around a mass of about 4 million $M_\odot$. This is the first time the mass of the supermassive blackhole was derived.

Sgr A* is the supermassive black hole closest to us, making the angular size of the Schwarzchild radius larger than any other black holes. At 8 kpc, R_{sch} is about 0.1 AU [65]). By extrapolation, VLBI observations at 7 mm and 3.5 mm indicated that the size of Sgr A* at 1.3mm is of 20-40 microarcseconds [66]. At 1.4 mm, the size is found to be 50-170 μas. However, due to interstellar scattering, wavelengths longer

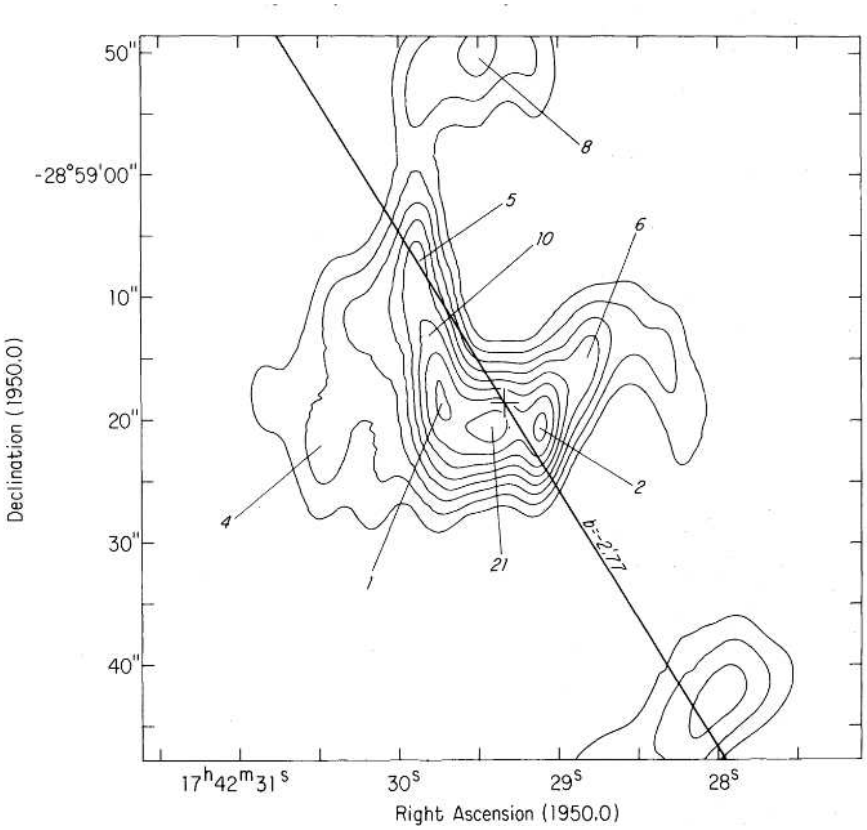

Figure 2.1: The 5 GHz VLA image taken from Brown et al. [58]. The numbers represent the 10μm peaks identified by Becklin & Neugebauer [64].

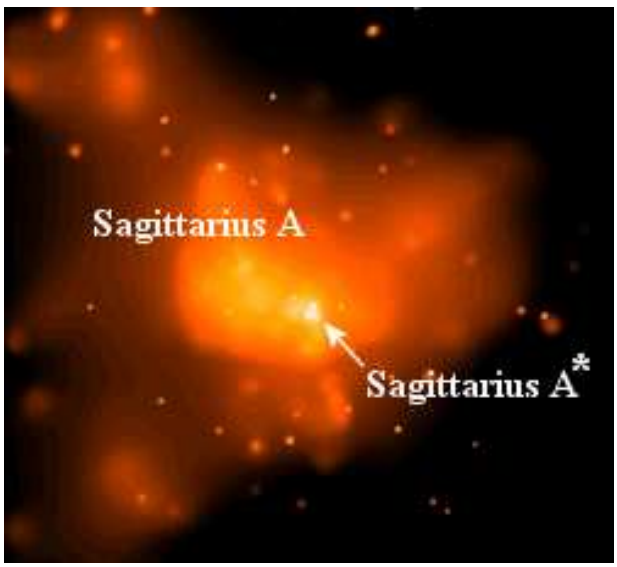

Figure 2.2: X-ray image of Sgr A* taken by Chandra. Image credit: NASA Chandra X-Ray Observatory and Penn State University [59]

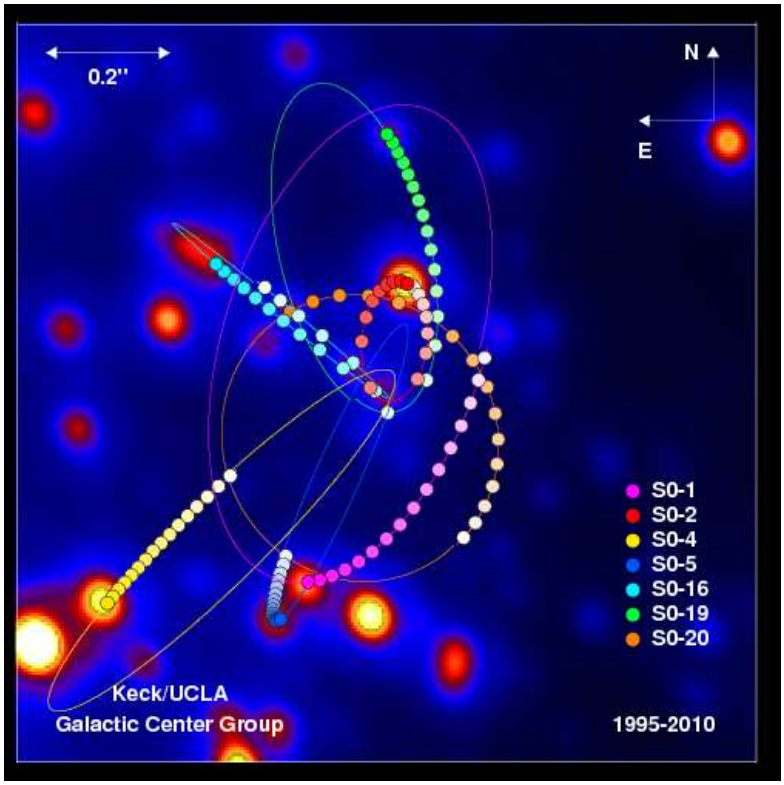

Figure 2.3: Stars circling around the Galatic Centre within 0.02 parsecs. Yearly positions of seven stars are color coded. Image credit: Keck/UCLA Galactic Centre Group

than 1.3 mm are broadened. Later observations were made again using VLBI when the wavelength was extended to 1.3 mm, the intrinsic diameter of Sgr A* was set to 37 microarcseconds [67]. Shen et al. [68] made observations with the Very Long Baseline Array (VLBA) at the shortest wavelength of 3.5 mm. The radio image demonstrated a size of $\sim$1 AU (Fig. 2.4). The authors derived the mass density to be 6.5×10^{21} $M_\odot$ pc^{-3} assuming a lower mass limit [69]. From these observations, the small size and high density indicate Sgr A* is a compact radio source holding a supermassive black hole.

From the observations of stellar winds surrounding Sgr A*, the mass accretion rate is found to be $\dot{M}_{accretion} \sim 10^{-5}$ $M_\odot$ yr^{-1} (e.g. [70] and references therein). Numerical simulations indicate a large angular momentum, rendering a smaller accretion rate $\dot{M}_{accretion} \sim 10^{-6}$ $M_\odot$ yr^{-1} [71]. Based on this accretion rate, the bolometric luminosity is expected to be $\sim 10^{40}$ erg s^{-1}. However, observations [72] show the bolometric luminosity is $\sim 10^{37}$ erg s$^-$1, which is only $\sim 10^{-9}$ of the Eddington luminosity. Compared with other accreting black holes, Sgr A* is very faint. Narayan & Yi [73] proposed a model called "Advection-dominated Accretion Flow", in which most of the viscously dissipated energy is stored in the thermal energy and advected into the hole rather than radiated away. This model is radiatively inefficient due to inefficient electron heating. It can explain the low luminosity of Sgr A* and can roughly fit the spectrum. However, this model predicts a radio flux too low. It also predicts a high rotation measure which leads to a linear polarization far below observation. Yuan et al. [74] revised the model and included outflow which contributed to accretion efficiency. In this revised model, most of the accreted gas is lost into the outflow, lowering the rotation measure. Thus, the linear polarization is higher. To solve the problem of low radio luminosity, a jet ([75] [76]) is introduced in the model, or, the radio emission is due to synchrotron radiation

by a fraction of electrons in the ADAF which are in nonthermal distribution [74].

Though Sgr A* is rather dim, it is active in multi-wavebands. Below is a summary of observations in differerent wavebands.

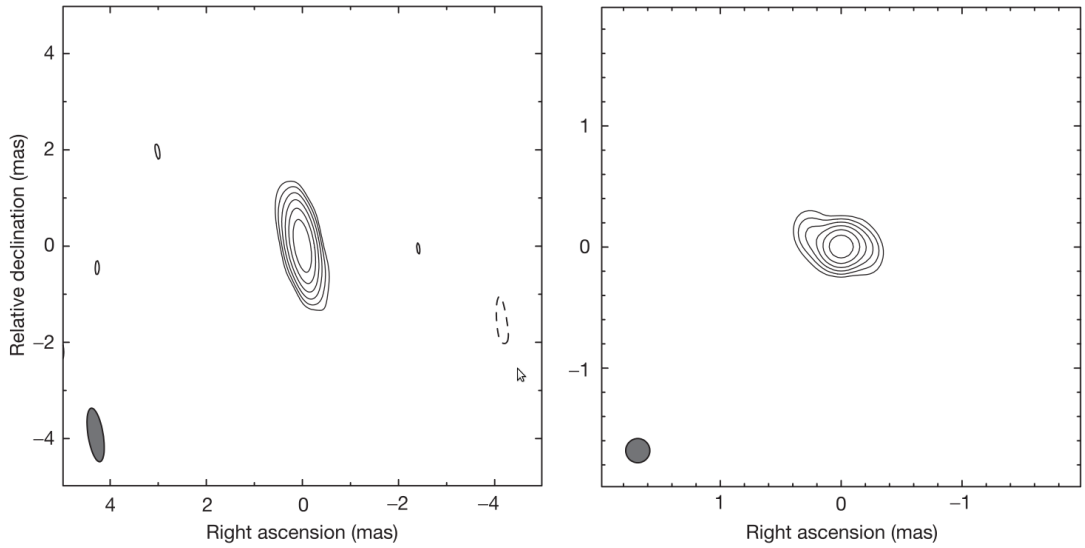

Figure 2.4: High-resolution VLBI image of Sgr A* obtained with the VLBA at 3.5 mm. Left: A uniformly weighted image with the restoring beam (indicated at the lower left corner) of 1.13 mas × 0.32 mas at 9°. Right: A super-resolution image with a circular beam of 0.20 mas. Image taken from Shen et al. [68].

2.2 Multiwavelength Observations

Miyazaki et al. [77] performed observations using the Nobeyama Millimeter Array in 100 and 140 GHz bands, and detected several flares, the shortest one being intraday.

Fast infrared flares showing a ∼ 17-minute quasi-periodic variability were observed using the VLT in 2003 [78]. The most powerful flare incresed by a factor of 5 in the H band (1.65μm). The emission can be modelled with highly energetic electrons or hot gas in the innermost accretion region.

A multiwavelength campaign at submillimeter, infra-red and X-ray was launched in 2004 [79]. Simultaneous X-ray and NIR flares were detected, with a time lag of less than 10 minutes by the X ray. Combined with previous flare data, this result indicates agreement with a synchronous evolution.

XMM-Newton caught a bright flare followed by three smaller flares in half a day in spring 2007. The big flare, having a peak amplitude of ∼100 times above the quiescent state, was then the second brightest recorded flare [80].

To study the correlation of variability between different wavebands, a multiwavelength campaign was conducted in radio, millimeter, near-IR and X-rays in 2004 using altogether nine ground- and space-based telescopes [81]. Simultaneous X-ray and near-IR flares with correlated substructures were observed for the first time (Fig. 2.5). Submillimeter and near-IR flaring activities were also observed simultaneously. The authors explain the variability in submillimeter during a near-IR flare with a low-energy component of the particles emitting synchrotron radiation in the near-IR. The submillimeter seed photons are upscattered by the near-IR-synchrotron emitting particles to X-ray.

Yusef-Zadeh et al. [82] carried out another simultaneous observation campaign in radio, submillimeter and X rays in 2006. The lightcurves are shown in Fig. 2.6. They found a delay of ∼110 mins between X-ray and 850 μm. Shorter time lags of ∼ 25 mins were observed between 22 and 43 GHz. The delay between different wavelengths can be explained with a simple model of a bubble of synchrotron-emitting electrons cooling via adiabatic expansion.

In 2009, Eckart et al. [83] observed the source for a single night at millimeter, near-infrared, and X rays . Sub-mm lightcurves were found to lag behind the NIR ones by about ∼45 minutes. The flares in different wavebands can be modeled as the signal from an adiabatically expanding synchrotron self-Compton (SSC) component.

Swift had been observing Sgr A* from 2006 to 2011 and detected six flares of an average luminosity $L_X \sim 10^{35}$ erg^{-1} (2-10 keV). The flaring rate is 0.1-0.2 day^{-1}([84]).

Using 15 years of XMM-Newton and Chandra data from 1999 to 2014, Ponti et al. [85] observed an increase in flux in 2013-2014 by a factor of 2-3. An increase of almost 10 times of the flaring rate since late summer 2014 was noted. This period was about six months after G2 had passed the pericentre (see the next section for G2). However, the source was monitored more frequently in that period than before. Thus, whether the increase in rate was due to a stationary noise process producing flares not uniformly distributed in time or increased accretion rate induced by G2 is not certain. The long-term X-ray lightcurves of Sgr A* is shown in Fig. 2.7.

Employing data during the first 25 mohtns of observations by the Fermi-Lat, studies on the morphological, spectral and temporal characteristics have been carried out [86]. No variability was found at GeV energies on the month timescale. The spectrum is best fit with a broken power law with break energy $E_{br} \sim 2.0$ GeV. The slopes before and after break energy are $\Gamma_1 \sim 2.2$ and $\Gamma_2 \sim 2.68$ respectively. Using the combined Fermi and HESS data, the authors showed that the spectrum of the central gamma-ray source is inflected with a relatively steep spectral region matching between the flatter spectrum found at both low and high energies.

VHE γ-ray emission was first detected by H.E.S.S. [87] as a point-like source. The spectrum is a power law with an index of 2.2. Subsequent observations made from 2004-2006 showed a similar index of 2.1 [88]. However, with three times more data the spectrum exhibited a cutoff at 15.7 TeV. Rayleigh tests and Fourier analysis were performed to study the periodicity of the source. From the results of the tests, neither periodicity nor variation in flux was detected.

The only simultaneous X-ray and γ-ray observations were conducted in 2005 [89], in which an increase of a factor of ∼9 was detected for X-ray but no evidence was found for increase in the TeV flux (Fig. 2.8). This implies keV and TeV emission are not associated with the same population of accelecated particles.

2.3 The Gas Cloud G2

The low bolometric luminosity of Sgr A* suggests a low accretion rate. The supermassive black hole has been "starving". However, in 2011, a dense gas cloud called "G2" was discovered by Gillessen et al. [90] with ESO VLT. From the L' band (3.8μm) spectroscopic data, it was found to have a mass three times that of the Earth and a low temperature of 550K. The orbit is highly eccentric (e = 0.966) (Fig. 2.9). Due to the elongated Br-γ emission along the direction of motion, and a spatially resolved velocity gradient, they suggested that G2 is a dusty, ionized gas cloud.

The first observations suggested that it would pass the pericentre in mid 2013, at a

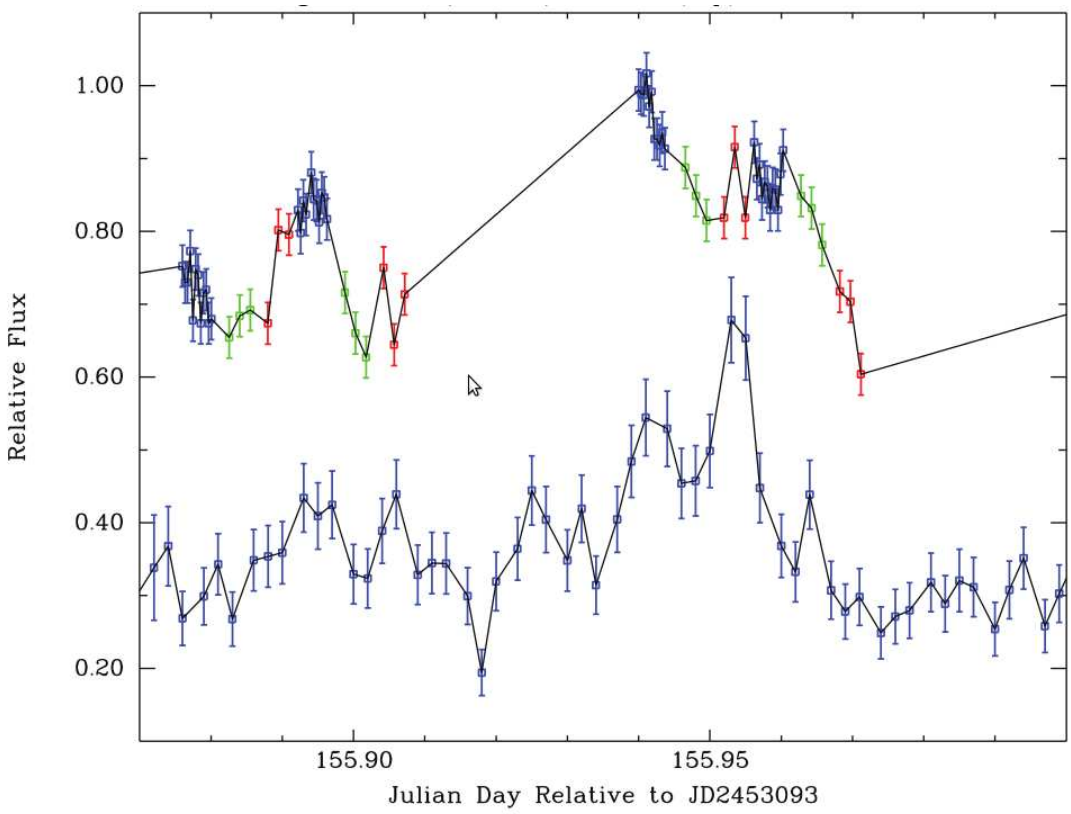

Figure 2.5: Simultaneous near-IR (top line) and X-ray (bottom line) lightcurves of Sgr A* in a flaring state. The vertical axis shows the observed flux density in near-IR wavelengths and the observed count rate in X-ray wavelengths. The green, red and blue data in the near lightcurves represent different filters. Image taken from [81].

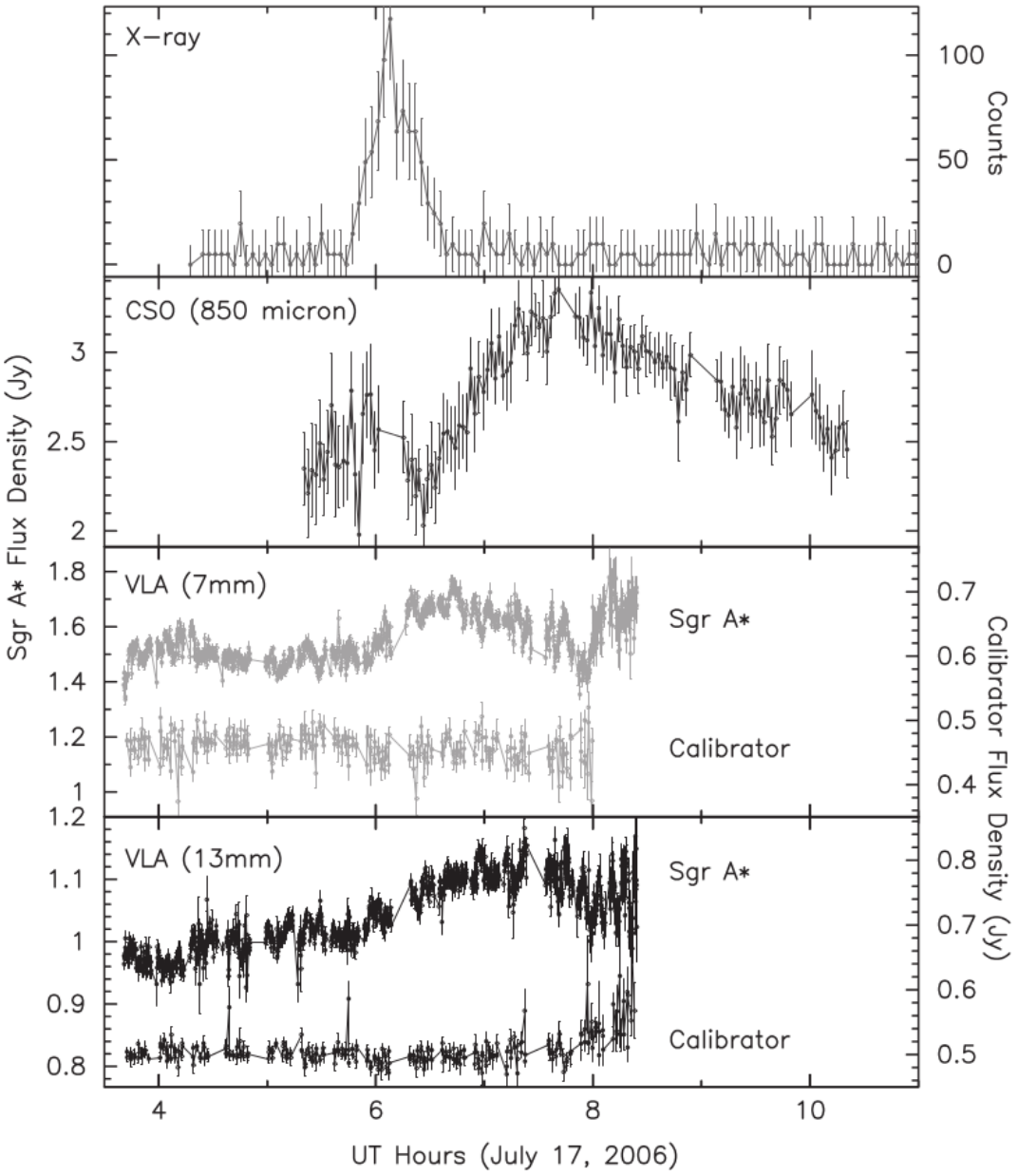

Figure 2.6: Lightcurves of Sgr A* using Chandra, CSO, and VLA observatories. The fluxes in X-ray are shown in count rate while the rest are measured in Jy. Image taken from [82].

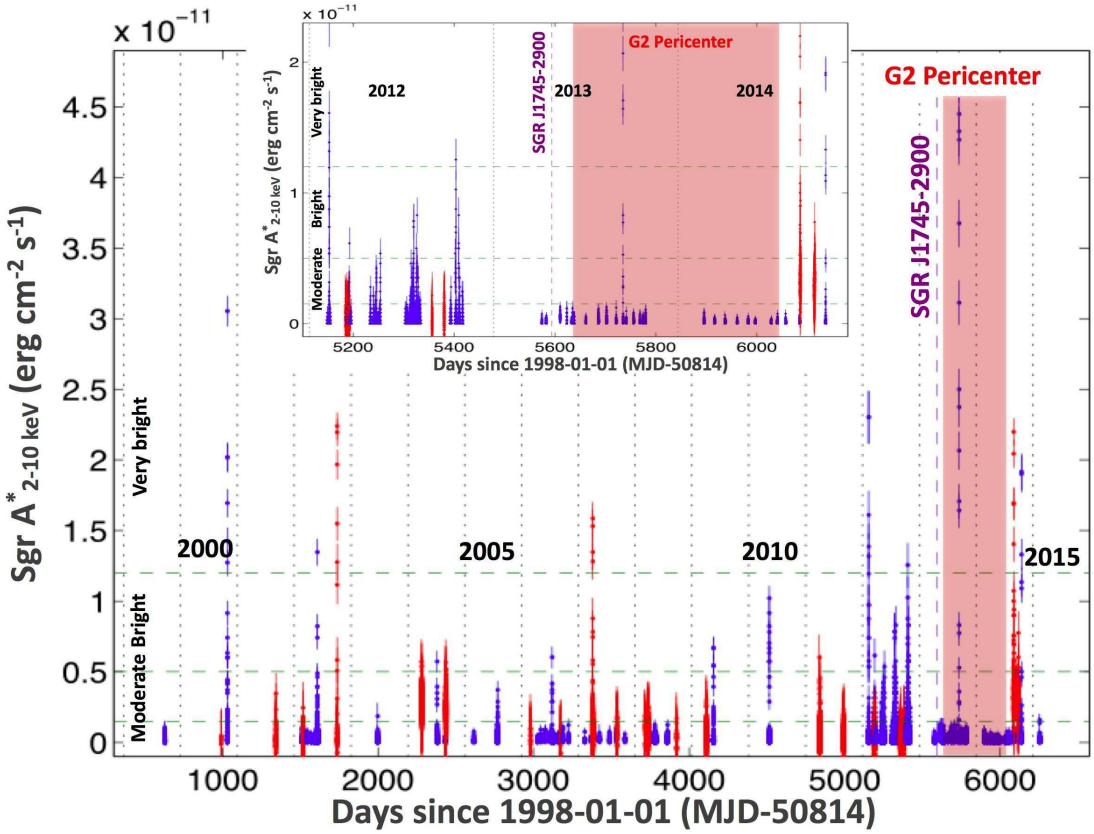

Figure 2.7: (Main figure) Light curves of XMM-Newton (red) and Chandra (blue) of the 2-10 keV flux emitted by Sgr A*. Gaps between observations are removed. (Upper panel) Zoom on the 2013-2014 period that shows no moderate flare but 5 bright flares at the end of the XMM-Newton and Chandra monitoring campaigns. Image taken from [85].

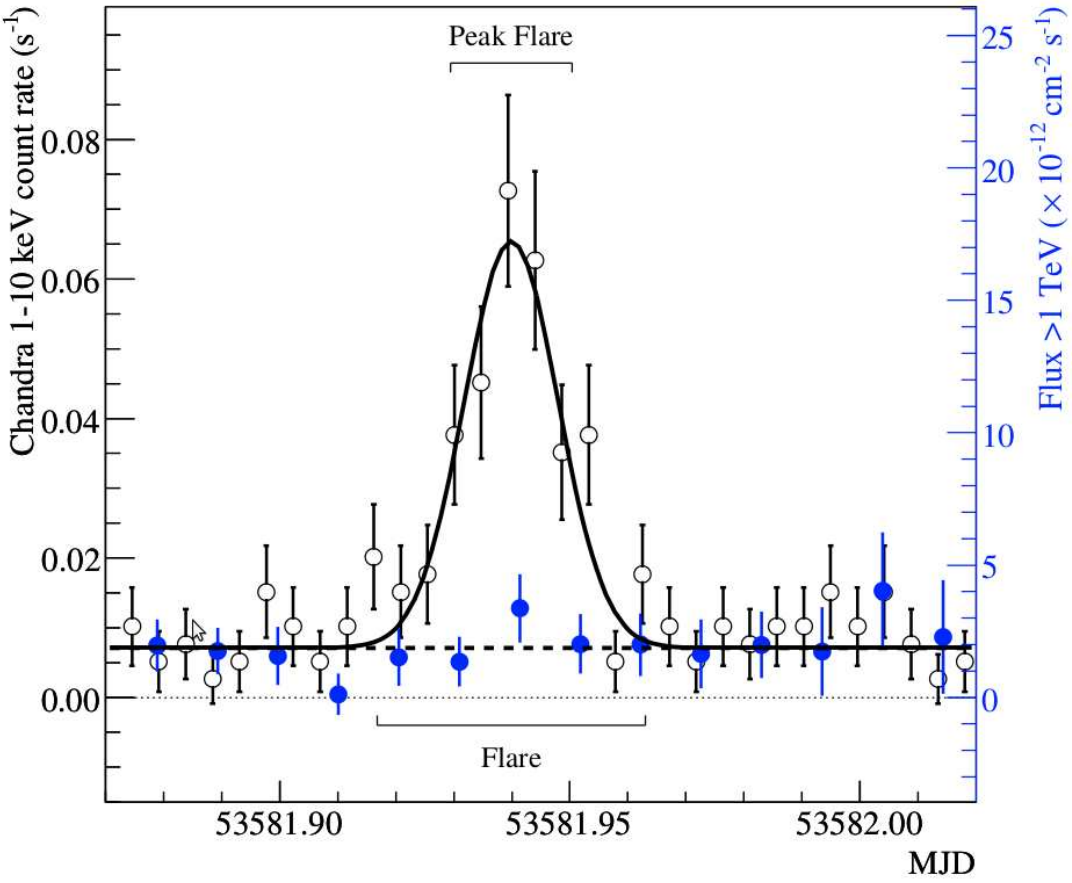

Figure 2.8: X-ray and γ-ray lightcurves for Sgr A* observed with Chandra and HESS. The open circles represent the background-subtracted 0.3-8 keV count rate from within 2.5'' of Sgr A* in 400-s bins. The closed circles represent the VHE γ-ray light curve from HESS, binned in 15 mins and scaled such that the historical VHE flux level (dashed line) matches the quiescent X-ray count-rate. Image taken from [89].

distance of only 3100 Schwarzchild radius. As it is getting close to the pericentre, it will experience stronger and stronger tidal shearing from the supermassive black hole. Eventually, it will be fed into the supermassive black hole, inreasing the accretion rate. Since the Galactic supermassive black hole is the black hole closest to us, the infall of G2 would provide us with the very first chance to observe the black hole feeding process. It is expected that the hot gas and the cloud of G2 will interact strongly, giving rise to a strong shock. The post-shock temperature near pericentre passage will increase, leading to X-ray emission.

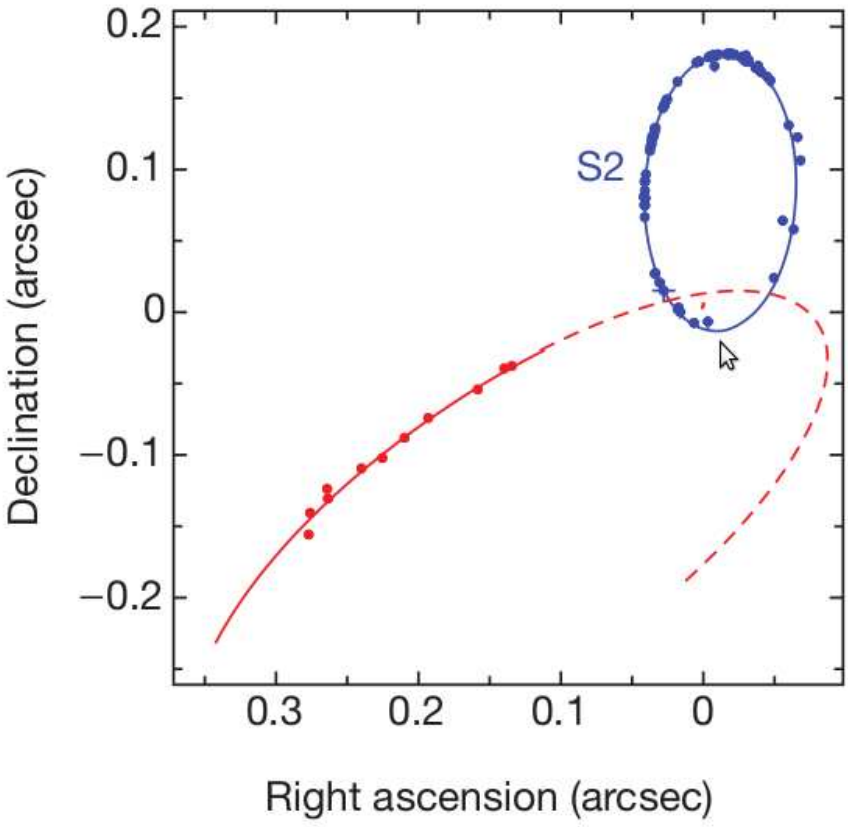

Figure 2.9: The orbit of G2 derived from L' and Brγ astrometric data. Image taken from [90].

Models of G2

The origin of G2 is debated, and a number of models were proposed. These models can be divided into two categories according to whether there is a compact hidden central star enshrouded in a cloud. Here are some models of a pure gas cloud scenario:

• Burkert et al. [91] and Schartmann et al. [92] performed hydrodynamical simulations and reproduced G2's observed kinematical and geometrical properties with a spherical shell model, in which G2 is interpreted as the head of a larger, shell-like structure that formed at apocentre. This model predicts active galactic nucleus activity in the next 30 years after pericentre passage as G2 will break up into a string of droplets.

• G2 may have been formed from the debris stream due to the removal of mass from the outer envelope of a giant star nearby [93]. According to the hydrodynamical simulations, G2 is one of the clumps that the debris stream condenses into with cooling.

Here are some models with a compact hidden star:

• A proto-planetary disc model is proposed by Murray-Clay & Loeb [94] in which

the observed gas cloud is produced by the photoevaporation and tidal disruption of the proto-planetary disc surrounding a low-mass star as it approached the SMBH.

• Miralda- Escudé [95] proposes a similar model involving a circumstellar disk surrounding a star. When a stellar black hole flew by the star, its envelope experienced tidal disruption. This disruption placed the star in the highly eccentric orbit. The cloud is formed by the photoevaporation wind originating in the disk.

There are various simulations demonstrating increase in flux across the whole wavebands during pericentre passage. Narayan et al. [96] estimated the energy distribution of the accelerated electrons via particle-in-cell simulations and found a bow shock in front of the cloud could accelerate electrons to relativistic energies. The non-thermal synchrotron radiation emitted by these electrons are a factor of several above the quiescent radio emission. From fully three-dimensional simulation during pericentre passage, Saitoh et al. [97] showed that G2 would experience strong tidal force by the SMBH. It would be compressed in the vertical direction, heating up and flaring up of the cloud would result. This flare is prominent in the NIR. Using three-dimensional and moving-mesh simulations, Anninos et al. [99] predicted that the spherical cloud G2 supposed to be in pressure equilibrium with the background may increase accretion rate depending on whether the gas is cold or not. If it is hot, most of the gas will be caught in outflows. If cold, it is unlikely to mix well with the hot background gas. Instead, it will be accreted onto the SMBH efficiently. Due to increased accretion driven by the hot emitting gas surrounding Sgr A*, Yusef-Zadeh & Wardel [98] showed that there is significant increase in X-ray and radio emission.

Observations dedicated to G2

In order to catch flares and test different models around pericentre passage, there were many observation campaigns at different wavelengths devoted to G2. Table 2.1 and Table 2.2 summarize the orbital parameters derived for different studies and the observation results dedicated to variability studies carried out around pericentre passage respectively.

Gillessen et al. [100] made subsequent observations with ESO VLT in 2012 and confirmed the eccentricity of the orbit, but a higher value of 0.966 was found. The updated orbit revealed a pericentre passage two months later than estimated before, and even at a shorter distance of 2200 Schwarzchild radius.

In 2013, Phifer et al. [101] made observations using Keck I and Keck II and found the L-band positions had systematic offset, so they used Br-γ line astrometry to locate the orbit instead. They found the pericentre approach to be in early 2014, a closer periastron of $\sim$ 1900 Schwarchild radius and a even higher eccentricity of 0.98. Such a high eccentricity argues in favour of a stellar model and is consistent with a triple star system. They suggested that G2 could be the result of a recent merger between two components.

Gillessen et al. [102] made observations again using ESO VLT. This time they derived the orbit's parameters based on Br-γ astrometry. Part of G2 had already passed the pericentre at that time. The orbital parameters derived are compatible with Phifer et al. [101], a high eccentricity of ≈ 0.98 and a pericentre passage time in early 2014.

Observations were made with Spizer/IRAC at 4.5 microns in late 2013 [103], approximately 100 days before the predicted pericentre passage. No evidence was found in the lightcurve demonstrating activity due to G2 interaction.

Before, during and after pericentre passage, the flux of Sgr A* was monitored at 22GHz using the VLBI [104]. No significant increase in flux was detected. The average flux density was consistent with the usual range of the source. Bower et al. [105]made

broader observations in the low energy band from 1.0 to 355 GHz using the Very Large Array, Atacama Large Millimeter Array, and Submillimeter Array from October 2012 to November 2014. They found no evidence for change in the mean flux density attributable to G2.

In order to monitor the pericentre passage, Witzel et al. [106] launched an observation campaign using Keck II in the K and L' band. G2 was observed to have survived the closest passage intact, causing no increase in L' brightness. After pericentre passage, its motion continued to follow a Keplerian model. These results implied that G2 has a central star surrounded by a thick dust shell.

Table 2.1: A summary of orbital elements of G2 found in different studies

Parameter	Gillessen et al. [90]	Gillessen et al. [100]	Phifer et al. [102]
T_0 [yr]	2013.51 ± 0.035	2013.69 ± 0.04	2014.21 ± 0.14
Eccentricity (e)	0.9384 ± 0.0066	0.9664 ± 0.0026	0.9814 ± 0.0060
P [yr]	137 ± 11 yrs	198 ± 18 yrs	276 ± 111 yrs
p_0 [R_S]	3140	2200	1900

Table 2.2: A summary of results of observations around G2's pericentre passage

Telescope	Waveband	Time of Observation	Flares found?
Spitzer/IRAC [103]	4.5 μm	December 2013	no flares found
Japanese VLBI Network [104]	22 GHz	Feb. 2013 to Aug. 2014	no flares found
Very Large Array [105]	1 to 41 GHz	late 2012 to mid-2014	no flares found
ALMA [105]	218 to 354 GHz	mid-2013 to mid-2014	no flares found
Submillimeter Array [105]	217 to 353 GHz	mid-2013 to late 2014	no flares found
Keck II [106]	L' and K' band	March 2014	no flares found
Chandra [85]	2-8 keV	mid-2013 to mid-2014	increased flaring rate observed

Chapter 3

Air Showers

3.1 Extensive Air Showers

Air shower was first discovered by Bruno Rossi in 1934 while studying cosmic rays with detectors. It is formed when an incident high energy particle strikes the atmosphere and generates secondary particles. These secondary particles further interact with atmospheric molecules, causing the development of the shower. Depending on the particle type, the shower can either be electromagnetic(EM) or hadronic.

3.1.1 Electromagnetic Shower

If the incoming particle is a γ-ray photon, an electromagnetic shower is formed. It first interacts with the nuclues of an atmospheric molecule at 10-20km altitude, forming an electron and a positron as a result of pair production.

$$\boldsymbol{\gamma \rightarrow e^{+} + e^{-}} \tag{3.1}$$

The $e^{\pm}$ then experiences a strong attraction force as it gets close to the nucleus of an air molecule, and is deflected by Coulomb scattering. The $e^{\pm}$ decelerates and gives off a photon as a result of Bremsstrahlung(Fig. 3.1). These secondary particles produced experience Bremsstrahlung and pair production again, forming more secondary particles. In this way, a cascade of secondary particles are produced, leading to an air shower.

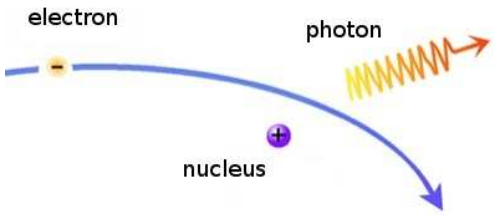

Figure 3.1: An illustration of Bremsstrahlung. When an electron is deflected by the Coulomb field of a nucleus, it decelerates and gives off a photon.

For relativistic electrons, the average energy loss rate per cm path length due to Bremsstrahlung is directly proportional to its energy. The relationship is given by:

$$\frac{dE}{dx} = -\frac{1}{X_0}E \tag{3.2}$$

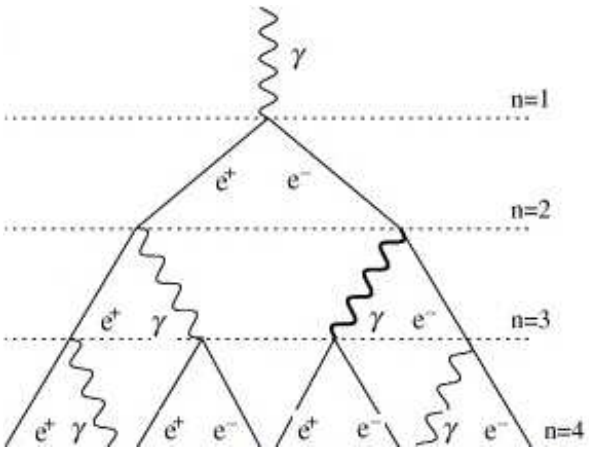

Figure 3.2: Heitler's toy model describing the development of an electromagnetic shower.

where X_0 is the radiation length of the material, usually measured in gcm^{-2}. After passing through the material for a radiation length, the average electron energy decreases to 1/e of the initial energy. This quantity is related to the material's density per cm^3,atomic number Z and mass number A. For Bremsstralung, it is given by [107].

$$X_{0,Brems} = \frac{716.405A}{Z^2[(L_{rad} - f(z))] + ZL'_{rad}}[gcm^{-2}] \tag{3.3}$$

where f(z) is the Coulomb correction and is different with different atoms. L_{rad} and L'_{rad} stand for the following expressions

$$L_{rad} = ln(184.15Z^{-(1/3)}) \tag{3.4}$$

and

$$L'_{rad} = ln(1194Z^{-(2/3)}) \tag{3.5}$$

Assuming a composition of 76.9% nitrogen, 21.8% oxygen and 1.3% argon, for air, the radiation length X_0 is 36.664[g cm^{-2}] [107]. For pair production by a high energy photon, the corresponding radiation length is $X_{0,pair} = \frac{9}{7}X_{0,brems}$. This means that a photon travels a longer track than an electron before undergoing interaction. This can be used to distinguish between photon-induced and electron-induced showers, in which the electron one has a higher first interaction point.

Heitler model [108] (Fig. 3.2)is a simplied model of EM shower development in the atmosphere. In this model, the radiation length for a photon undergoing pair production and an electron undergoing Bremsstrahlung are both taken to be X_0 as an approximation, the factor 9/7 is neglected. Pair production and Bremsstrahlung are considered as the only processes which can produce secondary particles. Another assumption made is that the electron-positron pair produced by pair production share the energy of the original photon equally. The same applies to the photon produced by Bremsstralung, in which the original electron travels a certain "step" and only retains half of the original energy after interaction, the other half goes to the newly produced photon.

According to eq. (3.2), the energy of the particle undergoing interaction becomes

$$E_x = E_0 e^{x/X_0} \tag{3.6}$$

Let's define the "step" as

$$d = X_0 ln2 \tag{3.7}$$

by inserting Eq. (3.7) into (3.6), we have

$$\frac{E_{(x=d)}}{E_0} = e^{\frac{-X_0 ln2}{X_0}} = \frac{1}{2} \tag{3.8}$$

It can be easily seen that after travelling a step of $X_0 \ln 2$, the particle carries half of the original energy. The energy required to produce an electron-positron pair is ≈ 1 MeV/c^2. Since the incoming photon's energy is a lot higher, the shower goes on developing by splitting. After n splittings the shower has 2^n particles in total. Their individual energy is $\frac{E_0}{2^n}$. It stops developing after n* steps when the individual energy drops below the critical energy E_c. The critical energy is about 84 MeV in air. After this point, energy loss due to ionization becomes more dominant and the shower maximum is reached. No more new particles are produced and the shower dies out gradually. As a result, cascade of particles are produced, forming an extensive air shower(EAS). Since the secondary particle travel in the same direction as the primary particle, the light cone is focussed. Finally a light pool with a typical width of $\sim$200 metres in diameter is observed on the ground.

The number of particles at shower maximum is given by

$$N_{max} = 2^{n^*} \approx \frac{E^0}{E^c} \tag{3.9}$$

and the shower depth is given by

$$X_{max} = \frac{ln E_0/E_c}{ln2} X_0 \tag{3.10}$$

For a 1 TeV particle, the typical height of the first intercation is $\sim$ 25 km. The height for shower maximum is $\sim$ 8 km. From equation 3.9, a 1 TeV photon produces $\sim 10^4$ secondary particles at shower maximum. Due to ozone absorption below 300nm, Rayleigh scattering and Mie scattering by aerosols, only about 50 photons m^{-2} can reach the ground.

3.1.2 Hadronic Showers

When a high energy proton hits the top of the atmosphere, nuclear disintegration results. Secondary particles are produced which in turn themselves produce disintegrations. The proton experiences loss of energy and deflection from its incident direction. This interaction can be written this way:

$$Cosmic\,Ray(CR) + Atmospheric\,Nuclei(AN) \rightarrow CR' + AN' + n\pi^{\pm} + m\pi^{0} + other\,mesons \tag{3.11}$$

where CR' is a fragment of the original cosmic ray and AN' are fragments of atmospheric nuclei. The secondary particles produced include neutral and $\pi^{\pm}$ mesons, of which the neutral ones are the most prominent. Neutral pions then instantly decay into photons, producing electromagnetic subshowers.

$$\pi^{0} \rightarrow \gamma, \qquad \tau = 1.8 * 10^{-16} s \tag{3.12}$$

where τ is the decay time. $\pm\pi$ mesons have a longer lifetime. They may either further decay into muons or interact with other atmospheric molecules to produce kaons.

$$\pi^{\pm} \rightarrow \mu^{\pm} + \nu_{\mu}, \qquad \tau = 2.5 * 10^{-8} s \tag{3.13}$$

muons then further decay to

$$\mu^{\pm} \rightarrow e^{\pm} + \nu_{e} + \nu_{\mu}, \qquad \tau = 2.2 * 10^{-6} s \tag{3.14}$$

Since muons are weakly interacting, they have a higher chance of reaching the ground. Interactions of $\pi^{\pm}$ with air molecules:

$$\pi^{\pm} + p \rightarrow p + K^{\pm} + K^{0}, \tag{3.15}$$

Kaons decay by weak interaction in about 10^{-8} seconds by the following processes:

$$K^{\pm} \rightarrow \pi^{\pm} + \pi^{0} \tag{3.16}$$

$$K^{+} \rightarrow \mu^{+} + \nu_{\mu} \tag{3.17}$$

$$K^{-} \rightarrow \mu^{-} + \bar{\nu}_{\mu} \tag{3.18}$$

$$K^{-} \rightarrow \pi^{0} + \mu^{-} + \bar{\nu}_{\mu} \tag{3.19}$$

Due to the complicated development of hadronic shower, it is more longitudinal(Fig. 3.3). The resulting light pool is more irregular and less concentrated than the EM one. The spread in volume is also very noticeable. This can be seen in fig.3.4, which shows the light pool on the ground for a hadronic and EM shower. The EM one has very clear radius due to the focussed light cone while the hadronic one shows heterogeneous

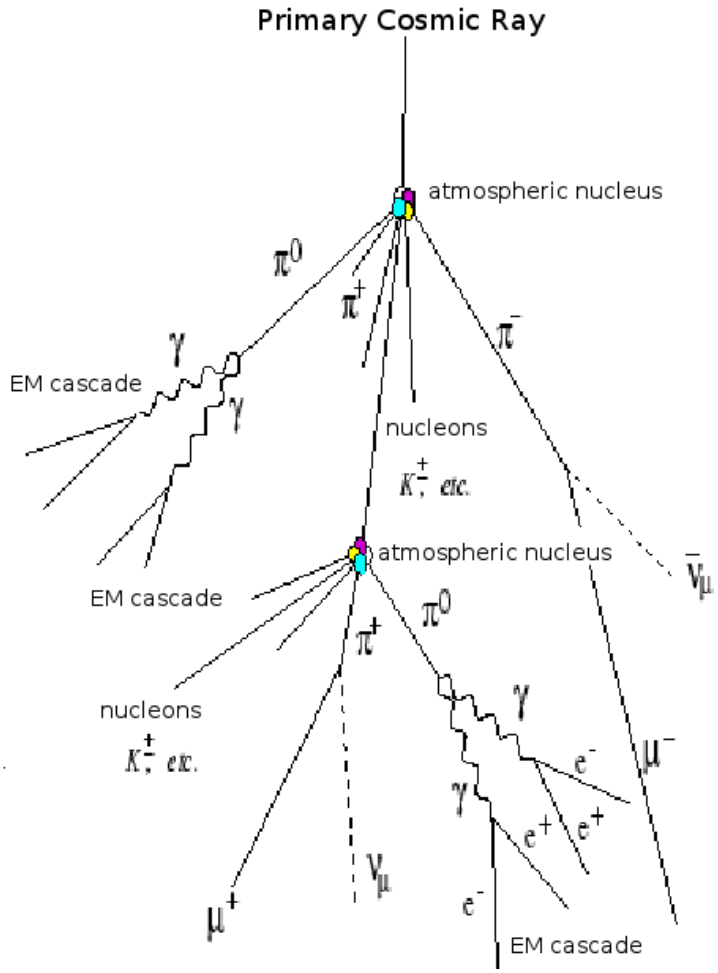

Figure 3.3: Geometric model of emission of Cherenkov radiation for hadronic shower.

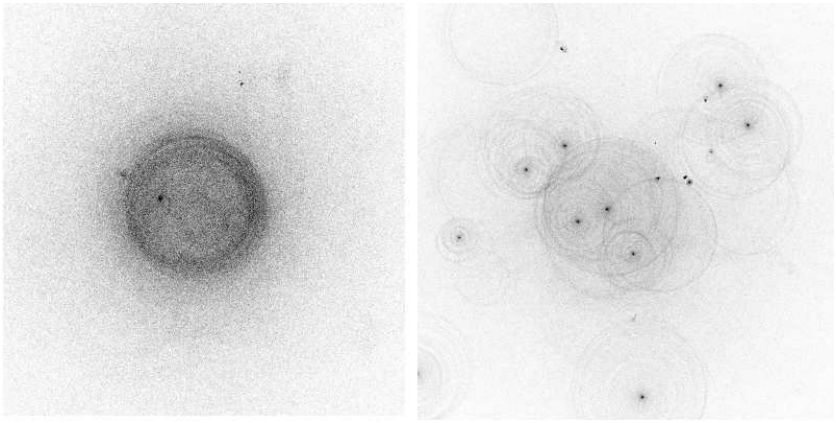

Figure 3.4: Monte-Carlo simulated lateral Cherenkov light distributions on the ground initiated by a 300 GeV γ ray photon(left) and a 1 TeV proton. Image taken from [109].

structures due to the complex longitudinal development described above.

For a hadronic shower, about a third of the original energy is lost due to new particle production at each stage from pion decay. Thus the total energy of the initiating particle is split into two channels - hadronic and electromagnetic. The primary energy of the original cosmic ray proton is linearly proportional to the combined number of EM particles and muons.

3.1.3 Cherenkov Radiation

Cherenkov radiation was first observed in the early 1900's by Mary and Pierre Curie while doing experiments on radioactivity emission. At that time, the nature of the phenomenon was unknown. In 1926, Mallet tried to study it and found emission of bluish-white light when transparent bodies were placed close to a radioactive source. However, he could not find out the nature of it. In the 1930s, P.A. Cherenkov carried out experimental work and I. E. Tamm and I. M. Frank [110] gave a theoretical interpretation, then this phenonmenon began to be understood and recognized. In 1953, Galbraith and Jelley detected Cherenkov radiation by observing light pulses from the night sky and the experimental search for Cherenkov radiation in the atmosphere began.

When an electron moves slowly through the atmosphere, the atoms whose original shape are roughly spherical in it become distorted due to the electric field generated by the passing electron. The atoms around the electron would then become polarized(fig. 3.5 left). As the polarization field is symmetric, there is no resultant field at large distance. Thus, no radiation is produced. However, if the electron is travelling fast enough, the polarization field would no longer be symmetric along the axis of travel since there is not enough time for the atoms to return to the equilibrium position (Fig. 3.5 right). As a result, a temporary dipole field is set up along the track. The molecules are then excited. When these molecules return to the ground state, photons are emitted as an electromagnetic pulse. If the velocity of the electron is faster than the phase velocity of light in the atmosphere, there is possibility for the wavefronts from parts of the track to interfere constructively. The radiation formed is called Cherenkov radiation.

As can be seen from Fig. 3.6 , this radiation is observed at a certain angle θ called Cherenkov angle with respect to the electron's track. This angle represents the position in which waves from points such as P, P1, P2 and P3 over the track AB are coherent. They combine to form a plane wavefront BC. This coherence takes place when the

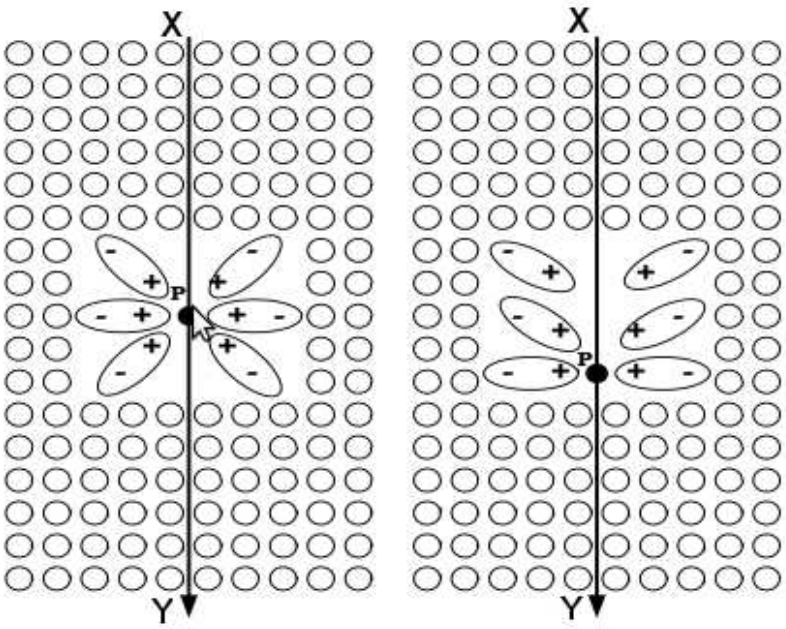

Figure 3.5: Polarization set up in the atmosphere due to a charged particle

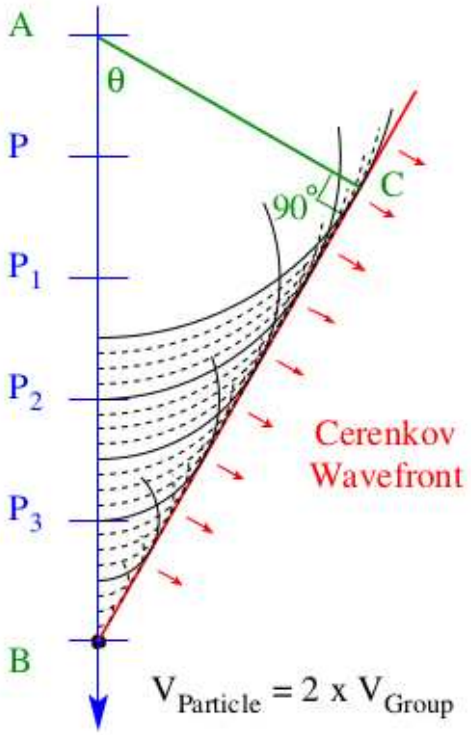

Figure 3.6: An illustration of the geometrical interpretation of the emission of the Cherenkov radiation.(Figure from [111])

particle travels from A to B in the same time that the light travels from A to C. Suppose the velocity of the electron is βc, where c is the velocity of light in vacuum, β is the ratio between the speed of the particle in the atmosphere and the speed of light, i.e. v_p/c, the refractive index of air is n, and the travelling time of AB is t, we have

$$cos\theta = \frac{\frac{c}{n(\lambda)} \times t}{\beta \times c \times t} \tag{3.20}$$

$$cos\theta = \frac{1}{\beta \times n(\lambda)} \tag{3.21}$$

$$cos\theta = \frac{c}{v_p \times n} \tag{3.22}$$

For the relativistic case, v $\sim$ c, thus cos $\Theta = \frac{1}{n}$. Since cos$\Theta \leq 1$, there exists a threshold velocity $v_{threshold} = \frac{c}{n}$. From the relativistic formular, E = γmc^2, where $\gamma = \frac{1}{\sqrt{1-\frac{u^2}{c^2}}}$, the energy threshold for Cherenkov radiation is $E_{thresh} = \frac{nmc^2}{\sqrt{n^2-1}}$. As can be seen from the this formular, the energy threshold is directly proportional to the mass of the charged particle for a given refraction index. The refractive index of air at sea level is 1.00029, the corresponding opening angle of the light cone is 1.3°. The threshold energy is 21 MeV for electrons, 4.4 GeV for muons and 39 GeV for protons.

3.2 Imaging Atmospheric Cherenkov Technique

Since the Cherenkov radiation generated in the EAS carries important information about the source, experimental device is used to extract these information. The first experiments began in the 50's by the British Atomic Energy Research Establishment in Harwell. The group was able to detect Cherenkov light pulses using a garbage can with parabolic mirror inside and a photomultiplier tube placed on its focal length. In 1968, the first Cherenkov telescope was bulit and the technique began to develop since then.

Imaging Atmospheric Cherenkov Technique, as its name suggests, takes an image of Cherenkov light emitted by secondary particles in air showers by collecting the Cherenkov photons. Basically a Cherenkov telescope consists of a parabolic reflector and a camera placed on the focal plane. Due to financial reasons, the reflector is usually made out of smaller mirrors. The mirrors are placed either on an azimuthal mount or an equatorial mount for support. Due to the short duration (a few nanoseconds) and low intensity of an air shower, fast electronics are required. Thus, the camera pixels are made of photomultiplier tubes (PMTs) which ensure rapid readout of signals. The number of pixels and its angular size are especially important because they determine the field of view and minimum angular resolution.

Due to the night sky background, cosmic ray showers and single muon events, stereoscopic technique, which adopts a multi-telescope array, was developed. The HEGRA system did pioneering work in 1996 [112]. This technique can largely lower the trigger threshold as it requires simultaneous trigger of more than one telescope. Thus, random triggers by night sky background and local muons (as mentioned in Section 3.1.2, muons have a small light cone and only trigger a single telescope) are reduced. Stereoscopic prin-

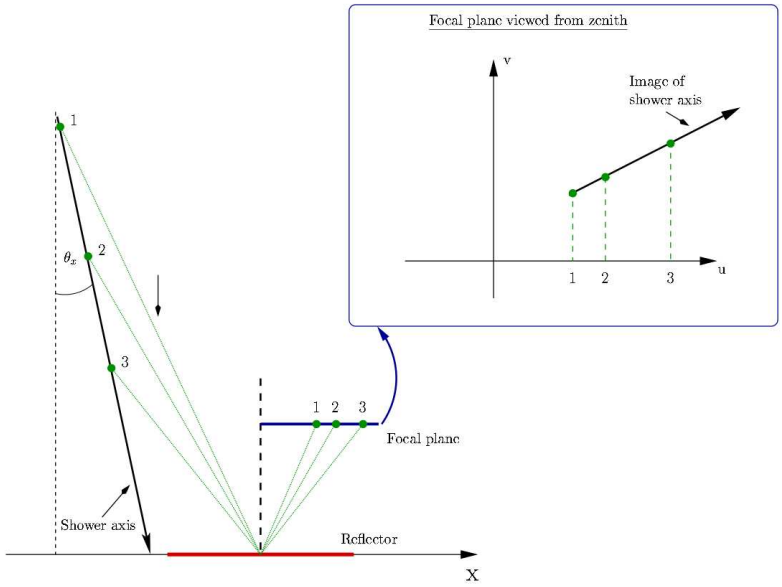

Figure 3.7: Mapping of the shower axis into the focal plane of a telescope. The inset shows the orientation of the image depends on the inclination of the shower with respect to the telescope optical axis. Image adapted from [113]

.

ciple also greatly improves shower reconstruction and γ/hadron separation as showers are seen from different angles.

Since Cherenkov light is emitted by the primary particle, it carries information about its properties, e.g. energy, type and direction. The images recorded on the camera planes reflect such properties. Hence, mapping rules are developed which allow to resolve the details of the image so that these properties of the primary particle can be reconstructed.

As a first step to analyze shower images, the position on the camera plane has to be known. This is related to the source position. For a point (x,y,z) in the atmosphere, the mapping rule to the camera is:

$$\begin{pmatrix} u \\ v \end{pmatrix} = -\frac{f}{z} \begin{pmatrix} x \\ y \end{pmatrix} \tag{3.23}$$

where(u,v) are the coordinates in the camera, f is the focal length of the mirror. In fig. 3.7, three points from the shower 1,2,3 are mapped onto the camera plane. The extrapolation of the image axis of one side in the focal plane points leads to the shower impact position on the ground while the other side points towards the source position.

Figure 3.8 schematically shows the principle of imaging an air shower onto the camera plane. The image is a two-dimensional projection of the shower. The resultant image is ellipsoidal. The major axis, i.e. length, of the shower is determined by the angle $\Delta\phi = \phi_2$-ϕ_1, under which the shower is observed. The position of AB on the camera plane is determined by R, which is the distance on the ground between the reflector mirror and shower. The larger it is, the further away AB is from the camera centre and the more elongated the shower appears on the plane. The major axis points back to the direction of the shower. The lateral view of the shower is shown in Fig 3.8 right. The width of the image on the camera plane is determined by the lateral extension of the shower. The

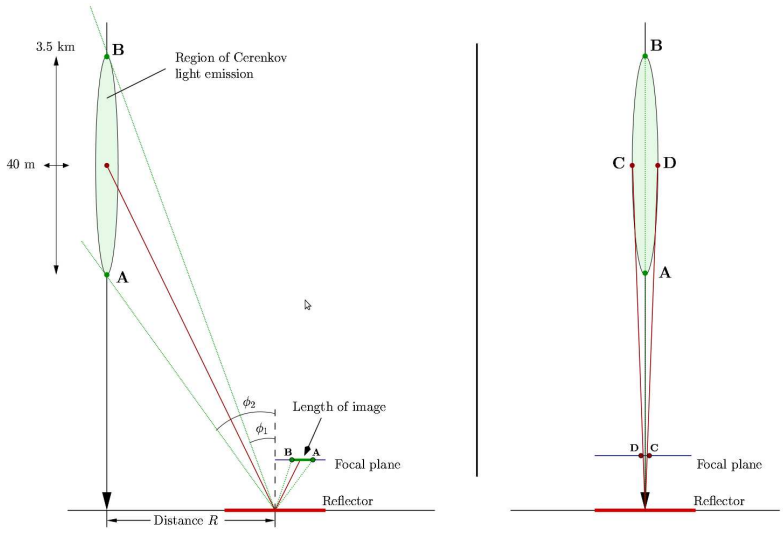

Figure 3.8: A sketch of the imaging geometry explaining basic dependencies between showers and camera images. Left: View of the plane spanned by the shower axis and the telescope position. Length and position of the image are determined by $\Delta\phi = \phi_2$ -ϕ_1 and R. Right: Perpendicular view from the telescope towards the shower. Distance to the telescope and the lateral spread of the shower determines the width of the image. The points A,B,C,D are drawn and to be compared with Fig. 3.9. Image taken from [113].

two-dimensional sketch of the camera image is illustrated in Fig 3.9. The shower image is symmetrical along the AB axis but not CD due to the non-linearity of the imaging as given by Eqn. 3.23. The length and width are robust parameters in determining whether a shower is electromagnetic or hadronic. Since EM showers are single-cored, the spread of the shower tend to be smaller, the images are more elongated and narrower compared to the multi-cored hadronic ones. Moreover, the primary particle's energy, the distance between the telescope and the reconstructed shower impact point can be estimated from the image intensity.

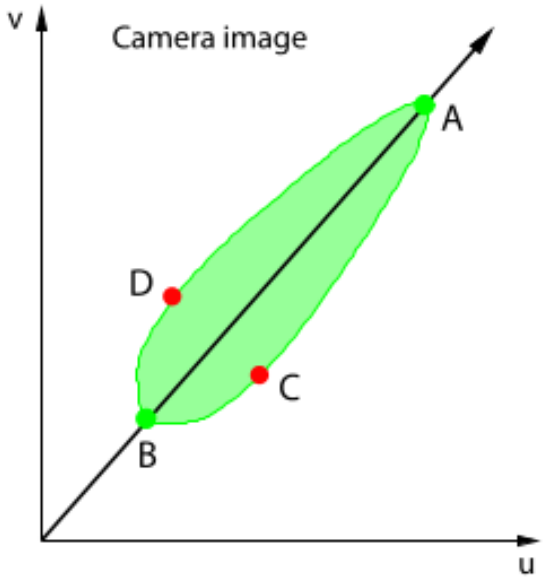

Figure 3.9: Image of an air shower mapped onto the camera. Due to non-linearity of the mapping rule, the image appears not perfectly ellipsoidal.Image taken from [113].

Chapter 4

The H.E.S.S. Experiment

4.1 H.E.S.S. site

H.E.S.S. is an array of five imaging atmospheric Cherenkov telescopes, located in the Khomas highlands of Namibia(23° 16 18 South, 16° 30 00 East) at 1800 m above sea level (see Fig. 4.1). This site was chosen because of its height, clear cloudless nights and low humidity [114]. It has been shown that 57% of the moonless darktime is cloud-free and that the relative humidity was below 90% in 94% of the nights. Its location in the Southern hemisphere made H.E.S.S. in large parts devoted to the search for VHE gamma rays from Galactic sources. In autumn to winter time in Namibia, the Galactic Centre is at optimal position for observations.

4.2 Layout

Phase I of HESS has four telescopes, each has a 12m dish. They came into full operation in 2003. The telescopes are arranged in a square of a length of 120m. The Cherenkov light pool has a diameter of 250m. If the spacing is too large, it is unlikely that the same shower would trigger at least two of the telescopes at the same time. If too small, good stereoscopic viewing cannot be guaranteed. This distance was optimised for maximum sensitivity at the planned energy threshold of 100 GeV. For phase II of HESS, a bigger telescope with a 28 m dish is placed in the centre of the square. It saw its first light in 2012.

4.3 Mirror Systems

For a HESS I telescope, the dish is made up of 382 round mirrors, each of which has a diameter of 60 cm, amounting to a total area of 108 m^2. The mirror has a d/f ratio of 0.8 and a focal length of 15 m. For a wavelength of 300 to 600 nm, the reflectivity of a mirror is $> 80\%$. For the HESS II mirror, the focal length is 36 m. It is made up of 875 hexagonal facets of 90 cm diameter each. The total area is 614 m^2. Due to loss of reflectivity, the mirrors have to be recoated once in every five years.

Every mirror is slightly tilted so that they can accurately reflect the shower's image in the camera. Mirror alignment is done with an automatic procedure called Mirror Alignment Control System (MACS). The mirror facets are mounted onto supports equipped with two motor-driven actuators which allow individual mirror adjustment. A CCD camera(lid CCD, see fig. 4.2) is placed at the centre of the dish which views the image of a star on the closed lid of the PMT camera. Before alignment, the image might not appear as a single spot(Fig. 4.3). Every facet is aligned in both axes until a single spot which is smaller than the size of a pixel is formed at the centre of the camera. Other than the lid CCD, there is also a sky CCD mounted off-axis which serves as a guide

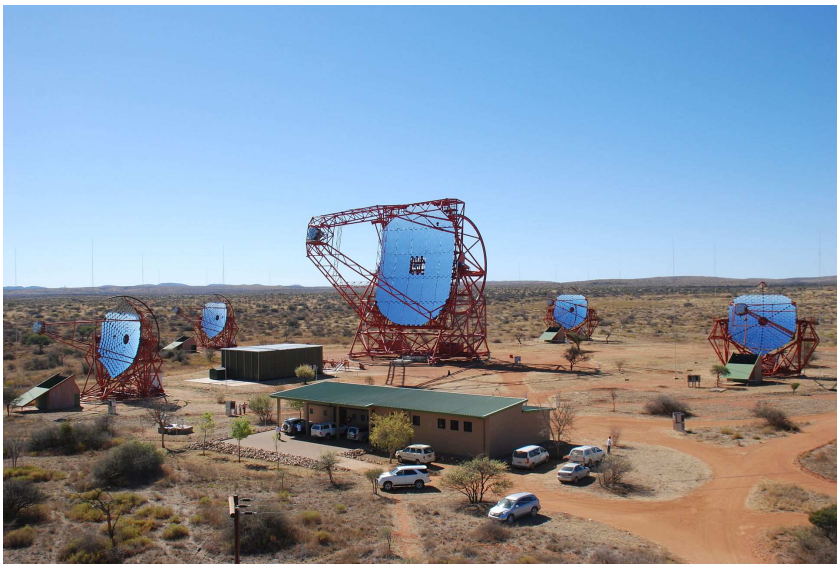

Figure 4.1: A picture of the H.E.S.S. site

telescope to correct deviations from perfect pointing. Deformations of camera masts also affect mirror alignment. There are eight LEDs mounted at the corners of the PMT which serve to monitor them.

The goodness of the alignment of the mirrors is defined by the point spread function(PSF). Due to the single-mirror design without corrective elements and the telescopes' modest f/d ratios, there are significant optical aberrations. The width of the PSF is expected to grow linearly with the angle θ to the optical axis. The following parameterization is used to describe the PSF as a function of angular distance θ to the optical axis

$$r_{80\%} = (0.42^2 + 0.71^2\theta^2)^{1/2}[mrad] \tag{4.1}$$

$r_{80\%}$ means the radius containing 80% of the total intensity. Telescope pointing is another source of variation in the PSF. This gravity-induced deformation is to a good approximation is described by

$$r_{80\%} = (0.41^2 + 0.96^2(sin\Theta - sin66^\circ)^2)^{1/2}[mrad] \tag{4.2}$$

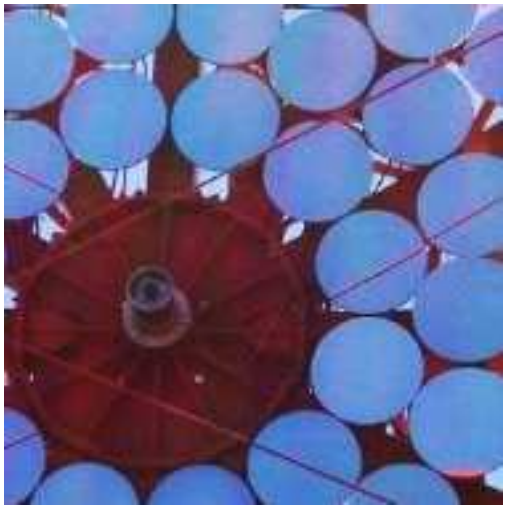

Figure 4.2: A picture of the lid CCD placed at the centre of each telescope.

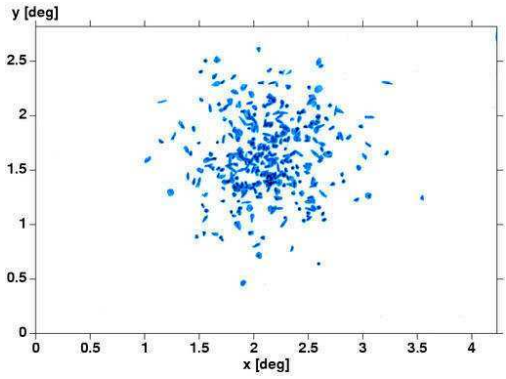

Figure 4.3: Image of a star on the camera lid before alignment. Each spot corresponds to a mirror facet. The coordinates x, y refer to the CCD image translated into degrees. Image taken from [115]
.

Figure 4.4: Left: The camera of a H.E.S.S. I telescope. Right: A close-up view of the H.E.S.S. II camera showing the photomultipliers and Winston cones

4.4 The H.E.S.S. Camera

Each telescope has a camera installed at the focal plane of the mirror. The HESS I cameras have a hexagonal array of 960 photo-multipliers(PMTs), each of which subtends an angle of 0.16°, resulting in a total field of view of 5°. The HESS II camera has 2048 PMTs. Each has a size of 0.067°. The total FOV is 3.2°. The front part of both HESS I and HESS II cameras contain drawers. Each of them has 16 PMTs [116]). The quantum efficiency of the PMTs is at a maximum of about 30%. The drawers contain the trigger and readout electronics, high voltage(HV) supply, control and monitoring electronics.

Winston cone is a non-imaging light concentrator placed in front of the PMTs. They can avoid dead areas caused by the insensitivity at the outer edges of the PMT cathodes and the support structure in between PMTs. It is optimized for a sharp angular cutoff, thus reducing noise due to scattered light from the ground or from the sky when the telescope is making low elevation observations. About 75% of the photons reflected from the mirror can be collected by the cones. A picture of the H.E.S.S. cameras is shown in Figure 4.4.

4.5 The Central Trigger System

The central trigger system (CTS) of H.E.S.S. employs a multi-telescope array level trigger. If a minimum number of pixels in a sector has a signal above a threshold of N photoelectrons, coincident in a trigger window of $\sim$ 1.3 ns , the camera is triggered. Signals are then digitized and sent to the central trigger system [117] as well as the central data acquisition system (DAQ) by optical ethernet connection [118]. The CTS would then check for multiple telescope coincidence requirements. At a low energy level, single telescope triggers are dominated by random night-sky background(NSB) light. Local muons with a very narrow Cherenkov light cone can also easily cause triggers. At a high energy level, they are dominated by hadronic showers. In this way, the random NSB and single telescope triggers caused by muons are then reduced at the hardware level. The energy threshold of the system could then be lowered. In case of active trigger from only one telescope but no telescope multiplicity occurs, a reset signal is sent to the camera. Then, the event would be discarded and the camera is immediately ready for the next event.

The coincidence trigger window should be of a suitable width so that it can effectively avoid random telescope conincidences and does not miss the real ones. The minimum achievable window lies in the intrinsic spread in the arrival times of telescope triggers at the central station. This spread is mainly due to the width and curvature of the

Cherenkov wavefront and the field-of-view of the cameras. The coincidence window of H.E.S.S. is set to be 80ns.

Dead-time is important in the determination of spectra and fluxes of astrophysical γ-ray sources. The CTS records every Cherenkov event triggering the array, storing information on which telescopes are able to provide data for a particular event, as well as on those that are triggered but are busy reading out the previous event. These information are used in the determination of the system dead-time.

4.6 Drive System

The drive system of HESS I has a servo-controlled AC motor and a backup battery-driven DC motor for each axis. It acts on a circular rail of around 7 m radius. For HESS II, it is driven by four 28 kW servo motors. They are pair-wise torque-biased and synchronized through a state of the art Programmable Logic Controller (PLC). For both telescopes, the maximum speed can reach 100°/min. This allows a fast repositioning and a minimal settling time. In case of GRB alerts, the telescope can quickly change from one direction to another.

4.7 Data Acquisition System

Each of the five telescopes of H.E.S.S. is a heterogeneous system which has several subsystems including a camera with individual photo-multiplier tubes, light pulser systems for calibration purposes, a source tracking system, an IR radiometer for atmosphere monitoring, and a CCD system for pointing corrections. The weather station, ceilometer and all-sky radiometer are common to the whole array. They serve to monitor the atmopheric conditions. All these call for a central system, the data acquisition system (DAQ), which provides the connectivity and readout of all the systems mentioned above.

The DAQ takes over run control, the recording of events and slow control data, error handling, and monitoring of all subsystems. The system must also allow easy inclusion and removal of new hardware without major reconfiguration. The DAQ therefore has to be based on a flexible framework that allows communication between very different systems, running on different hardware architectures and running different operating system.

The DAQ is a multi-machine, multi-process, multi-threaded system with more than 100 different processes called controller spread over about 23 machines and dedicated hardware. The communication between the different processes is built on the CORBAdistributed, object-oriented inter-process communication standard. The ROOT Data Analysis Framework provides a serialization mechanism for the transport and storage of objects.

All hardware used by the DAQ is represented by a Controller, which is a software process running on the DAQ cluster. It interacts with the hardware directly and reads out the data. The Controllers then send data to intermediate Receivers by Push mode, which can then perform further processing and store the data. The Receivers allow other processes to sample processed data by Pull mode, in which a client pulls the server process for new data in periodic intervals. This transport mechanism is used by displaying processes where a subsample of the data is enough. The whole process is shown in Fig. 4.5.

In order to standardize the operations on the controller, each DAQ process contains a StateController object which maps the state of the hardware to the state of the corre-

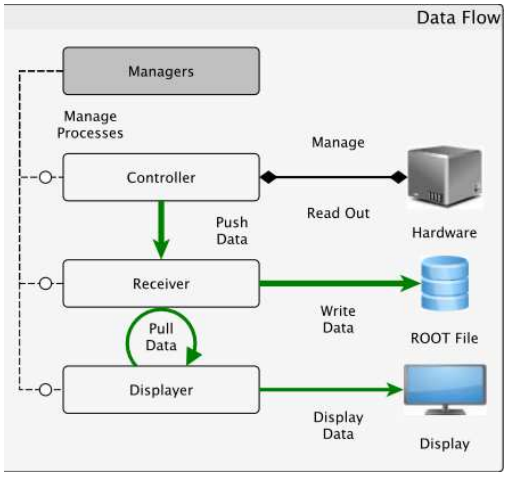

Figure 4.5: An illustration of the H.E.S.S. DAQ data flow. The data from the hardware is first sent to the Receiver through Push mode. The received data is then stored in ROOT files. By using the Pull mode, the data can be displayed on the screens in the control room for fast feedback. The Manager handles error and synchronizes processes. Image taken from [119]

.

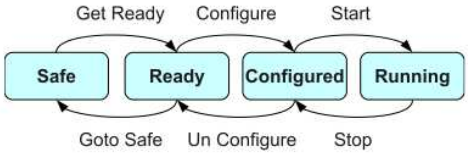

Figure 4.6: Machine states and transitions for the H.E.S.S. DAQ. The boxes represent the available states for a Controller while the arrows represent the available transitions. Image taken from[120]

.

sponding Controllers. The states and corresponding transitions are shown in Fig 4.6. If a Controller is in the Safe state, the corresponding hardware is either turned off or in a state of minimal activity. In the Ready state, Controllers are preparing for data taking. The Configured state is an intermediate step before data taking, which indicates that the hardware has received all the necessary configuration parameters from its Controller. Finally, if a Controller is Running the corresponding hardware is read out and the data are processed by the DAQ and stored on disk.

The overall coordination of data-taking is implemented by a dedicated run manager (Fig. 4.7) that can handle several data taking tasks at the same time. Setting up the required processes for a particular run type is simplified by combining related processes in groups called contexts. An example for a context is CT1 which comprises all Controllers accessing the hardware of telescope number 1. Every context contains one Manager which is responsible for synchronizing the different processes in the context during data taking. Managers take care of the distribution of the run configuration to their subordinated processes as well as state transition of each of the controllers belonging to the context. During data-taking a central DAQ Manager first reads the observation schedule from the database and decides the run sequences according to the availability of contexts.

The H.E.S.S. central DAQ has worked for more than 10 years since the inauguration of the first telescope in 2003. The flexibility, evolutiveness and easy scalability ensure smooth operation of the experiment. Due to its high stability, the central DAQ has only

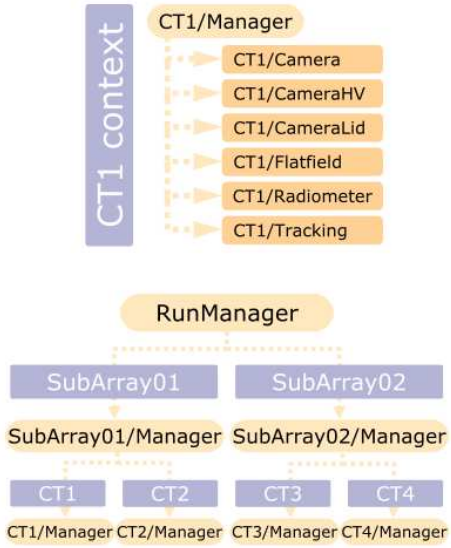

Figure 4.7: Run Control in H.E.S.S. Image taken from mathieus thesis p.59

.

contributed to a loss of 0.8% of the available dark time since 2009.

Such flexible and evolutive systems are clearly required for next-generation instruments such as CTA, which incorporate many independent devices that need to cooperate closely during data acquisition.

4.8 Atmospheric Monitoring

The Cherenkov light densities depend largely on atmospheric conditions. In order to accurately relate the intensity of the Cherenkov light pool and the energy of the incident particle, atmospheric parameters and transmission need to be known. Vast simulations have been performed and different instruments are used at the H.E.S.S. site to probe the atmosphere which include 1) one radiometer per telescope 2)a scanning radiometer 3) a LIDAR 4) an optical telescope ATOM and 5) a weather station

Corsika simulations modelling different atmospheric density show light differences of 60% between tropical and antarctic winter profiles. For the same profile, the differences between average summer and winter can be as large as 15-20%. As a result, shower simulations should adopt appropriate profiles and take seasonal effects into considerations.

Each telescope has an infrared radiometer, Heitronics KT 19, which measures the IR radiation of the water in clouds in the field of view of the telescope. Clouds and water vapour play an important role in the count rate of an IACT. Clouds manifest themselves through an increase in the sky temperature. Water vapour content has an effect on the transmissivity of the atmosphere. The Heitronics KT19.82A Mark II is a scanning infrared radiometer which calculates the sky temperautre by measuring the infrared radiation of the sky. In addition to this, the radiometer can also determine the water vapour content in the atmosphere.

In order to monitor atmospheric transmission due to light-attenuating aerosols, a LIDAR is used. It mainly detects backscatter due to aerosol scattering. The in-built algorithms can invert the backscatter profile to recreate the optical density profile for the atmosphere. Then this profile can be used to compare with the simulated model

atmospheric profiles for the calculation of extinction.

The Automatic Telescope for Optical Monitoring(ATOM) was installed at the site in 2008. This all-sky camera performs astrometric comparison with a theoretical night sky model. The absence of stars is interpreted as cloud coverage. Observation would stop if cloud coverage indicates rain in a short time. In addition, ATOM also serves as a tool for a meteorological analysis of the observation site of the Cherenkov Telescope Array.

Chapter 5

Data Analysis

5.1 Hillas Analysis

In this section a brief summary of H.E.S.S. data analysis scheme is given. Section 5.1.1 describes event reconstruction. Section 5.1.2 is about the calculation of shower parameters. Section 5.3 is about background modelling, spectrum and lightcurve determination.

5.1.1 Event Reconstruction

Preliminary processing

Both non-ideal atmospheric conditions and hardware problems worsen data quality. Thus, before the first step of analysis, the data have to pass certain criteria to guarantee quality. In order to exclude data where clouds passed through the field of view, cuts on the stability of the system trigger rate are applied. Dust reduces atmospheric transparency, so a cut on the absolute system trigger rate is imposed. Requirements are also placed on the absolute value and the RMS on the trigger rates. If there are technical problems, meteorites or bright stars, PMTs are turned off. The number of PMTs not in operation has to be less than 10%. Artifacts and bad reconstruction quality would result if broken pixel rate is too high. The mirror reflectivity worsens over timescales of years. In order to monitor this, the optical response of each telescope has to be extracted using muon rings.

Image Cleaning

This process serves to remove noisy pixels whose intensities are not due to Cherenkov light but PMT noise or night sky background. This is done by a two-step procedure in which pixels fulfilling certain intensity cuts are kept. The first step is the so-called tail-cut, in which a pixel with an intensity of more than 10 p.e. and a neighbouring pixel more than 5 p.e. is kept, or, a pixel with an intensity of more than 5 p.e. and a neighbouring pixel more than 10 p.e. is kept. In the second step, a pixel passing this tail-cut but the intensity does not exceed 3σ of the RMS of the pedestal is removed.

Direction Reconstruction

The shape and intensity of shower images contain important information about the direction, energy ands morphology of the γ-ray source. In order to extract these information, Hillas parameters [121] of the images are calculated. The shower images are parameterized by a two-dimensional ellipse. The position of the shower is indicated by the centre of gravity (COG). The length and width measure the size of the image. α and ψ contain information about orientation. Fig 5.1 shows these parameters.

As H.E.S.S. adopts a stereoscopic approach, for each shower image, there are at least two cameras recording one image. The shower direction is located on the major axis of the ellipse for each shower image. Hence the origin of the primary particle can be recovered by intersecting the major axis of the ellipses from the different cameras. This method is sketched in Figure 5.1. For individual events, the difference between the

true and reconstructed direction is on average less than 0.1°. This angle determines the angular resolution which is discussed later in this chapter. By the same principle, the shower impact point on the ground is determined. The plane which contains the shower axis and core of each shower image is orthogonal to the camera plane. The different planes of the shower images taken by different cameras intersect the ground in a straight line. The intersection point is the impact position.

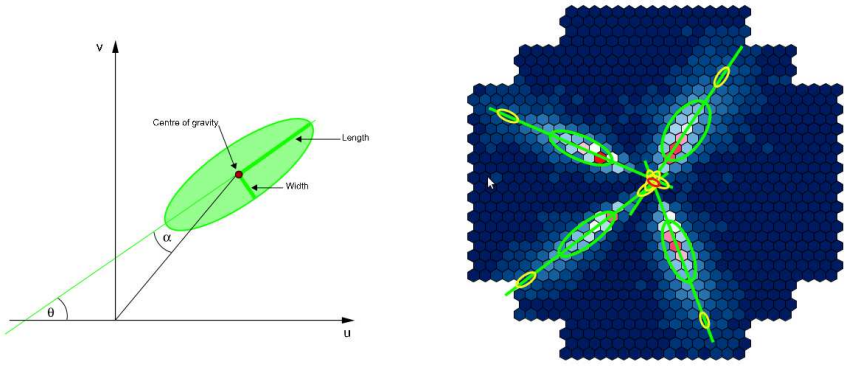

Figure 5.1: Definition of Hillas parameters (left) and the geometrical technique for source position reconstruction (right). Image taken from Berg (2006).

5.1.2 Hadron/gamma separation

Once the image parameters are determined, they can be used to classify the images as hadronic or γ-ray. As mentioned in Chapter 3, hadronic showers are more irregular. The widths and lengths can be used as a means to separate hadronic and γ-ray shower images. They are compared to the mean values obtained from Monte Carlo simulations. The simulations take into account the zenith angles, impact distance, offset and primary energy of the particle since these affect the image shape. The difference between real data and simulations are quantified using the mean reduced scaled width (MRSW) and mean reduced scaled length (MRSL). These parameters are defined as the mean difference in units of standard deviation between the measured image width (length) and the expected value from simulations. It is averaged over all telescopes taking part in the same event taking:

$$MSRW = \frac{1}{N_{tel}} \sum_{i=1}^{N_{tel}} \frac{width_i - < width >_i}{\sigma_i} \tag{5.1}$$

and the same for MRSL. In the above equation, <width>$_i$ is the mean simulated width, σ_i its RMS spread. These cuts are called shape cuts and can reject the majority of hadronic background.

For γ-ray showers, further cuts have to be applied to guarantee image qualities. Images with COG within 2° of the camera centre are kept so as to avoid incomplete images taken by cameras (nominal distance cut).

Fig. 5.1 shows the distributions of MRSW and MRSL for simulated γ-ray and hadronic shower and real off data. These two parameters demonstrate quite strong power in separating gamma-ray and hadronic showers. The simulated protons agree well with real off data, meaning that the background is well understood. By selecting a certain range of

MRSL and MRSW, different numbers of γ-ray events and protons are included. Depending on the source nature, dfferent cuts are applied on MRSW and MRSL in post-selection for γ-like event selection. These cuts are optimized so that maximum detection significance can be achieved. Moreover, to further suppress the residual hadronic background, a directional cut θ^2, which is the square of the angular distance between the simulated shower position and the reconstructed position, is applied since hadronic background is isotropic.

For standard H.E.S.S. analysis, hard, std and loose cuts are used. They are summarized as below:

• Hard cuts: Optimized for weak sources having $\sim$1% flux of Crab Nebula and a rather hard spectral index of $\sim$2.0. It has the most strict cut on the shape parameters (See Table 5.1). An image intensity of at least 200 p.e. is required. This can effectively reject badly reconstructed events but the energy threshold is higher.

• Standard cuts: Optimized for sources with a flux level $\sim$10% of the Crab Nebula and an index similar to it, i.e. $\sim$2.6. The image intensity is at least 80 p.e.

• Loose cuts: Optimized for strong sources with a flux of the same level as the Crab Nebula, but a steeper spectral index of $\sim$3.0. Because of the steeper spectrum, a lower energy threshold is required. Thus, the image intensity is above 40 p.e. only.

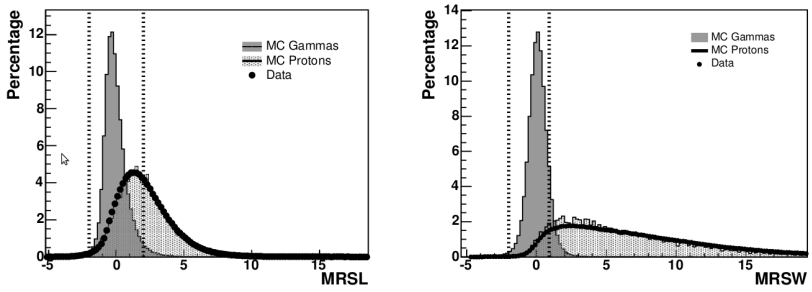

Figure 5.2: Shown is the distribution of mean reduced scaled width (MRSW) (left) and mean reduced scaled length (MRSL)(right) for Monte-Carlo simulated γ-ray data for a zenith angle of 20°. The vertical dotted lines are the cut-values for standard cut for γ-ray selection. Image taken from [122].

Table 5.1: Optimized values for the different γ-ray selection cuts for point sources. Cuts are optimized on MRSW, MRSL, squared angular distance(θ^2) between reconstructed and simulated shower direction, and image size.

Cuts	MRSW (min max)	MRSL (min max)	θ^2(deg^2)	size p.e.
hard	-2.0 0.7	-2.0 2.0	0.01	200
standard	-2.0 0.9	-2.0 2.0	0.0125	80
loose	-2.0 1.2	-2.0 2.0	0.04	40

5.2 Multivariate analysis technique for hadron/gamma separation

The Hillas standard analysis has long been used for hadron-γ separation. By considering the shape of the shower images, cosmic-ray background can largely be reduced. However, due to the complex relationship between shower parameters, simply cutting on a range of

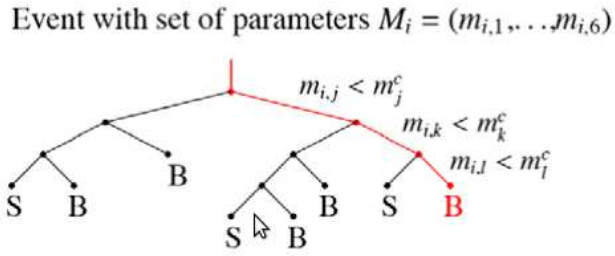

Figure 5.3: A sketch of a decision tree. At each branching, an event is compared to binary split criterion until it ends up in a leaf where it is marked as signal- or background-like. Image taken from [123].

MRSW and MRSL is not an ideal way for hadron-γ separation. A multivariate analysis technique [123] based on a tree classification method, Boosted Decision Trees (BDT), provided by the TMVA package is developed [124].

An example of decision trees [125] [126] is shown in Fig. 5.3. At each branching, a binary split criterion is applied on the input parameters which classify the events as signal-like or background-like. The criteria are based on a set of background or signal events. "Training" refers to the determination of these criteria.

Since single decision trees may induce bias due to instability against statistical fluctuations, the tree is extended to a forest of decision trees having different binary split criteria. Finally, a weighted mean vote is given to the BDT and describes the likeliness of an event as signal or background. This vote stabilizes the response of the classifier and improves its performance.

5.3 Background Modelling

After applying different cuts described in Section 5.1 on the dataset, γ-like events are selected. However, there are still some other γ-like events in the background which cannot be excluded. In order to extract the γ-ray signal from the source, the background events have to be removed. For background estimation, different techniques are applied which serve different purposes.

In this work, the ring background method is used to generate the sky map for morphology studies and the reflected-background method is used for spectral analysis.

5.3.1 Signal Determination

Since the excess events N_γ extracted from the source position contain background events, they have to be removed in order to extract the significance of the γ-ray signal. Given the number of events N_{ON} in the test region and the number of background events N_{OFF}, excess is estimated by:

$$N_\gamma = N_{ON} - \alpha N_{OFF}, \tag{5.2}$$

where α is the normalization factor. Since the solid angle, exposure time, zenith angle and acceptance may be different between the on and off source regions, the normalization factor has to take all these into account when estimating the excess. It is generally defined as:

$$\alpha = \frac{\int_{on} \epsilon_\gamma(\psi_x, \psi_y, \phi_z, t) d\psi_x d\psi_y d\phi_z dt}{\int_{off} \epsilon_\gamma(\psi_x, \psi_y, \phi_z, t) d\psi_x d\psi_y d\phi_z dt} \tag{5.3}$$

where ϵ is the detector's acceptance of γ-like events which depends on the position (ψ_x,ψ_y) of the field of view and the zenith angle ϕ_z. The significance S of a signal above background is usually calculated from the approach of [127]:

$$S = \sqrt{2}(N_{ON} ln(\frac{(1+\alpha)N_{ON}}{\alpha(N_{ON}+N_{OFF})}) + N_{OFF} ln(\frac{(1+\alpha)N_{OFF}}{N_{ON}+N_{OFF}}))^{1/2} \tag{5.4}$$

Given N_{ON}, N_{OFF} and α for each position of the sky, a two dimensional excess and significance map can be derived. Older generation Cherenkov telescopes like Whipple whose field of view is small used the On-Off mode for background estimation. In this observation mode, dedicated off runs are made in the empty field which has the same conditions as the on-source runs. The main disadvantage is that twice the observation time is required for one source, and combining two dataset introduces additional systematic errors. Modern Cherenkov telescopes with a large field of view like H.E.S.S. allow estimation of background in the same field of view as the observed target. This mode of observations is called the wobble mode in which the source is placed at an offset angle from the centre of the field of view. Different techniques which are described in the following sections are then applied to determine the background.

5.3.2 Ring Background Method

In the ring background method, the background is estimated by putting an annular ring of radius R_{ring} around the test position (Fig. 5.4 left). The typical mean radius of the ring is 0.5°, which is usually sufficiently larger than the on region to avoid contamination from the source. The area covered by the ring is about 7 times that of the on region. The larger size is to increase the statistics of the background. Since the ring covers different areas which have different zenith angles and offsets to the camera centre, the acceptance is not uniform across the whole ring. The normalization factor α (defined in Eqn. 5.3) has to be determined for each bin. This background estimation is done on the whole set of accumulated data rather than on a run-by-run basis. This method is used to generate 2D sky maps for morphology studies. However, it is not suitable for spectral studies since the non-uniform distribution of acceptance in the on and off regions introduce additional systematics.

5.3.3 Reflected Background Method

In order to extract the energy spectrum, homogeneity in the acceptance in both the on and off regions is essential. The reflected background method allows this by placing a series of circles equidistant to the camera centre as the on region (Fig. 5.4 right). In order to find enough off regions, the source has be placed at a significant offset from the camera centre. The typical value is $\sim$0.5°. Note that if there is any source in the off regions, those regions cannot be used in background estimation.

The camera acceptance is radially symmetric about the centre, both the on and off regions can be considered having the same acceptance. Because of this, the normalization factor α is just the ratio of the number of on and off regions.

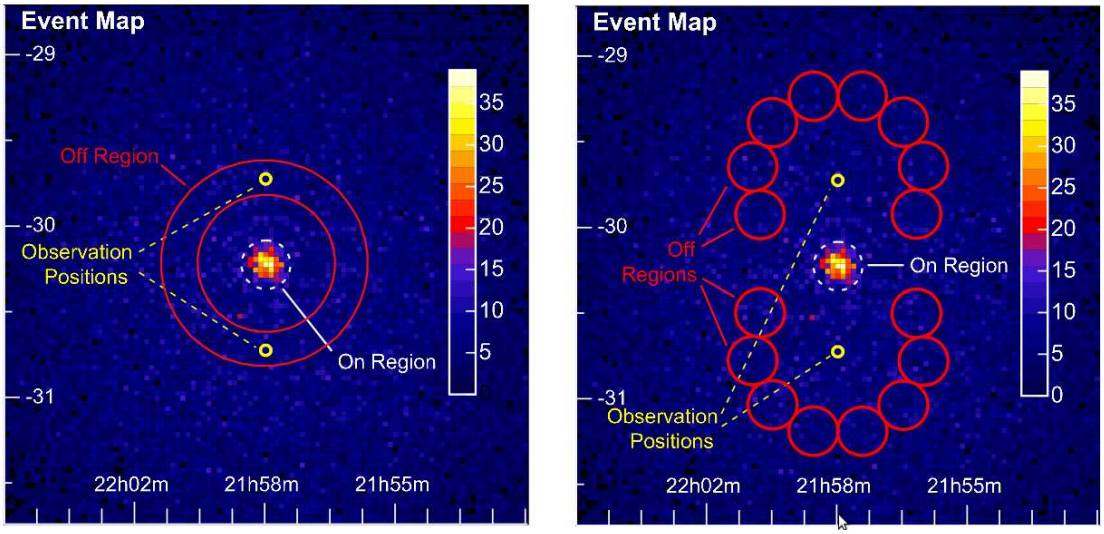

Figure 5.4: Count map of the AGN PKS 2155-304 for five hours of H.E.S.S. observation. The left plot illustrates the ring background method and the right plot shows the reflected background method. The yellow circles are the observation position in different runs. The red circles are the off regions. In the ring background method, the source is placed at the centre of the ring with a defined radius for both the inner and outer ring. For the reflected background, the off regions have the same area and are placed at an equal offset from the centre of the camera as the source. Image taken from [113].

5.3.4 Template Background Method

The template background technique adopts a different approach in background estimation. Instead of using γ-like events from off regions which spatially do not overlap with the on region, this method uses events also in the on region but classified as background events according to the MRSW [128]. Fig. 5.5 shows the MRSW distribution of both kinds of events and the corresponding selection regions. In order to calculate the normalization factor α, the radial acceptance curve for both the background and signal regime must be determined. This is done by the lookup tables. For extended sources, usually it is hard to find a "clean" off region without contamination from the source. This method is suitable for very extended sources, or crowded fields of view. However, as the background events consist of energies different from the source, it is not suitable for spectral analysis.

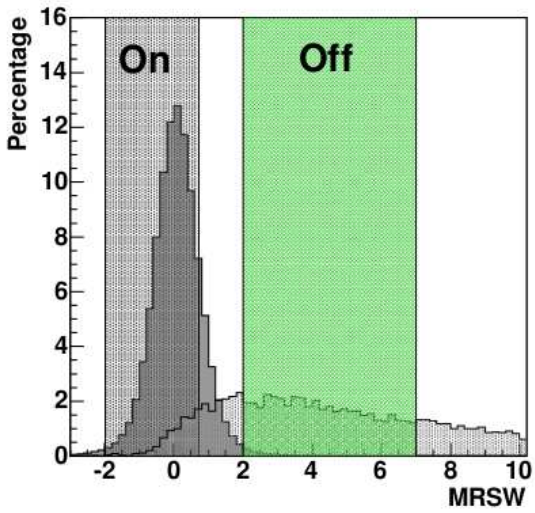

Figure 5.5: Illustration of the on and off events used for the template background method in the different MRSW regimes. Image taken from [122].

5.4 Angular Resolution

The angular resolution of H.E.S.S. is described by the point spread function (PSF), which is the squared angular distance(θ^2) between the reconstructed and true direction of simulated γ-ray events. The angular resolution is defined as the 68% containment radius R_{68}, which includes 68% of the reconstructed γ-rays. It depends on the observation conditions, particularly zenith, offset and the analysis cuts. The PSF is calculated by lookup tables produced by Monte-Carlo simulations assuming different observation conditions.

Figure 5.6 (left) shows the θ^2 distribution of simulated γ-rays for different sets of analysis cuts for a zenith angle of 10° and an offset of 0.5°. The stricter the cut, the better the angular resolution. For hard cuts, R_{68} is about 30% smaller than std cuts. Hard cut has got a larger size cut (> 200 p.e.), so only well defined camera images are selected.

R_{68} dependence on zenith and offset is shown in Fig. 5.7. For the left plot, R_{68} at zenith angles of 0°, 10°, 20°, 30°, 40°, 50°, 60° and an offset of 0.5° for std cut is illustrated. R_{68} worsens strongly beyond 30°. At larger zenith angles, since the shower maxima are further away from the telescope, the average stereo angle between camera images becomes smaller, both image length and width appear shorter. Hence, directions are more likely to be misreconstructed. For the right plot, R_{68} at offsets of 0°, 0.5°, 1.0°, 1.5°, 2.0°, 2.5° and a zenith angle of 10° for std cut is shown. As can be seen from the plot, the dependence of R_{68} on offset is not as strong as zenith. It remains rather stable up to 1.0°. At maximum simulated offset of 2.5°, it is only ∼50% larger than its minimum value. Compared with zenith dependence, R_{68} doubles between maximum and minimum zenith angles.

5.5 Energy Reconstruction and Energy Bias

Given the fact that for a certain zenith angle and offset, the shower intensity is proportional to the primary energy of the incident particles, the energy can then be reconstructed by lookup tables. These tables which parametrize energies are constructed by Monte-Carlo simulations using the image amplitude, the reconstructed impact parameter (i.e. the distance of the shower core to the telescope centre), zenith angle and offset. The reconstructed energy is sensitive to several systematic effects, e.g. atmospheric effects, optical response of the instrument and camera response.

The energy bias is defined by the relative error of reconstructed energy over true energy

$$\Delta E = (E_{reco} - E_{true})/E_{true} \tag{5.5}$$

Figure 5.8 shows the distribution of ΔE for standard cuts and for simulated γ-ray events at 20° zenith angle and 0.5° offset. The energy reconstruction is good enough for the range ∼0.3 - 100 TeV. However, bias is strong at high and low energies. The positive bias at low energies is due to selection effect. Around E_{th}, only events with upward fluctuations in image size are selected. Hence E_{reco} is over estimated, and a positive bias results. The opposite is true for high energies. Since in simulations the energies have an upper limit, this leads to an underestimation of E_{reco}, resulting in the negative bias. When performing spectral analysis, energies with large bias should be avoided. In order

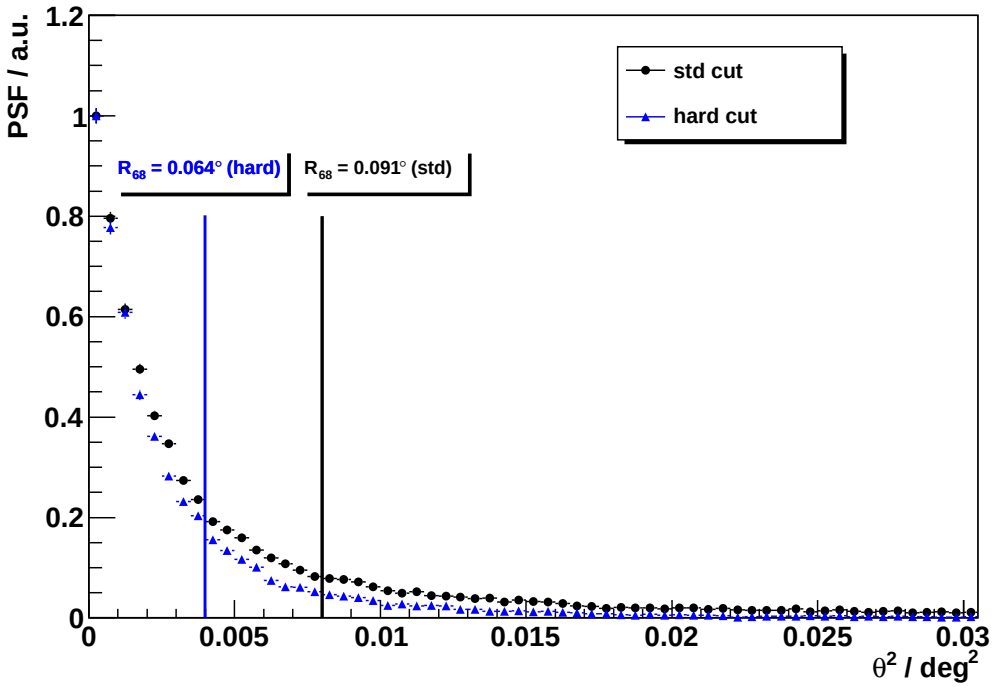

Figure 5.6: A histrogram showing the distribution of the θ^2, which is the angular distance between the reconstructed direction and simulated shower direction, for hard and std cuts. The straight lines are the 68% containment radius, which is defined as the angular resolution.

to guarantee a reliable result, safe energy threshold E_{safe} is introduced. It is defined as the range where the energy bias is less than 10%. The safe energy threshold is shown in Fig. 5.8.

5.6 Spectrum and Lightcurves

Both energy spectrum and lightcurves are of vital importance which tell the intrinsic properties of the sources. In order to determine them, the effective area which relies on the observation parameters have to be derived first. In this section, the determination of the effective area, the calculation of energy spectrum and lightcurves are described.

5.6.1 Effective Area

The effective collection area A_{eff} of the detector on the ground is significant in measuring the energy spectra of VHE γ-ray sources. A_{eff} describes the detector efficiency and is determined from Monte-Carlo simulations for events assuming a spectral index of 2. It can be expressed as:

$$A(E|\theta_z, \psi, \upsilon_{az}) = 2\pi \int_0^\infty P(E|\theta_z, \psi, \upsilon_{az}, R) R dR \tag{5.6}$$

where R is the distance of the shower core to the array centre, $P(E|\theta_z,\psi,\upsilon_{av},R)$ the probability of detecting a γ-ray shower which passes all the selection cuts given the

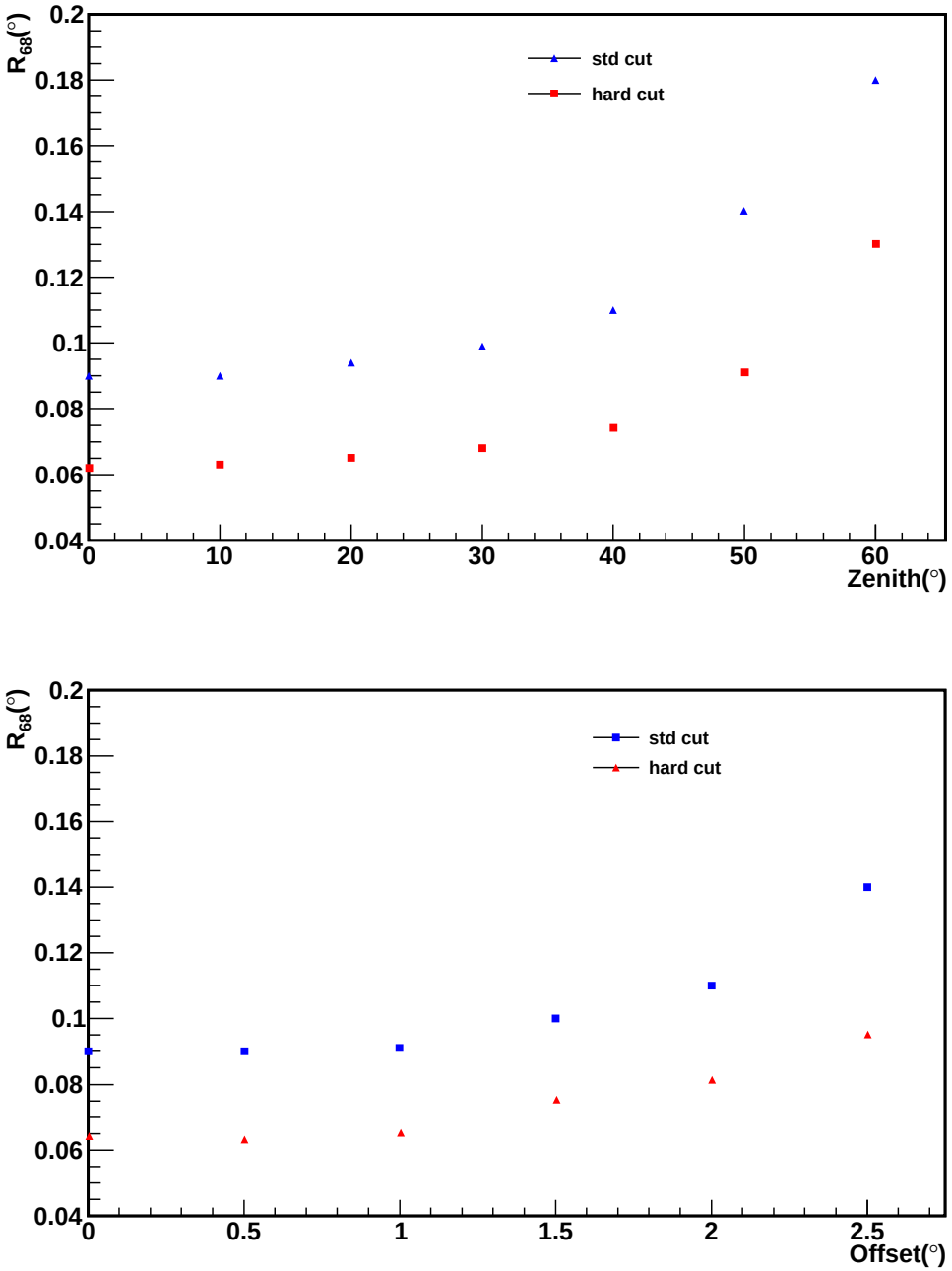

Figure 5.7: Top: Dependence of angular resolution on zenith angles for hard and std cuts assuming an offset 0.5°. Bottom: Dependence of angular resolution on offsets for hard and std cuts assuming a zenith angle 10°.

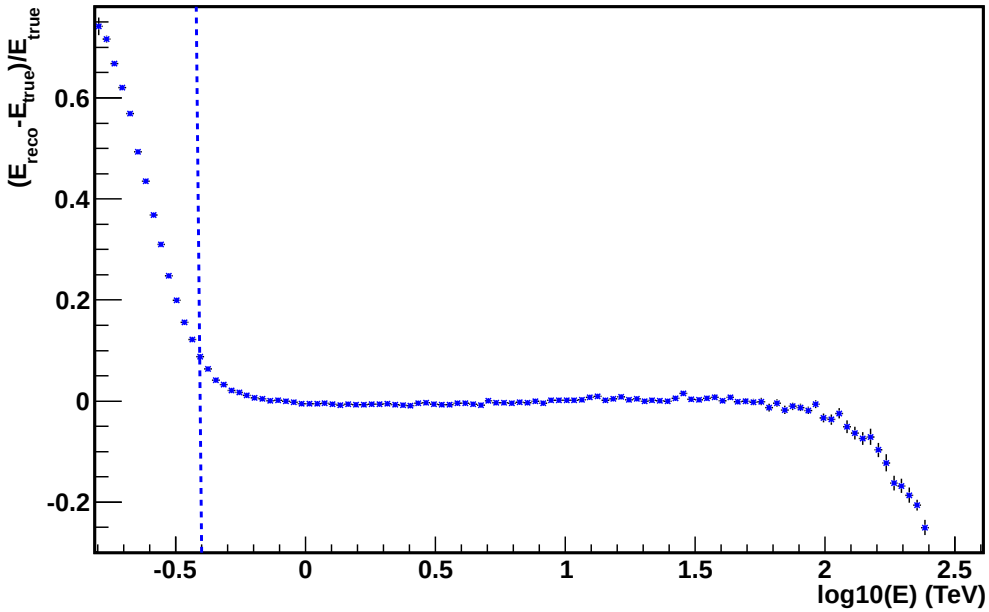

Figure 5.8: Energy bias plot assuming a zenith angle of 20° and an offset of 0.5° The dashed vertical line indicates the safe energy threshold, above which the energy bias is less than 10%.

following parameters: zenith (θ_z), offset (ψ) and azimuth (υ_{av}). It describes the optical efficiency of the telescope. At large distances where R approaches infinity, the probability becomes zero. Hence, only showers within a maximum radius are considered. Since the A_{eff} depends on the energy of the shower, zenith angle of the shower, azimuth angle of the telescope pointing, which is related to the orientation of the shower with respect to the magnetic field of the Earth's, and the offset, which is the angular distance of the shower from the observation position, it is thus determined for distinct sets of these parameters and different selection cuts. It is created for zenith angles of (0°, 20°, 30°, 40°, 45°, 50°, 55°, 60°, 63°, 65°), offsets of (0.0°,0.5°,1.0°,1.5°,2.0°,2.5°), and azimuth angles of (0°,180°). Since the dependence on azimuth angle is weak, a set of two angles is enough. For any arbitrary set of parameters (θ_z,ψ,υ_{az}), a bilinear interpolation in $\cos(\theta_z)$ and ψ is performed to obtain the effective area. As azimuth does not affect the effective area much, no interpolation is required. Given a fixed zenith angle, azimuth angle and offset, for a certain energy band ΔE, the probability P is simply the ratio of the number of γ-rays n passing the cuts to the total number of simulated events N.

$$A_{eff}(E|\theta_z,\psi,\upsilon_{az}) = \frac{n(\Delta E|\theta_z,\psi,\upsilon_{az})}{N(\Delta E|\theta_z,\psi,\upsilon_{az})} A_{MC} \tag{5.7}$$

Figure 5.9 shows the effective area as a function of the true and reconstructed energy for a zenith angle of 20°, an offset of 0.5°, and an azimuth angle of 0°. The difference in the effective area between the true and reconstructed energy is due to the limited precision in energy reconstruction. The effect of energy bias is dominant in both low and high energies. At low energies, very few events can pass the event selection cut. Once the energy threshold is passed, the effective area increases rapidly. This is seen as the sharp rise at the beginning. Then the effective area rises slowly and reaches a

maximum value at ~ 8 TeV. At larger energies, the cut becomes less efficient. Thus, there is a gradual drop in the effective area towards the end.

The dependency of effective area on zenith angles and offsets is shown in Fig 5.10. In the top plot, since larger zenith angles result in larger distances between the shower maximum and the telescopes, the optical column depth the Cherenkov light has to traverse before reaching the ground increases. Hence, the effective area increases. On the other hand, the Cherenkov light pool becomes dimmer because of the longer distance travelled, the energy threshold of the instrument becomes higher and the maximum area is reached at a higher energy. The bottom plot illustrates the change in effective areas for offsets from 0° to 2.5° in steps of 0.5°. The sharp rise at low energies is again due to energy bias.

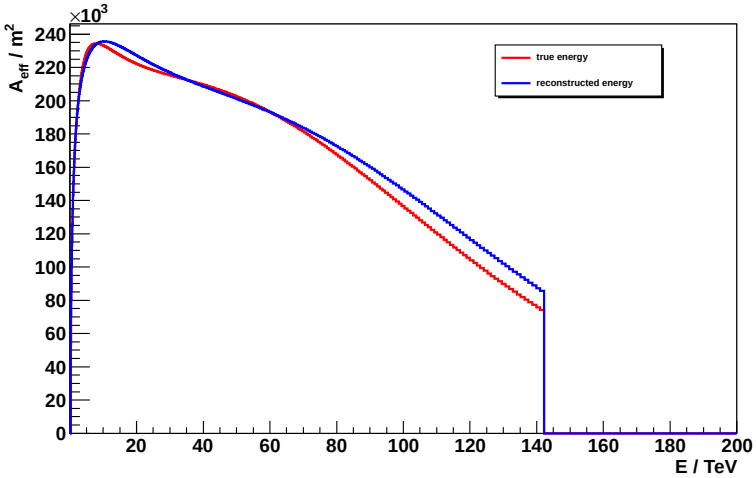

Figure 5.9: Effective areas for true(red) and reconstructed(blue) energy for 20° zenith, 0° azimuth, 0.5° offset and standard cut.

5.6.2 Spectral Reconstruction

The differential energy spectrum is an essential tool in understanding the underlying physical mechanisms of γ-ray sources. To extract the spectrum from data, the response of the detector has to be known very well. It mainly relies on zenith angles and offsets. The energy threshold and effective area also change with time. These call for accurate statistical techniques for proper extraction of the intrinsic energy disbution of the sources.

Conventionally, the differential energy spectrum, Φ(E), is defined by the following formula:

$$\Phi(E) = \frac{dN_\gamma}{dEdtdA} \tag{5.8}$$

where N_γ is the observed number of γ rays, dt per unit time, dA per unit area and dE per unit energy.

For H.E.S.S., the differential γ-ray rate after background subtraction and event selection in bins of reconstructed energy E_r is measured as:

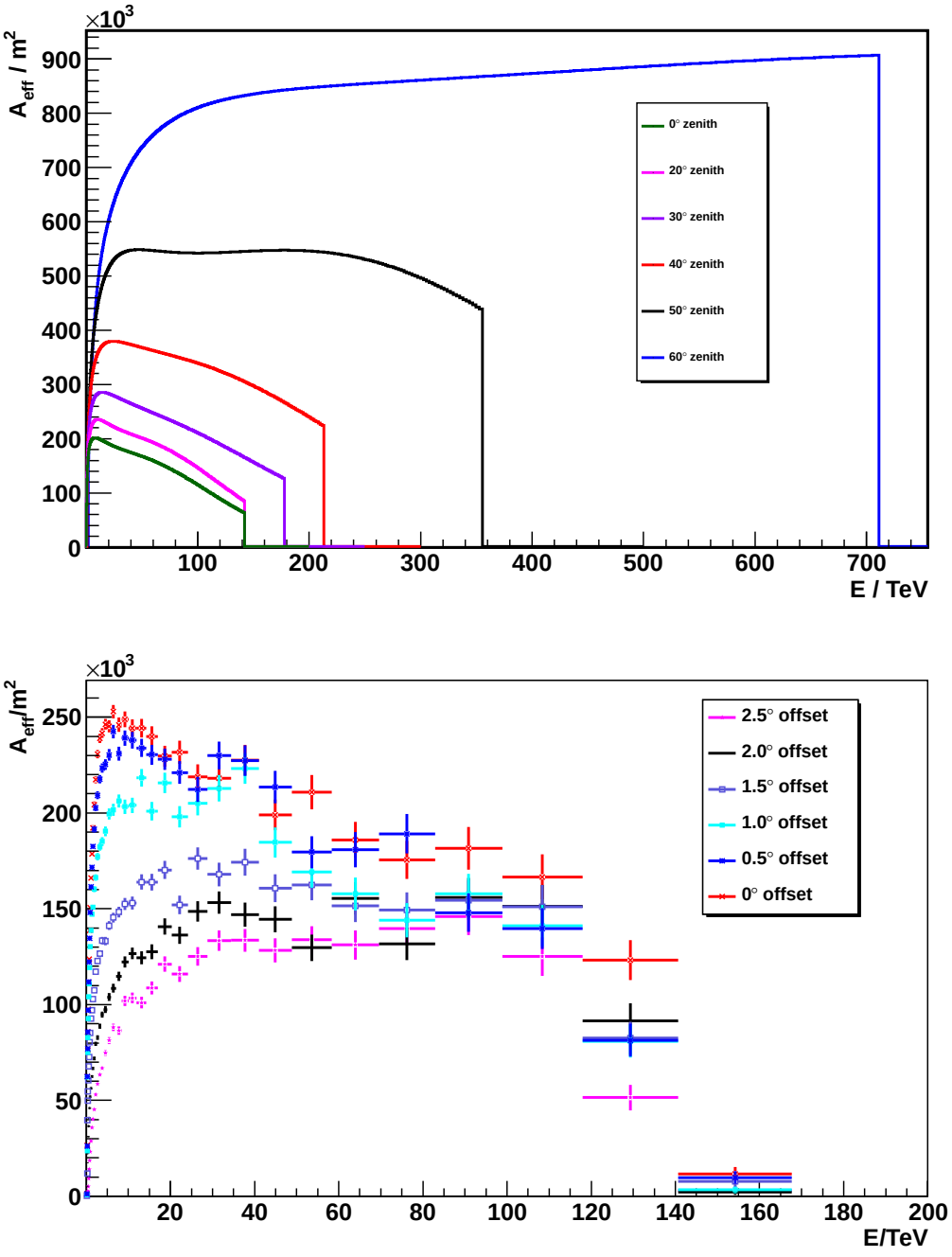

Figure 5.10: Effective areas as a function of energy for different zenith angles and offsets.

$$\frac{dN_\gamma}{dE_r dt} = \int_0^\infty R(E_r, E|\theta_z, \psi, \upsilon_{av}) \times A(E|\theta_z, \psi, \upsilon_{av}) \times \Phi(E|\vec{\alpha}) dE, \tag{5.9}$$

where R(E_r,E|θ_z,ψ,υ_{av}) is the resolution function, which is the probability density function(pdf) of a γ-ray with energy E to be reconstructed to have an energy E_r, and is obtained from simulations. A(E|θ_z,ψ,υ_{av}) is the effective collection area of the instrument described in the previously section. For the forward folding technique, a certain spectral shape which is a function of some parameters $\vec{\alpha}$ is assumed. Under this assumption, the expected number of on and off events in each reconstructed energy bin is derived. By applying log-likelihood $\vec{\alpha}$ is derived. This technique is described in the following.

For any given bin of reconstructed energy E_r, zenith angle θ_z and offset ψ, let's define:

• N_{ON} and N_{OFF} as the number of events passing the selection cuts in the ON and OFF data,

• α as the background normalization factor,

• n_γ and n_h the expected number of gamma and background events in the bin.

For a given zenith, offset and azimuth, n_γ is obtained by integrating over true energies and reconstructed energies.

$$n_\gamma = \sum_{\theta_z,\psi} t_{\theta_z,\psi} \int_{E_{r,i}}^{E_{r,i+1}} dE_r \int_0^\infty dE \times \Phi(E) A(E|\theta_z, \psi, \upsilon_{az}) R(E_r, E|\theta_z, \psi, \upsilon_{az}) \tag{5.10}$$

where $E_{r,i}$ and $E_{r,i+1}$ is the corresponding reconstructed energy bin, $t_{\theta_z,\psi}$ the livetime of the observation spent at this zenith angle θ_z and offset ψ, Φ(E) is the underlying source spectrum with preassumed parameters, A(E|θ_z,ψ,υ_{az}) and R(E_r,E|θ_z,ψ,υ_{az}) have been introduced previously.

When we expect the number of γ-ray and background events to be n_γ and n_h respectively, the probability of observing N_{ON} and N_{OFF} is given according to Poisson statistics by:

$$P(N_{ON}, N_{OFF}|n_\gamma, n_h) = \frac{n_\gamma + \beta n_h^{N_{ON}}}{N_{ON}!} e^{-(n_\gamma+\beta n_h)} \times \frac{n_h^{N_{OFF}}}{N_{OFF}!} e^{-n_h} \tag{5.11}$$

n_h is unknown. Since n_γ and n_h have Poissonian probability distributions P(n_γ) and P(n_h), n_h can be obtained by maximizing the likelihood function:

$$L(\{\vec{\alpha}\}, \{n_h\}) = \prod P(N_{ON}) P(N_{OFF}) \tag{5.12}$$

The analytical solution is given by:

$$C = \beta(N_{ON} + N_{OFF}) - (1+\beta) n_\gamma \tag{5.13}$$

$$D = C^2 + 4\beta(\beta+1) \times N_{OFF} \times n_\gamma \tag{5.14}$$

$$n_h = \frac{C + \sqrt{D}}{2\beta(\beta+1)} \tag{5.15}$$

The log-likelihood described above is then maximized for different parameters $\vec{\alpha}$ for the

assumed spectral shape. The covariance matrix between parameters and the expected number of events in each bin are then derived. The flux error is calculated from the error matrix $W_{i,j}$(inverse of covariance matrix) and the spectral parameters.

$$\Delta\Phi(E) = \sqrt{\sum_{i,j} W_{i,j} \frac{\partial\phi}{\partial\alpha_i} \frac{\partial\phi}{\partial\alpha_j}} \tag{5.16}$$

where $\Delta\Phi$(E) is the flux error at energy E.

5.6.3 Lightcurve

For investigation of source activity, lightcurves are the primary tool. In order to produce a lightcurve, the integrated flux above the threshold energy is calculated for different periods of time (e.g. runwise, nightwise, periodwise and yearwise) under the assumption that the source spectrum is well approximated by a power-law with a photon index Γ. The normalization of this power law can be estimated by comparing the total observed excess to the excess expected for a power law with a normalization of one between the energies E_1 and E_2 , known as the "expected counts" Δ. Using the same notaion as above, Δ is given by:

$$\Delta = \int_{E_1}^{E_2} \int_{t_1}^{t_2} E^{-\Gamma} A(E|\theta_z, \psi, \upsilon_{av}) dE dt \tag{5.17}$$

The normalization of the power-law energy spectrum of the source is then given by

$$\Phi = \frac{N_{ON} - \alpha N_{OFF}}{\Delta} \tag{5.18}$$

then the integral flux between the energy range E_1 and E_2 is given by:

$$F_{E_1-E_2} = \int_{E_1}^{E_2} \Phi_0 E^{-\Gamma} dE = \Phi_0 \frac{E_1^{-\Gamma+1} - E_2^{-\Gamma+1}}{\Gamma - 1} \tag{5.19}$$

The statistical error is the 1σ confidence interval for the rate of a Poisson process. The limit calculations make use of the profile likelihood method [129].

Chapter 6

Transient Tests

Strong flares are clearly seen in the lightcurves. However, fluxes of lightcurves are affected by background fluctuations. Sometimes, weaker variations in flux (or counts) may be drowned in the background without producing a significant excess given the amount of data. This calls for a set of statistical tests based on other methods in order to check for transient events. In this section, transient tests which are based on photon arrival times (intervals) are described taking into account the detector response. The tests include 1) exp-test, 2) cumulative sum test and 3) on-off test. Instead of the significance value given by [127], these tests have their own significance value [130].

6.1 Preliminary Data Processing

Since these tests rely on the photon arrival times which are acceptance dependent and observations are not made continuously, but in segments of 28 minutes (a run) seperated by gaps depending on the observing schedule, the variations in acceptance over the observed runs and effect of gaps in general, need to be accounted for. The detector's acceptance mainly depends on the zenith and offset angles. If the acceptance is high, the intervals between photon arrival times will become shorter and vice versa. Therefore, the absolute arrival times have to be processed before carrying out the tests.

In order to connect the runs together, the first event of a run is identified as the last event of the previous run (see Fig. 6.1). After connection, the absolute photon arrival times become relative. As the tests only rely on the time intervals between different events, the absolute time is not important and the relative time can be used instead. Run connection is important for tests like the On-Off test described later in this section, in which the whole dataset is divided into different time bins.

The acceptance is the integral of the effective area A(E|θ_z,ψ,ϵ,υ_{av})(see Section 5.3 for details), livetime $t_{livetime}$ and the flux Φ assuming a power law distribution and a specific spectral index Γ. This is called "expected counts".

$$a(t) = \int_{E_1}^{E_2} A(E|\theta_z, \psi, \epsilon, \upsilon_{az}) \times t_{livetime} \times \Phi^{-\Gamma} dE \tag{6.1}$$

where E_1 and E_2 are the boundaries of the energy bin.

The photon arrival times are supposed to be governed by Poisson process for a stable source or background events. Because of the differences in the detector's acceptance in different times, acceptance correction has to be applied in order to get the real times. This following formula is applied to get the acceptanced-corrected times,

$$dt = a(t) dt_{ob} \tag{6.2}$$

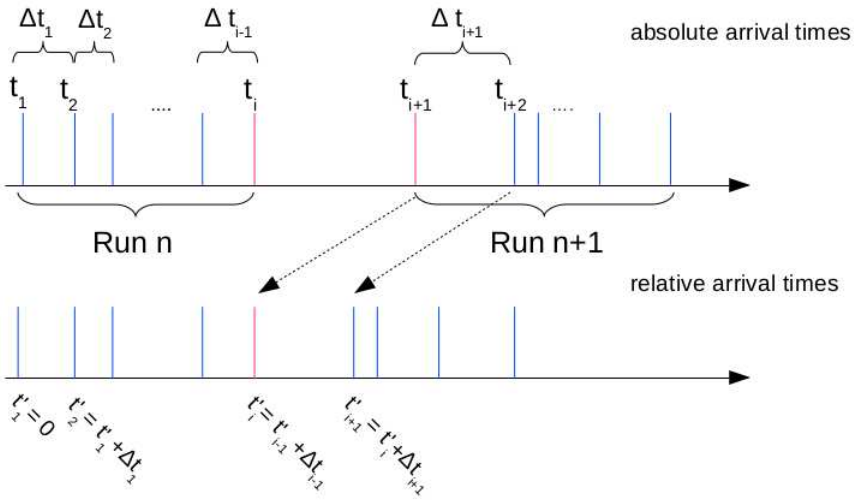

Figure 6.1: An illustration showing how different runs are connected. After connection, the photon arrival times become relative.

where dt is the corrected time intervals, a(t) is the acceptance and dt_{ob} is the observed time interval. The acceptance defined here is the expected flux per cm^2 per second, which depends on the effective area of the detector and the spectrum of the source.

The corrected time intervals then become:

$$\Delta t_i = t_{i+1} - t_i = \frac{a(t_i) + a(t_{i+1})}{2} \Delta t_{ob_i} \tag{6.3}$$

where $\Delta t_{ob_i} = t_{ob_{i+1}} - t_{ob_i}$

The $\{\Delta t\}$ can be normalized so that the mean value is 1. Suppose the total number of events is N, then $\int a(t) dt_{ob} = \int dt = \beta N$. For discrete times, $\sum \Delta t = \beta N$. The normalization factor β is thus calculated by comparing the sum of the corrected time intervals and the number of events. The corrected time intervals are then: $\Delta t_{norm} = 1/\beta \times \Delta t$. For a stable source, the acceptance corrected event arrival times follow Poisson statistics, and after normalization, the expected corrected time intervals distribution is an exponential with a slope of -1. Once the acceptance correction has been applied, different tests can be carried out.

6.2 Exp Test

This section describes the exp-test found in [131].

Now the event arrival times have been corrected for acceptance, the number of events n in a particular time window follows Poisson statistics:

$$P^{\lambda}(n) = e^{-\lambda} \cdot \frac{\lambda^n}{n!} \tag{6.4}$$

where λ is the expected value that depends on the observation time. This expression gives the probability of observing n events for an expected value λ. Generally speaking,

for the arrival times $\{t_i\}$, for events which follow Poisson distribution, there exists a constant C, such that for any time interval Δt, the observation time can be divided into equal intervals of this Δt with the number of events per interval which follows Poisson distribution of Eqn 6.4 with $\lambda = \delta/C$. The probability density function of the time intervals Δt between two events is then a decreasing exponential:

$$f_C(\Delta t) = \frac{1}{C} \cdot exp(\frac{-\Delta t}{C}) \tag{6.5}$$

For the time series $\{T_i\}_{i=1...N+1}$, the time interval between two adjacent events is:

$$\{\Delta T_i\}_{i=1...N+1} := \{(T_{i+1} - T_i)\}_{i=1...N} \tag{6.6}$$

The mean value of the series is $\bar{\Delta T}$=: C*. If we subsitute C = C* in Eqn 6.5, the ΔT follow the distribution $f_{C^*}(\Delta t)$. An estimator by [131] can test whether the observed ΔT follow the distribution $f_{C^*}(\Delta t)$. This test is particularly sensitive to ΔT which is away from the average value, i.e. bursts. The estimator M derived in [131] is as follows:

First, the pdf F(Δt) of the random probe time interval ΔT_i is defined as:

$$F(\Delta t) := \frac{1}{N} \sum_{i=1}^{N} \delta(\Delta t - \Delta T_i) \tag{6.7}$$

then,

$$\int_0^\infty f_{C^*}(\Delta t) d\Delta t = \int_0^\infty F(\Delta t) d\Delta t = 1 \tag{6.8}$$

$$\int_0^\infty \Delta t \cdot f_{C^*}(\Delta t) d\Delta t = \int_0^\infty \Delta t \cdot F(\Delta t) d\Delta t = C^* \tag{6.9}$$

from Eqn 6.8 and 6.7 follows

$$\int_0^\infty (1 - \frac{\Delta t}{C^*}) \cdot f_{C^*}(\Delta t) d\Delta t = \int_0^\infty (1 - \frac{\Delta t}{C^*}) \cdot F(\Delta t) d\Delta t = C^* \tag{6.10}$$

If we define

$$H(x) := \int_0^x h(\Delta t) \cdot f_{C^*}(\Delta t) d\Delta t \tag{6.11}$$

where h(Δt) = 1 - $\frac{\Delta t}{C^*}$. Obviously, one can get
- H(0) = H(∞) = 0

- H(C*) = 1/e for the global maximum of H Now if f_{C^*} is replaced by F(Δt) in Eqn 6.11 , the first property still holds true, but the global maximum found at C* would vary around a mean value $\sim$1/e. Hence one has

$$M(F) := \int_0^{C^*} (1 - \frac{\Delta t}{C^*}) \cdot F(\Delta t) d\Delta t \tag{6.12}$$

By substituting Eqn 6.10 into Eqn 6.12, the estimator can be expressed as

$$M = \frac{1}{N} \sum_{\Delta T_i < C^*} (1 - \frac{\Delta T_i}{C^*}) \tag{6.13}$$

This estimator compares the fraction of the time intervals which are below the average value C* to the total time. This is sensitive to excesses of the ΔT_i far from the mean value, which can be used to probe flares. For a stable source and for a uniform background, ΔT_i follow Poisson statistics, the estimator $\approx$ 1/e for F=f_{C^*}. For a burst-like behaviour (excess of small ΔT_i), it is greater than the expected value. For a periodic behaviour, in which all $\Delta T_i = 0$, it is smaller than the expected value. This estimator can be normalized to correspond to a normal distribution :

$$M_r = \frac{M - (1/e - \alpha/N)}{\beta/\sqrt{N}} \tag{6.14}$$

where N is the number of events, α the deviation from the mean value of 1/e and β quantifies the variance(Prahl 1999). The values of $\alpha = 0.189 \pm 0.004$ and $\beta = 0.2427 \pm 0.0002$ are adjusted on simulations. Fig. 6.2 shows the distributions of the M estimator and normalized estimator M_r for 10,000 simulations, with 1000 events following Poisson statistics in each set. As expected, M_r has a Normal distribution with a mean $\sim$0 and width $\sim$1. The histogram of the time interval distribution for one set of the simulations is also plotted. It exhibits a decreasing exponential law with a slope of -1.

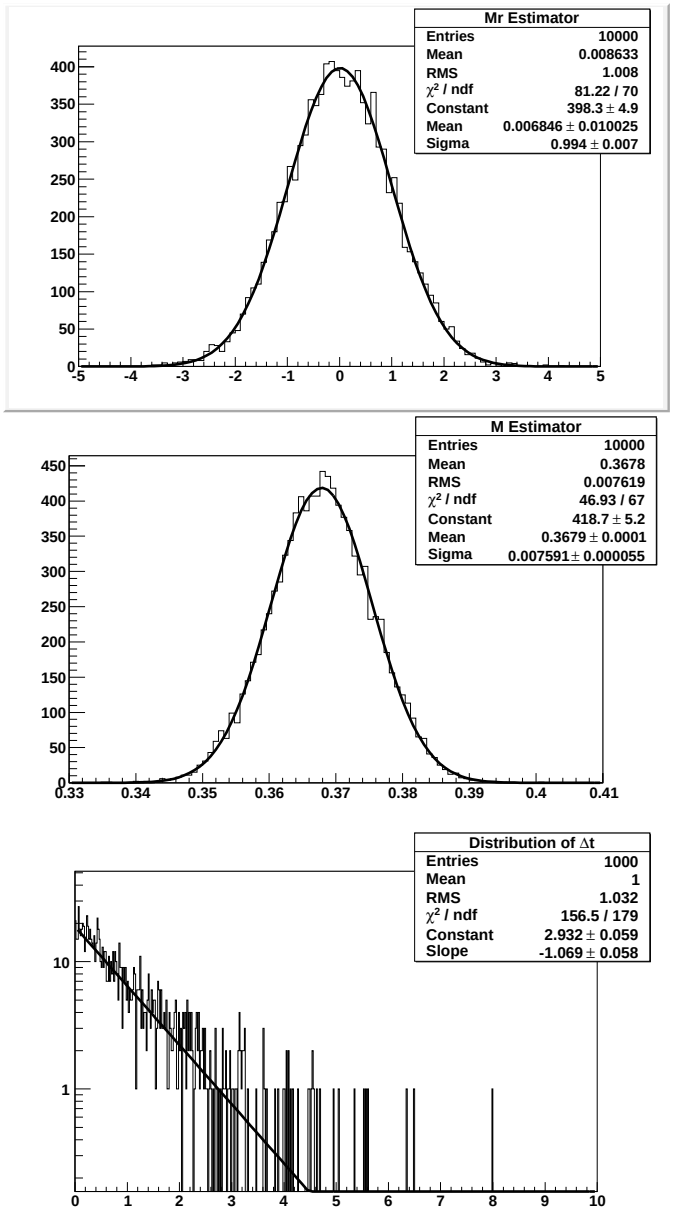

Figure 6.2: Exp-test results for 10,000 simulations of 1000 events. The top and middle figures show the distribution of the estimator and normalized estimator. The distribution of the normalized estimator is well fitted by a Gaussian distribution with zero mean and a standard deviation of 1. The bottom figure shows the distribution of the time intervals between two consecutive events for a sample of 1000 events. The fit shows an exponentially decreasing slope of -1.

6.3 Cumulative Sum Test

The cumulative sum (cusum) test presupposes that the time interval between two events follows Poissonian distribution. The individual time intervals are added up to compute the cumulative sum. At each step, the mean value is subtracted in order to get a variable with a null mean value [130] [132].

For a set of time intervals ordered in time $\{\Delta \mathrm{T}_i\}_{i=1\ldots N} := (T_{i+1}$ - $\mathrm{T}_i)_{i=1\ldots N}$, the cusum variable for time i is:

$$\chi_i = \sum_{k=1}^{i} (\Delta T_k - < \Delta T >) \tag{6.15}$$

where $<\Delta T> = \frac{1}{N}\sum_{i=1}^{N} \Delta T_i = C$. For each i, the value has a null mean:

$$\begin{aligned} < \chi_i > &= \sum_{k=1}^{i} (< \Delta T_k > - C) \\ &= 0 \end{aligned} \tag{6.16}$$

For events following Poisson behaviour, the probability density funciton of the time intervals is represented by eqn. 6.5, $<\Delta T^2>$ then becomes:

$$\begin{aligned} < \Delta T^2 > &= \int \Delta T^2 f_c(\Delta T) dt \\ &= 2C^2 \end{aligned} \tag{6.17}$$

The variance of the cusum variable χ_i is then :

$$\begin{aligned} Var(\chi_i) &= < \chi_i^2 > - < \chi_i >^2 \\ &= < \chi_i^2 > \\ &= < (\sum_{k=1}^{i} < \Delta T_k > - \frac{i}{N} \sum_{j=1}^{N} < \Delta T_j >)^2 > \\ &= \frac{2iC^2}{N}(N - i) \end{aligned} \tag{6.18}$$

Thus, for each index, we can determine whether the variable deviates from the expected distribution and quantify the number of corresponding standard deviations. To view this, we draw a plot of the cumulative sum vs. time intervals, and overplots the contours for 3, 4, 5, and 6 standard deviations (Fig 6.3). If the cusum value exceeds a certain significant threshold, then one can tell to what extent it deviates from Poisson distribution. Besides, the position of the maximum/minimum of the cusum value corresponds to the time that a flare begins/ends. In Fig. 6.3, the cusum test is performed on 1000 simulated events which follow Poisson statistcs. The cusum value fluctuates, showing no trend. The plot on the right is the significance, which is the cusum value on the left divided by 1 standard deviation.

In Fig. 6.4, the evolution of the cusum value according to the time intervals (calculated from acceptance-corrected time) for the flaring source Mrk 421, the corresponding run-wise lightcurves and the time interval distribution are shown. During a flare, the time interval is shorter than average, so the cusum value gets smaller and smaller. In left of top Fig. 6.4 , one strong downward trend starting from time $\sim$700 and ending at time $\sim$ 1370 is noted. This corresponds to the big flare in the lightcurves at $\sim$ MJD 53100. The smaller flare at $\sim$ MJD 55750 corresponds to the dip in the cusum plot from time

~1450 to the end. Since the cusum test extracts individual event times and no binning is required, it can better tell the duration of a flare compared to the lightcurves. In the bottom plot of Fig. 6.4, where the normalized time interval distribution is shown, the slope of the fit is -1.4, indicating significant deviation from Poisson distribution. This is another manifestation of a flare.

This method seems promising but has the drawback that the signal is more sensitive to a smaller number of events. A short timescale flare would fall unnoticed in long timescale data. Therefore, it requires some changes to be optimal. A large dataset can be divided into smaller time window of a fixed size, and then the test is run over the whole dataset. Using the C* value of the whole dataset, the significance is derived for each time interval. The result of the test is the maximum of all the significances.

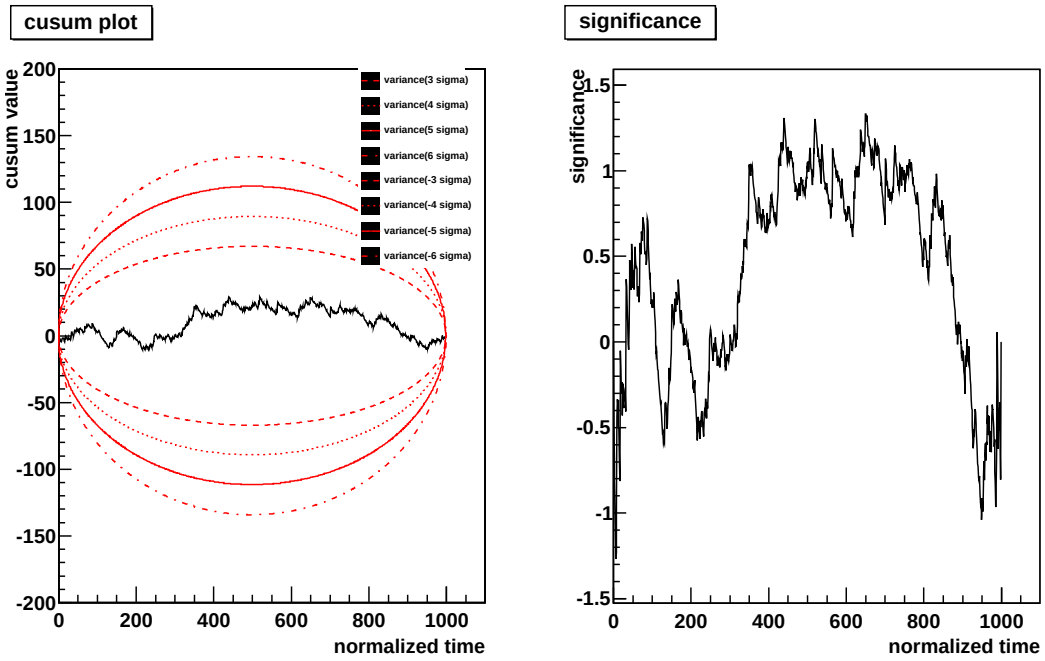

Figure 6.3: Left: Simulation of 1000 events for the cusum test.The red lines are contours for 3,4,5 and 6 standard deviations. No clear trend is observed. Right: Significance found for the cusum plot.

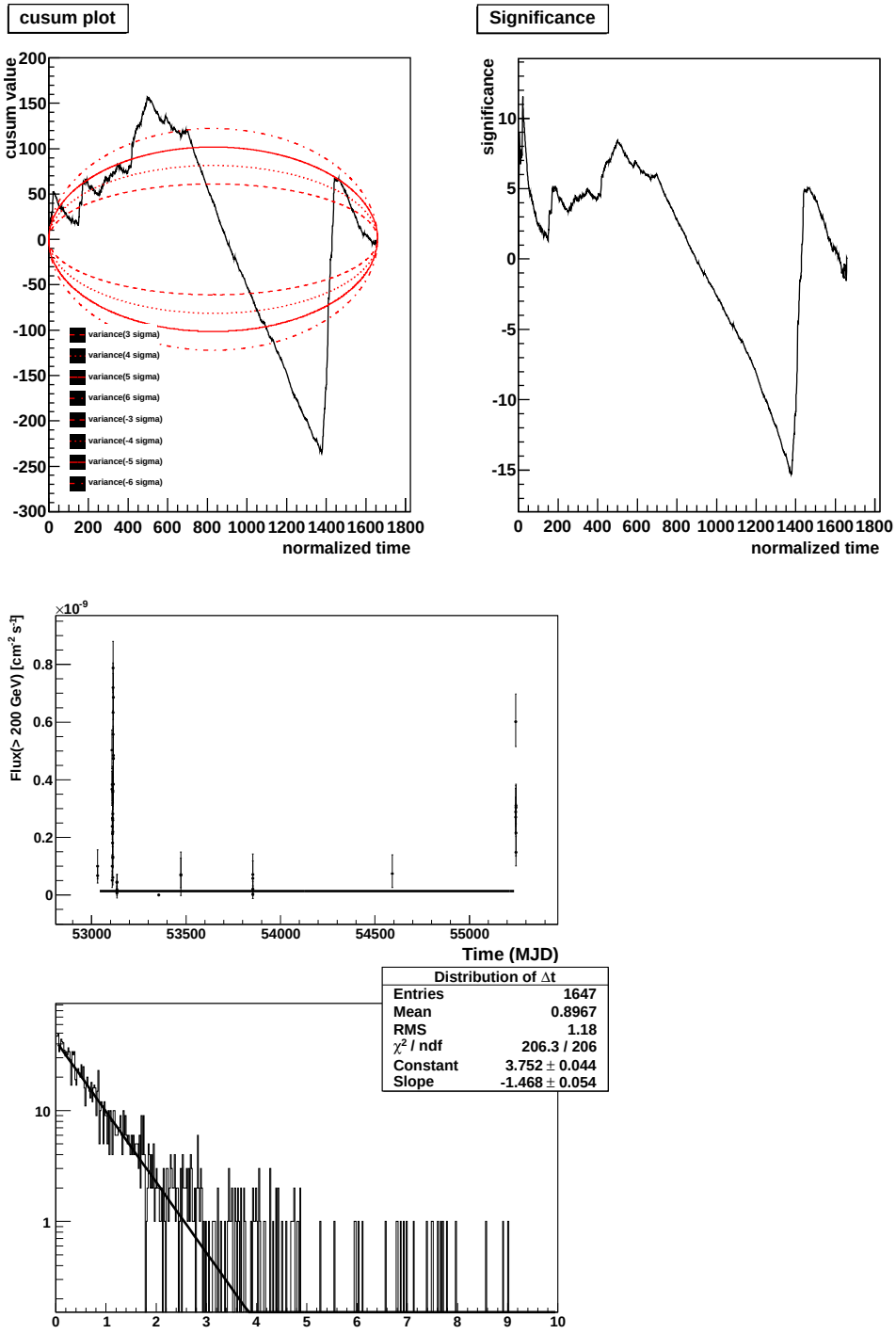

Figure 6.4: Cusum test results for Mrk 421. The top figure shows the cusum and significance value. The middle is the lightcurves for the same set of data. The big dip around the middle and smaller dip at the end in the cusum plot correspond to the two flares in the light curves respectively. The time interval distribution at the bottom shows prominent deviation from Poisson statistics.

6.4 On-Off Test

In this test, a set of time intervals $\{\Delta T_i\}$ amounting to a total observation time t is divided into evenly-spaced time bins. The binsize is picked based on the variability timescale being probed. Each turn, a particular bin is set as "on" and the rest as "off" to compute significance [133]. It is the same as the ON/OFF method used to compute maps but in one dimension. This test allows to probe a given timescale. The idea of bin division is shown in Fig 6.5.

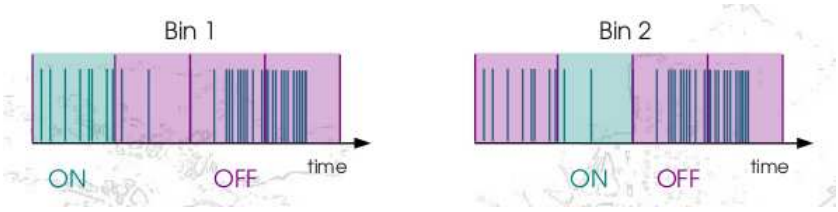

Figure 6.5: An illustration of the classification of on/off bin for the On-Off test.

For each on bin, the number of events is counted as N_{ON}. The same is done for the off bins, N_{OFF} is counted. α is calculated as the ratio of integrated acceptance, i.e. τ_{on}/τ_{off}. Then excess is calculated using the standard formula excess = N_{ON}-α N_{OFF}, and significance is derived from the Li & Ma significance [127]. If a bin has significance larger than 5σ, this bin is considered significant. The whole process is repeated with this bin removed. It stops when no more significant bin is found.

This method applies to short timescale flares that happen within a run. For consecutive runs where the gap is sufficiently smaller than the time bin, different timescales of a flare can still be probed. This test has an advantage over the exptest and cumulative sum test in a way that a significant bin of short timescale can stand out from the rest of the bins however large the time series is. But please note that sometimes a bin may include more than one run. Care has to be taken when a significant bin is found. Once a significant bin is detected, data of that period can be extracted and processed with other tests. The on-off test can be used as the first test to check for variability.

Fig 6.6 and 6.7 show the results of simulations and Mrk 421 respectively. A time bin of 10 minutes are set for both. In the simulation, there is no flare, no bin is found significant. For Mrk 421, four bins are found significant (bottom left). These bins indicate a flare of a timescale of $\sim$ 10 minutes.

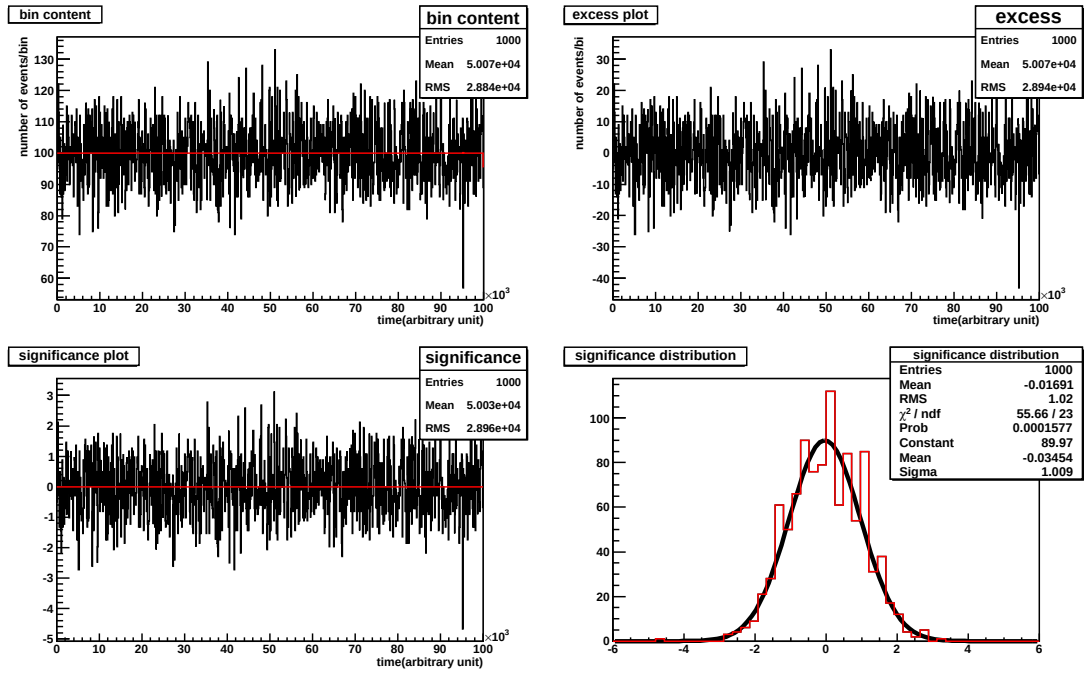

Figure 6.6: Results of simulations for the on-off test. 100000 events are simulated. A time bin of 10 minutes is set.Top left: The black line is the number of events in the on bin while the red line is the number of events in the off bin. Top right: Excess plot, which is N_{ON} - α N_{OFF}; Bottom left:Significance of each bin. The red line indicates those bins found significant. In this case, there is none. Bottom right: Significance distribution of each bin, which follows Gaussian distribution.

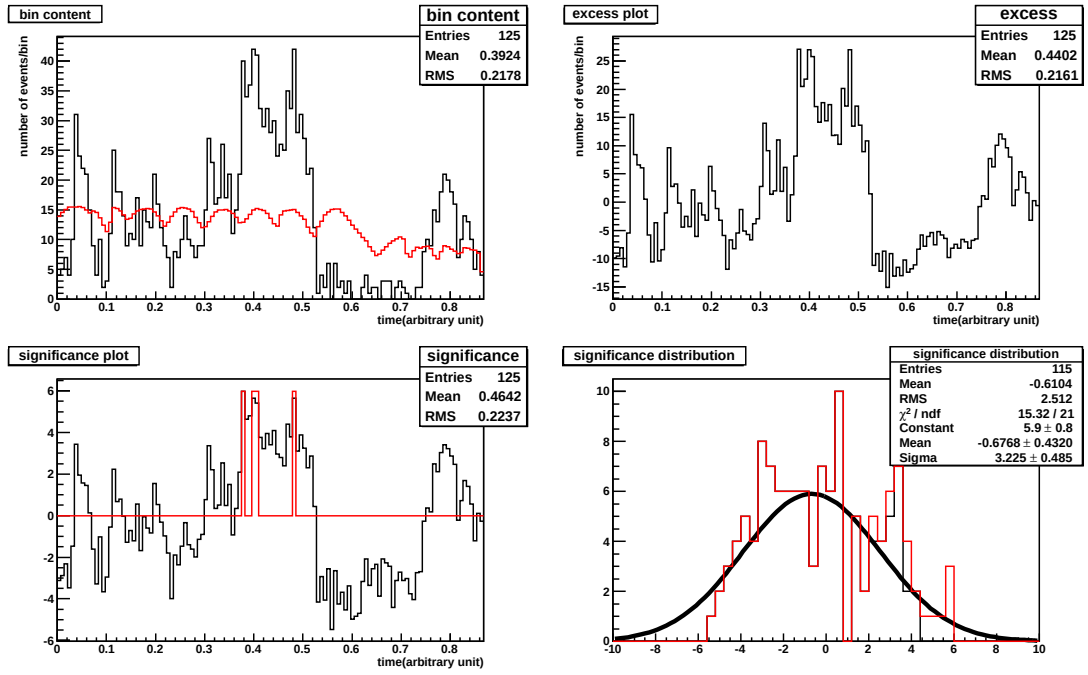

Figure 6.7: Results of the on-off test applied to Mrk 421. A time bin of 10 minutes is set.Top left: The black line is the number of events in the on bin while the red line is the number of events in the off bin. Top right: Excess plot, which is N_{ON} - α N_{OFF}; Bottom left:Significance of each bin. The red line indicates those bins found significant. 4 bins are found significant, indicating a flare of a time interval of 10 minutes. Bottom right: Significance distribution of each bin, which follows Gaussian distribution.

Chapter 7

HESS Observations of Sgr A*

In this section the analysis of Sgr A* using H.E.S.S. data is described. The analysis has two different datasets. The first set consists of observations from the HESS phase I, using only CT1-4 telescopes. Hereafter this is called dataset I. The second set includes observations using CT1-4 and the fifth telescope, CT5 . This is called dataset II throughout this analysis.

7.1 Dataset

The observations of dataset I were performed from 2004 to 2012. As the VHE source with most exposure in HESS observation campaigns, time is allocated to Sgr A* every year. This set of analysis includes runs with dedicated observations to the central source and observations of sources within a distance of 2.5° to Sgr A*. Altogether 720 runs were taken, 559 of which passed the data quality cut and only 545 can pass the atmospheric quality cut for spectral analysis [134]. The total livetime after these cuts amounts to 234 hours.

If observations are made at high zenith angles ($40° < \theta_z < 70°$), the Cherenkov light has to travel a longer distance to reach the ground. As a result, the radius on the ground is increased. In this case, there is a higher probability to observe energetic showers which can put constraints on the high energy part(> 10 TeV) of the spectrum. This was first done in 2005 and 2006. In Aharonian et al 2009, using the data from 2004-2006, it was found that the spectrum has an exponential cutoff at $\sim$15 TeV. Following this discovery, in 2011, observations at high zenith angles were made again. For dataset I, the overall mean zenith and offset are 20.9° and 0.9° respectively. Only data with at least 3 telescopes triggered are considered. In this way, the angular resolution is improved. The safe energy threshold for the whole dataset I is $\sim$196 GeV. The upper limit of the energy range is 62 TeV.

For spectrum and lightcurve study, due to many VHE sources around Sgr A*, a large exclusion region is applied. As a result, no off region can be found sometimes. A total of 341 runs can be used. No suitable data is available for the year 2009 due to this reason.

For dataset II, runs were taken between 2013 and 2014, the time around pericentre passage of G2. A total of 125 runs are used for map generation, resulting in a livetime of 47.3 hours. The mean offset and zenith angle are 22.6° and 0.5° respectively. The safe energy threshold (see Section 5.5) of this dataset is 237 GeV. The upper end of the energy range 22 TeV. For spectrum and lightcurve reconstruction, a total of 49 runs are used.

Table 7.1 summarizes the observation campaigns towards Sgr A* over the years. All data were taken in the wobble mode.

Table 7.1: A table of observation summary of Sgr A*

dataset I	Year	Livetime(hr)	Mean Zenith	Mean Offset	Excess	Significance
	2004	51.6	21.8	0.9	2574.6	46.0
	2005	59.6	25.4	0.8	2276.4	44.2
	2006	29.5	18.0	1.0	945.2	29.8
	2007	9.2	10.9	0.9	343.2	18.0
	2008	14.4	14.8	0.7	511.9	23.0
	2009	6.0	18.1	0.5	171.5	14.1
	2010	13.0	11.5	1.1	355.9	18.9
	2011	9.3	34.4	0.8	275.8	15.5
	2012	34.5	19.8	0.8	1165.7	33.1
	total	234.5	20.9	0.9	8761.6	88.2
dataset II	2013 & 2014	47.3	22.6	0.5	1819.8	42.8

7.2 Data Analysis

Dataset I is analyzed with standard multivariate analysis described in Section 5.2. For dataset II, Hillas standard hybrid cut is used for event selection. This is a combined analysis which uses events where there are at least two shower images available. The Ring background method is used to produce the sky maps while the Reflected background method (for details, see Section 5.3.2) is used to derive the differential energy spectra and lightcurves. For the former method, due to the exclusion region, it is difficult to use a ring with a fixed size. Instead an adaptive ring background method is used. The size of the ring is changeable but the thickness is kept constant, which is 0.2° in this analysis.

Figure 7.1 and 7.2 respectively show the smoothed sky map of excess events in the region around Sgr A* and significance map of the source for dataset I and dataset II. For dataset I, a significance of 88.2 is found, with an excess of 8761.6. For dataset II, the source is found at 42.8σ significance, with over 1800 excess events. Both datasets have the source excess centroid compatible with each other.

The significance maps of the region around Sgr A* after applying the exclusion region for dataset I and II are shown in Fig. 7.3a and Fig. 7.4a respectively. The corresponding histogram of the significance distribution of the background is shown on the right. As can be seen from these plots, the significance distribution is close to a normal distribution with a mean of -0.15 and width 1.11 for dataset I, and a mean of -0.13 width of 1.18 for dataset II, meaning that the background is well estimated.

Figure 7.5 shows the γ-ray emission as a function of squared angular distance θ^2 from the position of Sgr A*. For dataset I any event within a squared angular distance of 0.0125° is taken as the "On" region while for dataset II, this distance is 0.0132°. In this figure a long tail stretches outside the on region. This tail indicates the contribution of diffuse gamma-ray emission at large distances from the source.

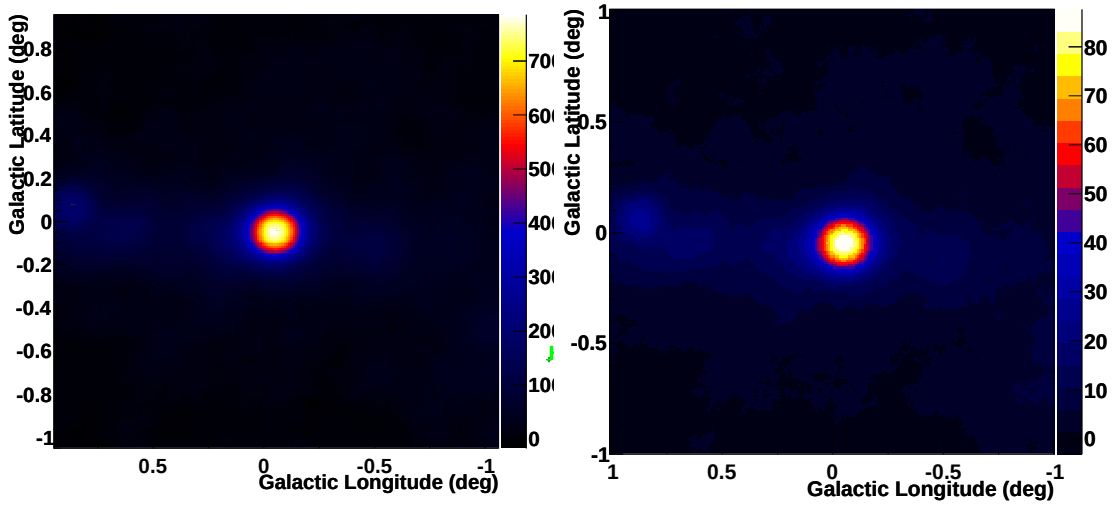

(a) Excess map **(b)** Significance map

Figure 7.1: Excess and significance maps of Sgr A* for dataset I, using Ring background method. Events are oversampled with a radius of 0.1°.

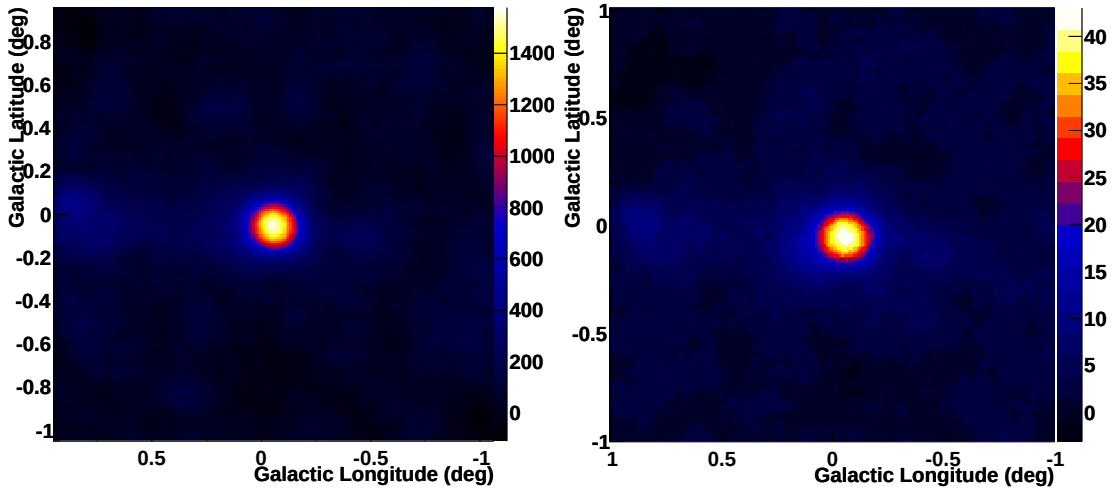

(a) Excess map **(b)** Significance map

Figure 7.2: Excess and significance maps of Sgr A* for dataset II, using Ring background method. Events are oversampled with a radius of 0.1°.

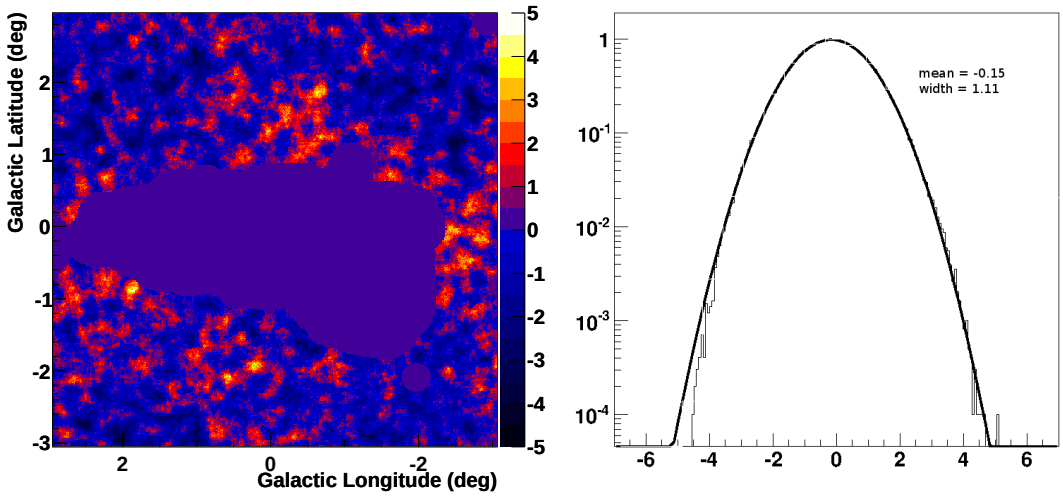

(a) (b)

Figure 7.3: Left: Significance map of the regions outside the exclusion region for dataset I. Major γ-ray sources around Sgr A* are excluded. Right: A histogram of the significance distribution outside the exclusion region for dataset I. The background is pretty well estimated with a Gaussian distribution of mean = -0.15 and width = 1.11.

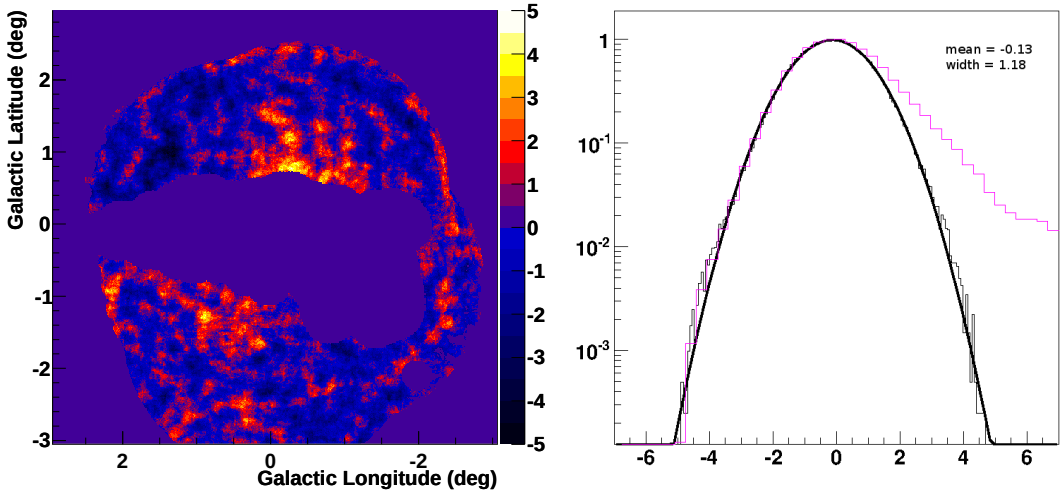

(a) (b)

Figure 7.4: Left: Significance map of the regions outside the exclusion region for dataset II. Major γ-ray sources around Sgr A* are excluded. Right: A histogram of the significance distribution outside the exclusion region for dataset II. The background is pretty well estimated with a Gaussian distribution of mean = -0.13 and width = 1.18.

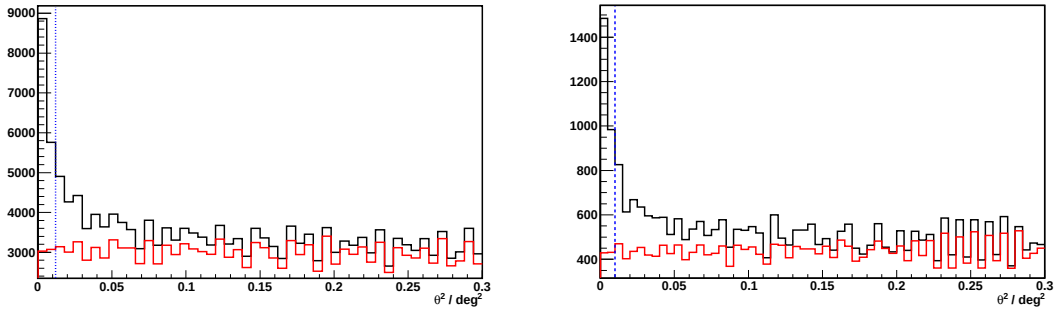

(a) Dataset I **(b)** Dataset II

Figure 7.5: Event distribution in the source region (solid black line) for dataset I (a) and dataset II (b) compared with the expected level of cosmic ray background contamination (solid red line) as a function of θ^2 from the source position where θ is the angular distance between Sgr A* and the γ-ray event. Vertical dotted blue line shows the region used to extract the signal from the source.

7.3 Energy Spectrum

The energy spectrum of the Sgr A* has been derived using the forward folding method (For details see Section 5.6.2). The systematic errors on the spectral indices derived in this analysis are taken to be 5% [135]. The errors are mainly due to broken pixels in the camera. Other sources of systematic errors include the variations of the atmospheric conditions and the absolute calibration of the response of the telescopes. These lead to systematic errors on the integrated fluxes above 1 TeV of about 20%. For the systematic bias of the reconstruction of the cut-off energy, a Monte-Carlo study shows that it increases linearly with the cut-off energy [136]:

$$E_{cut} = (0.92 \pm 0.01) \times E_{cut,true} + (0.25 \pm 0.05) \quad TeV \tag{7.1}$$

The systematic errors on the reconstruction of the cut-off energy amount to 17%.
The energy spectrum derived for dataset I and dataset II are fit with a power law,

$$\frac{dN}{dE} = \Phi_0 \times (\frac{E}{1TeV})^{-\Gamma} \tag{7.2}$$

and a power law with exponential cut-off,

$$\frac{dN}{dE} = \Phi_0 \times (\frac{E}{1TeV})^{-\Gamma} \times e^{(-\frac{E}{E_{cut}})^{\beta}} \tag{7.3}$$

where Φ_0 is the flux normalisation in $\mathrm{TeV}^{-1}\mathrm{cm}^{-2}\mathrm{s}^{-1}$, Γ the spectral index and E_{cut} the energy cut-off. In Eq. 7.3, β is the strength of the cut-off, which is taken to be one.
Fig. 7.6 shows the results of the fit for both datasets. For dataset I, as is found in [136], power law with exponential cutoff makes a better fit to the data. For dataset I, the results of χ^2/d.o.f. for power law with exponential cutoff is 37.7/21 whereas that for power law fit is 140.8/22. The index, energy cutoff and flux normalization at 1 TeV and integrated flux above 1 TeV are found to be:

$$\Gamma = 2.16 \pm 0.03_{stat} \pm 0.11_{syst} \tag{7.4}$$

$$E_{cut} = 14.16 \pm 2.66_{stat} \pm 2.41_{syst} \quad TeV \tag{7.5}$$

$$\Phi_0 = (2.94 \pm 0.08_{stat} \pm 0.59_{syst}) * 10^{-12} cm^{-2} s^{-1} \tag{7.6}$$

$$\Phi(\geq 1TeV) = (2.07 \pm 0.05_{stat} \pm 0.41_{syst}) 10^{-12} cm^{-2} s^{-1} \tag{7.7}$$

For dataset II, power law fit and power law with exponential cut-off do not make noticeable difference. The index, flux normalization and integrated flux above 1 TeV

found for power law are:

$$\Gamma = 2.20 \pm 0.05_{stat} \pm 0.11_{syst} \tag{7.8}$$

$$\Phi_0 = (2.75 \pm 1.40 \pm 0.55) * 10^{-12} cm^{-2} s^{-1} \tag{7.9}$$

$$\Phi(\geq 1TeV) = (2.23 \pm 0.14_{stat} \pm 0.45_{syst}) 10^{-12} cm^{-2} s^{-1} \tag{7.10}$$

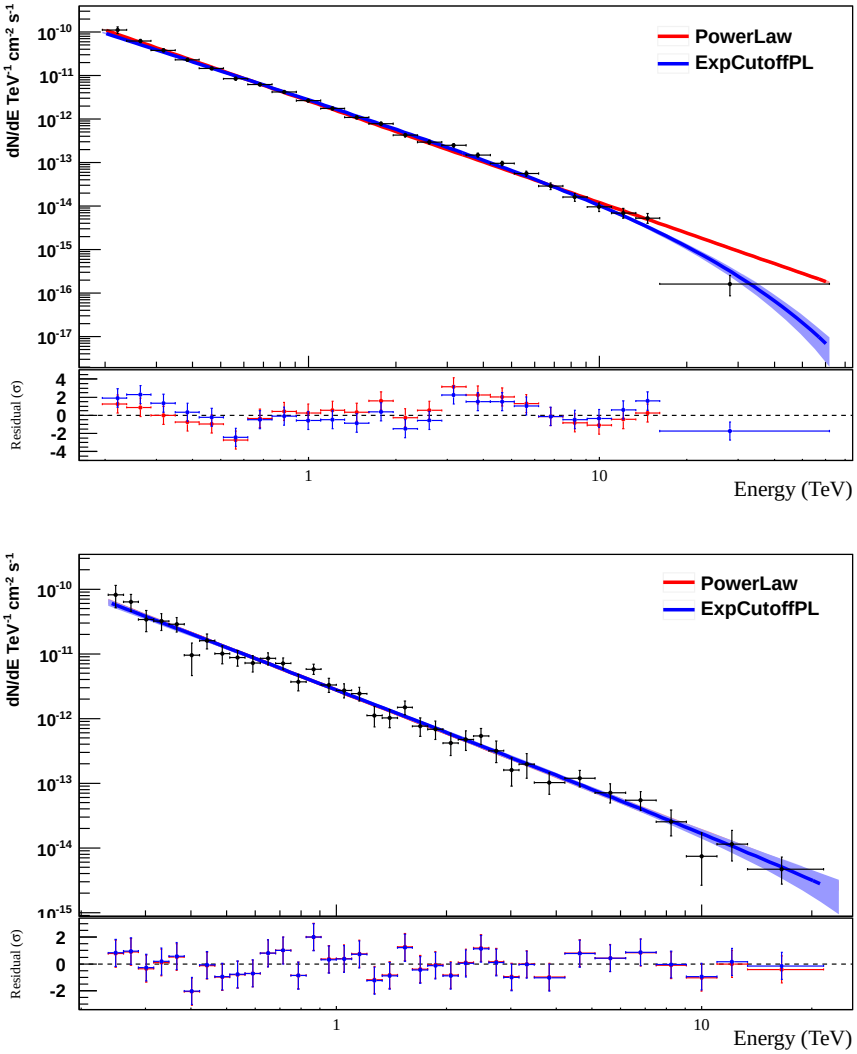

Figure 7.6: Spectral results of Sgr A* derived from standard multivariate analysis covering the years 2004-2013 for dataset I(top) and standard hybrid analysis for dataset II(bottom) for 2013-2014. The shaded areas are the 1σ confidence intervals for both power law fit and power law with exponential cut-off fit. The lower panels show the fit residuals.

The values found for both datasets are consistent with previously published H.E.S.S.

Table 7.2: Spectral parameters on the yearly spectrum for dataset I.

Year	Φ_0 (10^{-12}TeV^{-1}cm^{-2}s^{-1})	Γ	E_{cut} (TeV)	I($\geq$1 TeV) (10^{-12}cm^{-2}s^{-1})
2004	3.11 ± 0.17	2.13 ± 0.06	13.07 ± 4.17	2.18 ± 0.10
2005	2.91 ± 0.15	2.11 ± 0.07	11.51 ± 3.47	2.01 ± 0.09
2006	2.77 ± 0.22	2.19 ± 0.10	30.30 ± 30.76	2.09 ± 0.16
2007	2.16 ± 0.27	2.37 ± 0.15	0.42 ± 0.03	1.71 ± 0.22
2008	2.77 ± 0.34	2.31 ± 0.15	22.78 ± 33.83	1.85 ± 0.18
2010	2.50 ± 0.28	2.01 ± 0.16	23.75 ± 32.22	2.07 ± 0.19
2011	3.53 ± 0.52	2.10 ± 0.21	7.29 ± 4.83	2.19 ± 0.21
2012	3.11 ± 0.20	2.09 ± 0.09	12.74 ± 4.84	2.23 ± 0.13

results [136], which is (2.1 ± 0.04)*10^{-12}TeV^{-1}cm^{-2}s^{-1} for index, 15.7 ± 3.41 for energy cutoff, 2.55 ± 0.06 for flux normalization, and (1.99 ± 0.09)* 10^{-12}cm^{-2}s^{-1} for flux above 1 TeV. For datset II, no cut-off is seen in the spectrum. This is probably due to the significantly smaller time exposure compared with the larger dataset available for H.E.S.S. I analysis. There is not enough high energy statistics to tell whether an energy cut-off exists. In order to check for spectral variability, a yearly spectral analysis is carried out for dataset I. The spectral parameters found for power law with exponential cut-off are presented in Table 7.2. For the years 2006, 2007, 2008 and 2010, oberservations were made at low zenith angles ($< 18°$). As explained previously, energetic showers could not be well observed. As a result, the energy cutoff in these years are not well constrained. Power law fit and power law with exponential cutoff fit do not make significant differences in these four years. From 2004 - 2007, the spectrum showed softening with the index changing from 2.13 to 2.37, then it became hard again, having an index of 2.09 in 2012. Though a change is noted, the yearly indices are still compatible within a 2σ level.

7.4 Lightcurves

The runwise, nightwise, monthwise and yearwise integral VHE flux above the energy threshold for the dataset I is shown in Fig. 7.7. Since dataset II is smaller, only the runwise and nightwise lightcurves are shown (Fig. 7.8). In order to check for variability, a χ^2 test is performed. The results are listed in Table 7.3. The runwise lightcurves are also studied for individual years of dataset I. The mean flux and results of χ^2 test are listed in Table 7.4.

The overall runwise, nightwise and periodwise lightcurves for dataset I and the runwise and nightwise lightcurves for dataset II show hints of variability (the probability of being constant is $< 5\%$). For the individual years of the runwise lightcurves of dataset I, 2005, 2006, 2008 and 2012 may be variable. Considering the large error bars, other tests checking for variability need to be done. Transient tests are applied to these seemlingly variable lightcurves. The results are presented in the next section.

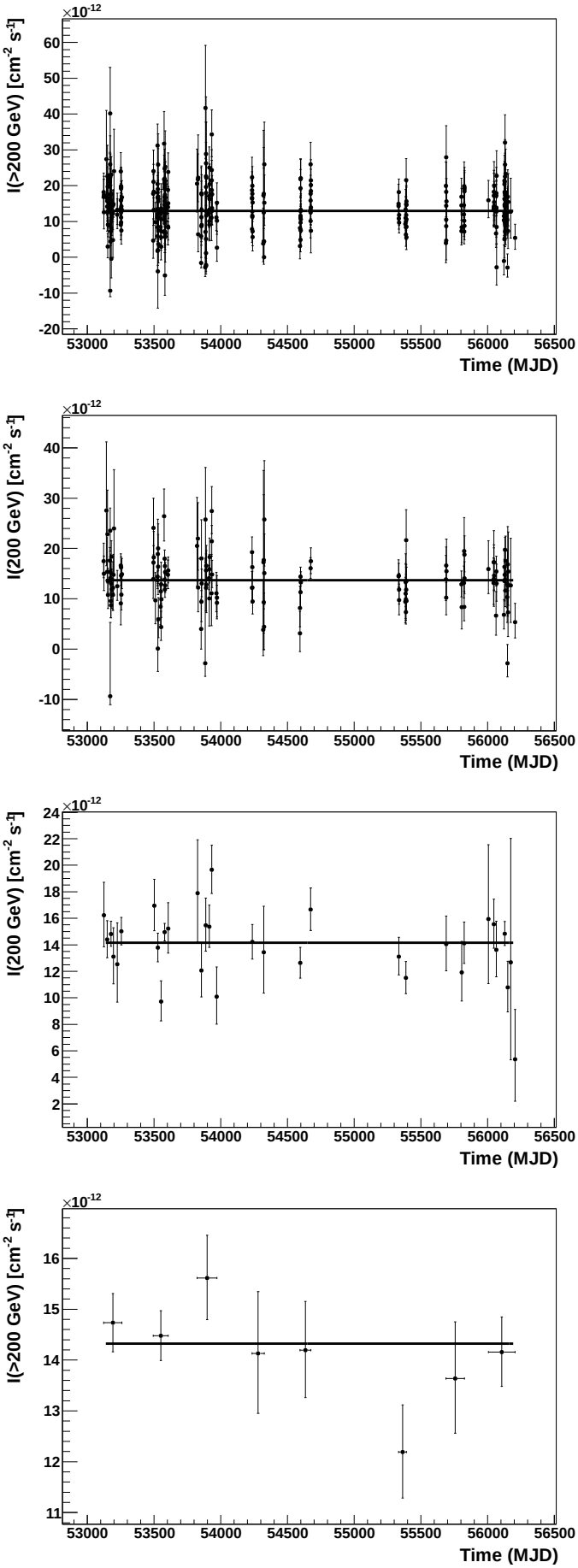

Figure 7.7: From top to bottom:Runwise, nightwise, monthwise and yearwise lightcurves for dataset I.

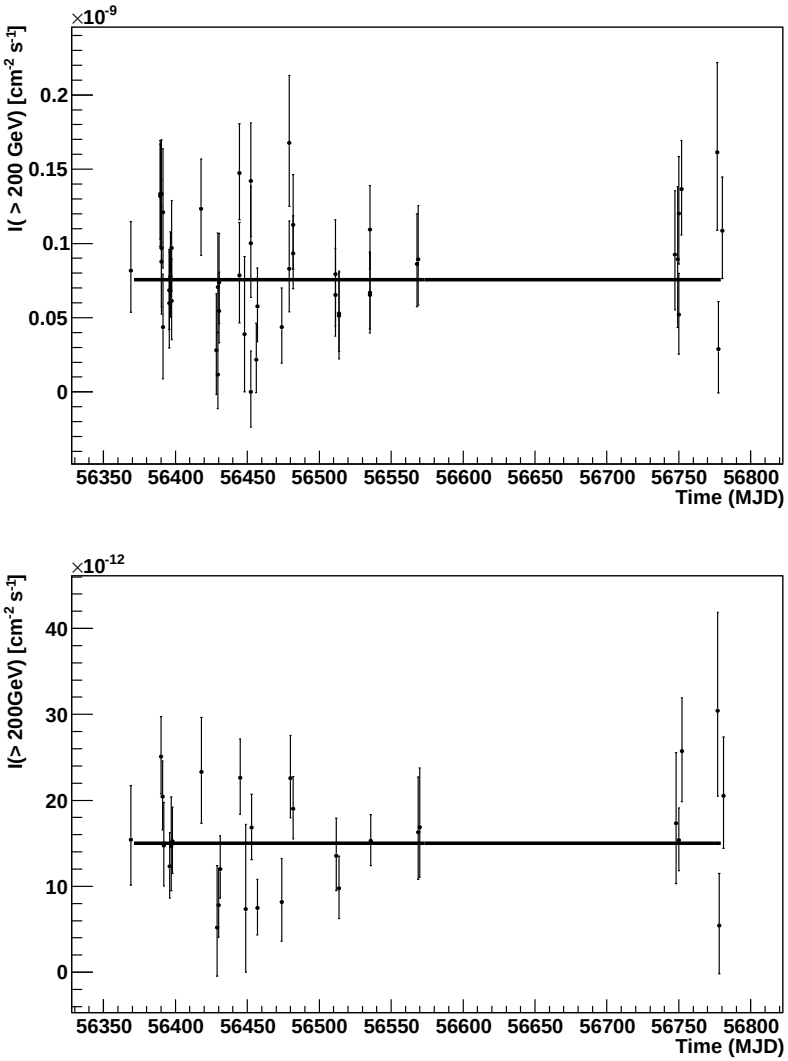

Figure 7.8: Runwise (top) and nightwise (bottom) lightcurves for dataset II

Table 7.3: Parameters of lightcurves of different binning for dataset I and II

Dataset I	Binning	Mean Flux($cm^{-2}s^{-1}$)	χ_2/d.o.f.
	runwise	$1.30*10^{-11}$	489.2/368
	nightwise	$1.37*10^{-11}$	209.5/148
	periodwise	$1.42*10^{-11}$	50.7/32
	yearwise	$1.43*10^{-11}$	8.8/7
Dataset II	runwise	$1.43*10^{-12}$	69.1/48
	nightwise	$1.50*10^{-12}$	41.5/28

Table 7.4: Flux and results of χ_2 test for the runwise lightcurves of dataset I

Year	Mean Flux($cm^{-2}s^{-1}$	χ_2/d.o.f.
2004	$1.38*10^{-11}$	95.3/86
2005	$1.30*10^{-11}$	152.2/108
2006	$1.35*10^{-11}$	72.6/48
2007	$1.27*10^{-11}$	21.2/15
2008	$1.27*10^{-11}$	41.1/24
2010	$1.15*10^{-11}$	16.4/19
2011	$1.27*10^{-11}$	23.5/21
2012	$1.25*10^{-11}$	91.1/64

7.5 Search for transient events

In order to check whether the lightcurves exhibit any variability, to what extent and what timescale, transient tests are performed on the overall lightcurves for both datasets and on the lightcurves of the years 2005, 2006, 2008 and 2012, which are the lightcurves showing variability from the χ^2 test.

Exptest

The values found for the normalized exptest estimator are listed in Table 7.5. For dataset I, the overall value is 0.13. For individual years, the value varies from 0.96 to 1.94, showing no prominent sign of variability. For dataset II, the estimator has a higher value of 5.7. Taken into account the larger systematics of HESS II, further tests are required to confirm variability.

The exptest is also applied to each run of both datasets (Fig. 7.9). For dataset I, the distribution of the exptest estimator can be fit with a normal distribution with a mean value of 0.09 and width of 0.98, indicating no transient events within a run. For the other dataset, the size is not large enough to be fit well with a Gaussian, but the mean value is 0.04 and no obvious deviation from the mean is seen.

Table 7.5: Values of the normalized exptest estimator of individual years of the lightcurves of Sgr A*

Dataset I	Year	Mr value
	2005	0.96
	2006	1.94
	2008	1.63
	2012	1.43
	overall	0.13
Dataset II	2013-2014	5.7

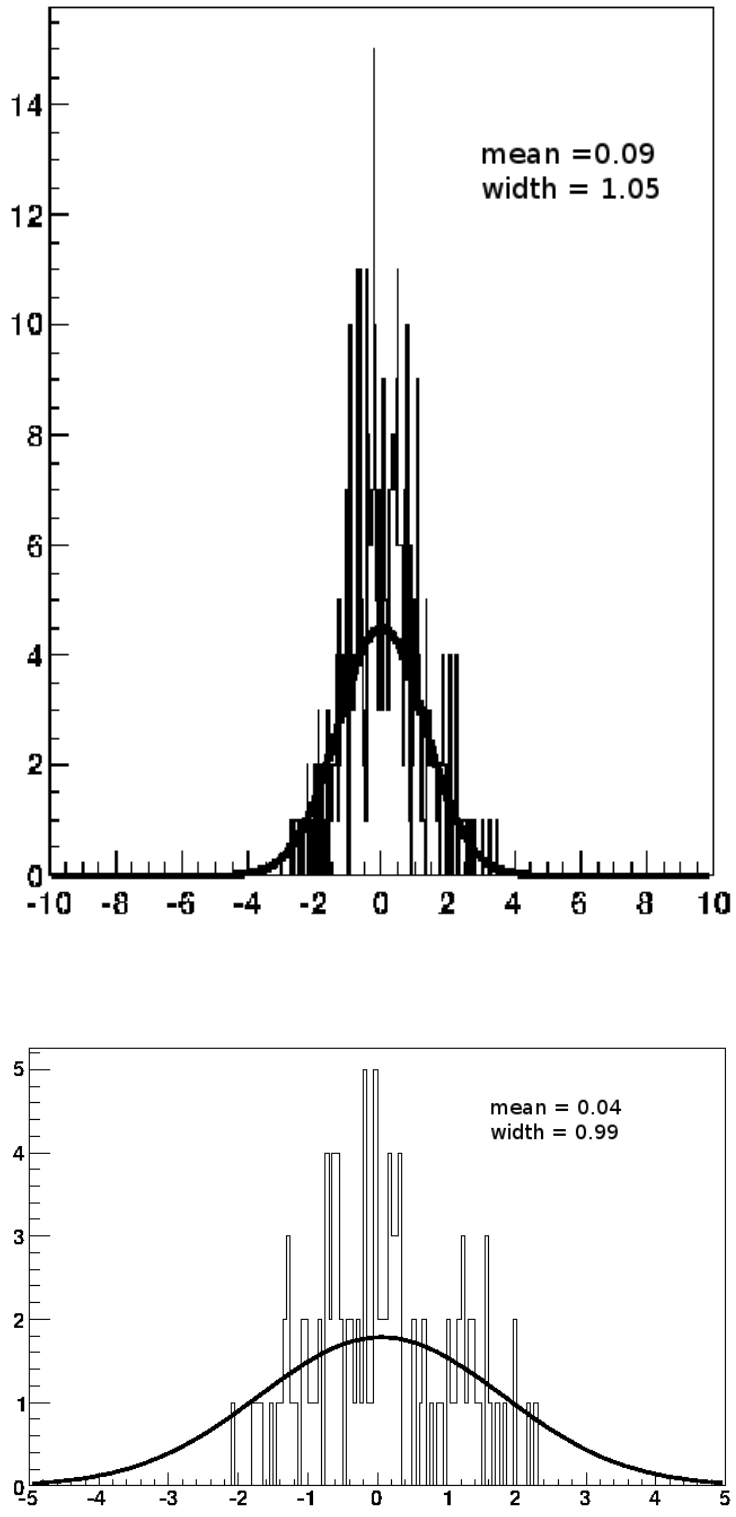

Figure 7.9: Distribution of the normalized exptest estimator for each run for dataset I (top) and dataset II (bottom). For dataset I, the data can be fit with a normal distribtuion with a mean of 0.09 and width of 0.98. For dataset II, the values for mean and width are 0.04 and 0.99 respectively. The results indicate no sign of transient events in a run.

Cumulative sum test

The test results for the overall lightcuves of both datasets are shown in Fig. 7.10. Both datasets show no clear tendency, but just fluctuations. The results for the years 2005, 2008, 2010 and 2012 are displayed in Fig. 7.11 and Fig. 7.12 respectively. Again these four years show fluctuations but no consistent downward trend.

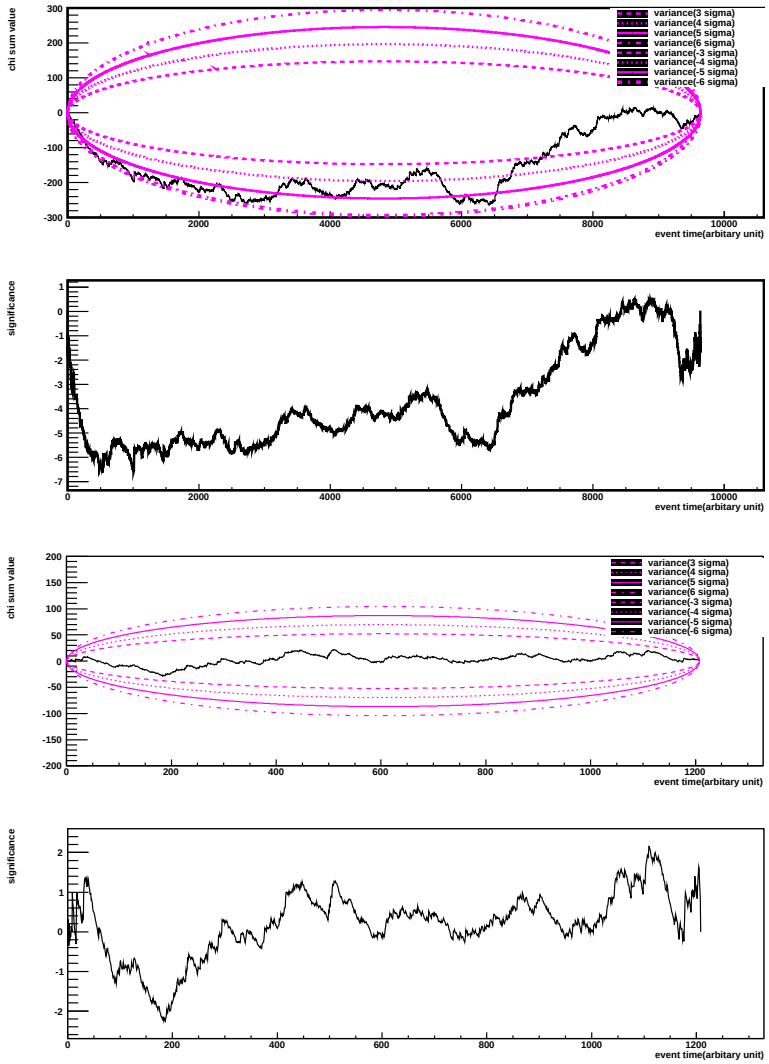

Figure 7.10: Cusum test results for dataset I (the first plot) and dataset II (the third plot). The red lines are contours for 3,4,5 and 6 standard deviations. The corresponding significance is the second and fourth plots. The purple curves show For both datasets, no obvious downward trend is observed, showing no transient activity.

On-off test

For the year 2005, 2006, 2008 and 2012, the results are in Fig. 7.14 and 7.15 for a time bin of 10 minutes. The significant distribution of each bin for these years can be fit with a normal distribution. Time bins of 20 and 30 minutes are also used for this test. Again no significant bin is found for these four years for all time bins tested.

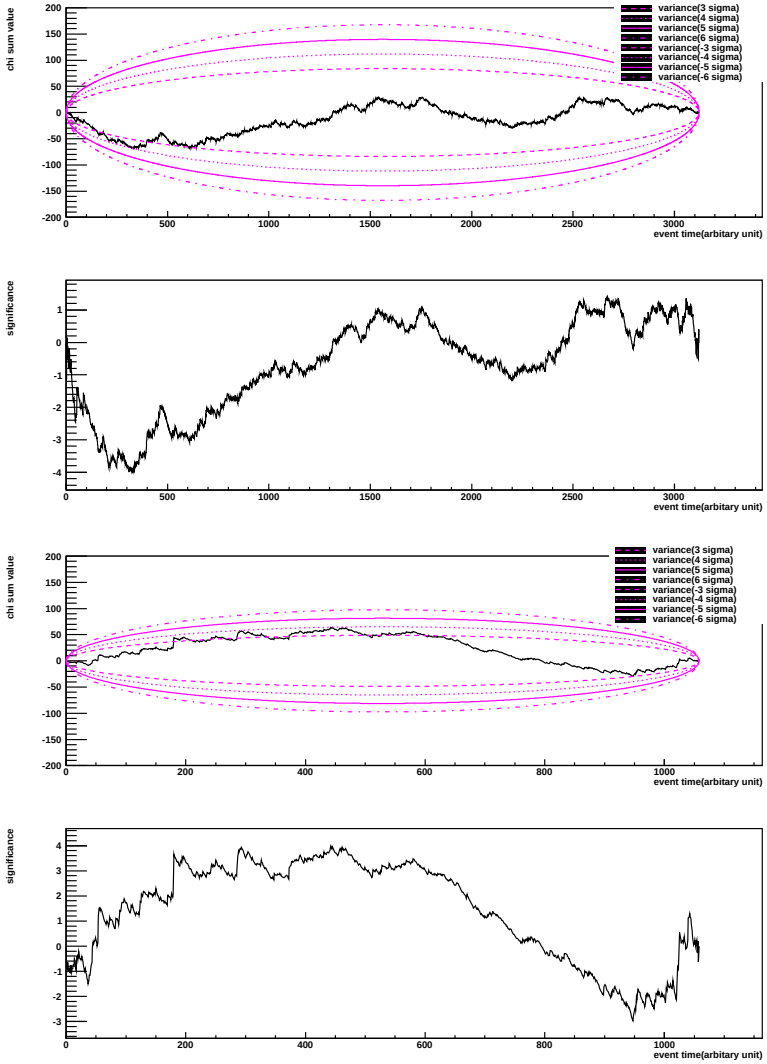

Figure 7.11: Cusum test results for the year 2005 (the first plot) and 2006 (the third plot). The corresponding significance is the second and fourth plot. For both years, no obvious downward trend is observed, showing no transient activity.

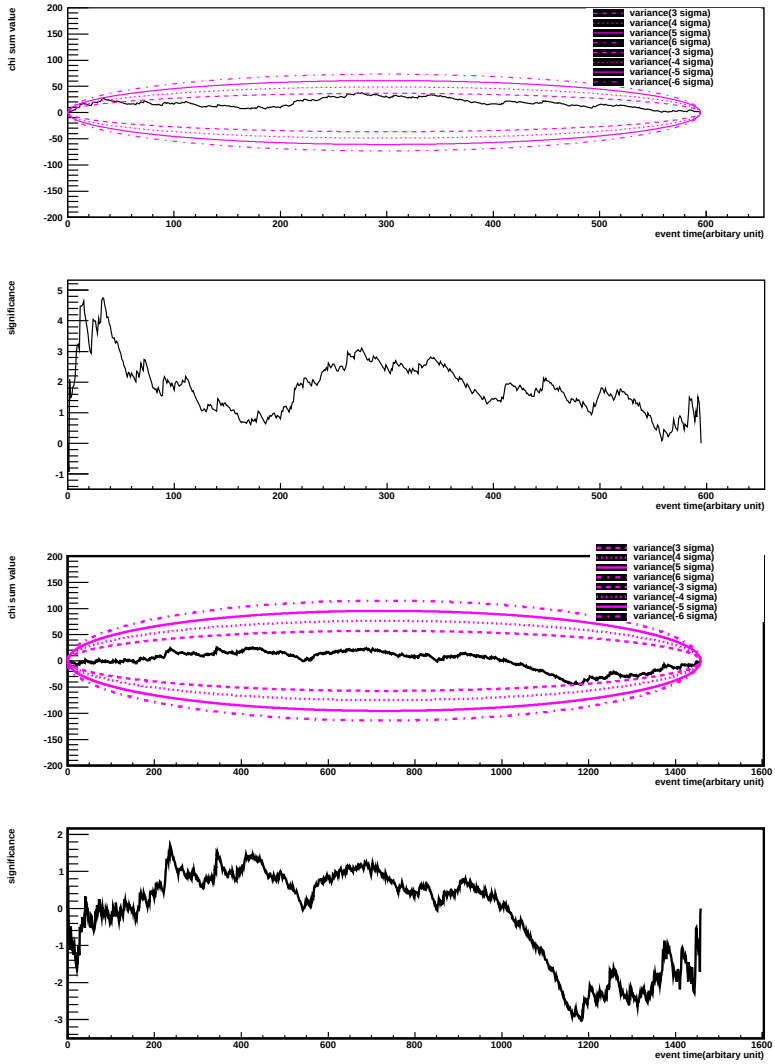

Figure 7.12: Cusum test results for the year 2008(the first plot) and 2010 (the third plot). The corresponding significance is the second and fourth plot. For both years, no obvious downward trend is observed, showing no transient activity.

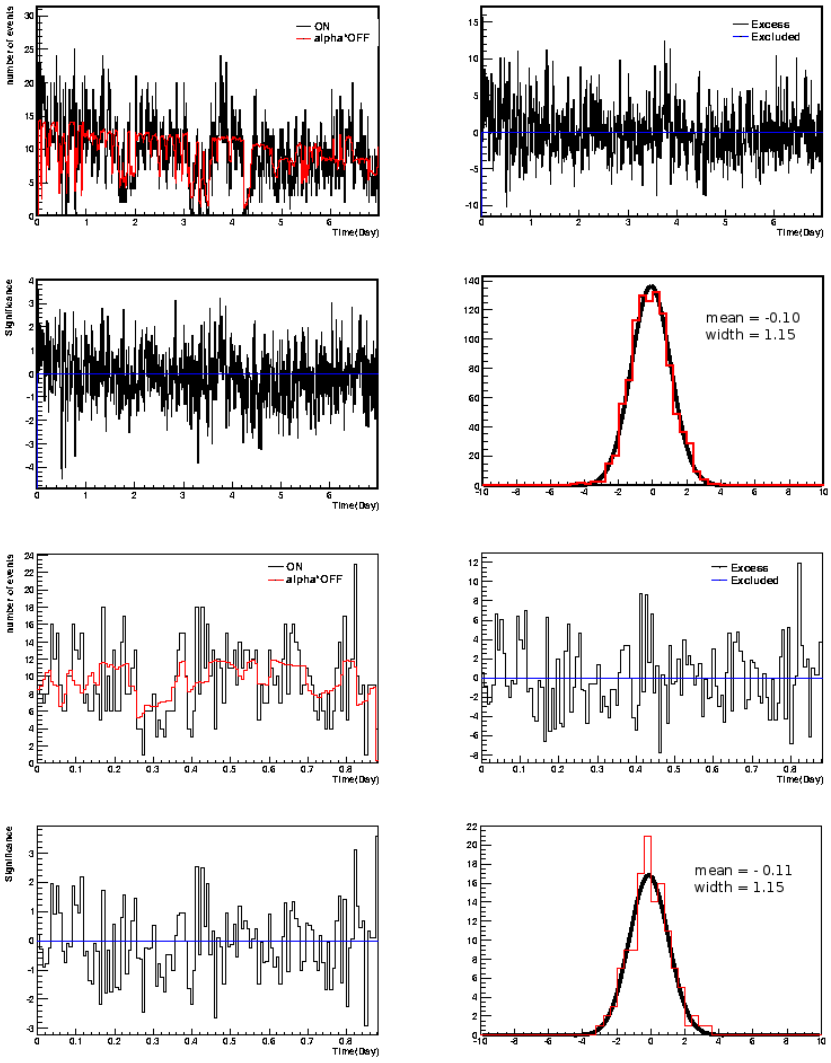

Figure 7.13: On-off test results for dataset I (top) and dataset II (bottom). A time bin of 10 mins is set. For each subplot,top left is the number of events in the on bin (black line) and the number of events in the off bin (red line). Top right is the excess plot, which is nOn - α nOff. Bottom left is the significance of each bin. Bottom right is the significance distribution of each bin. Both cases follow normal distribution.

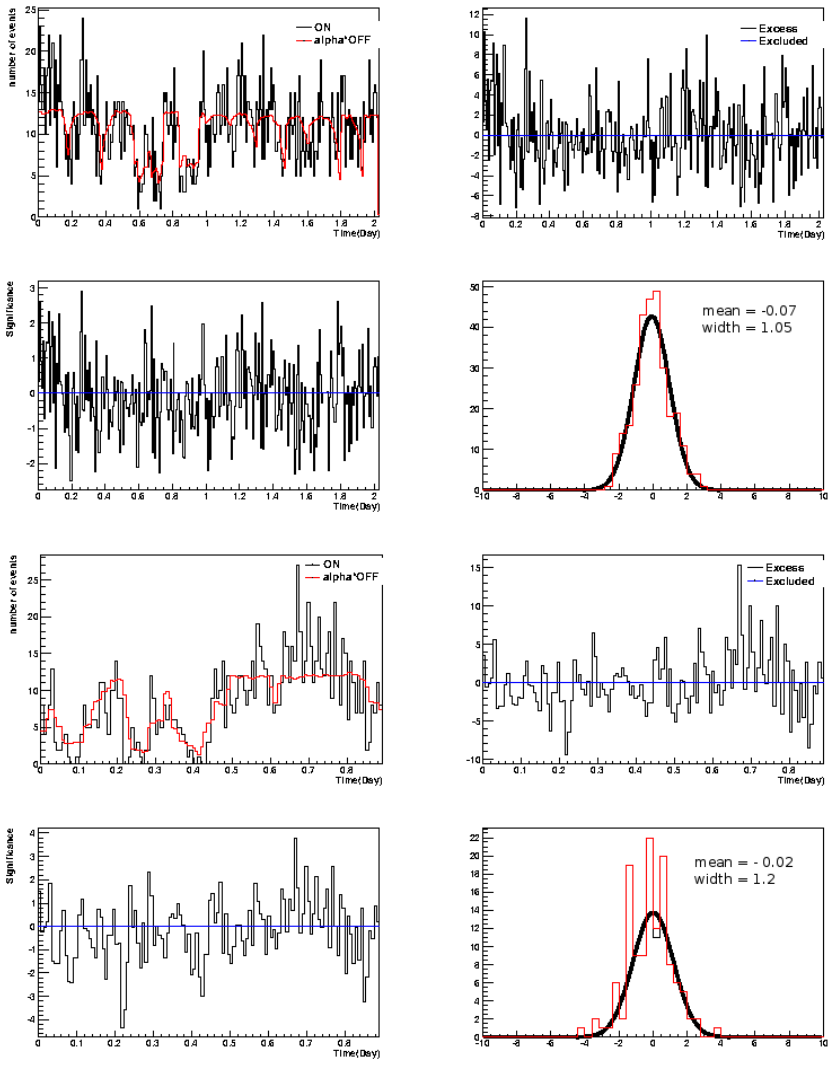

Figure 7.14: On-off test results for the year 2005 (top) and 2006 (bottom). A time bin of 10 mins is set. For each subplot,top left is the number of events in the on bin (black line) and the number of events in the off bin (red line). Top right is the excess plot, which is nOn - α nOff. Bottom left is the significance of each bin. Bottom right is the significance distribution of each bin. Both years follow normal distribution.

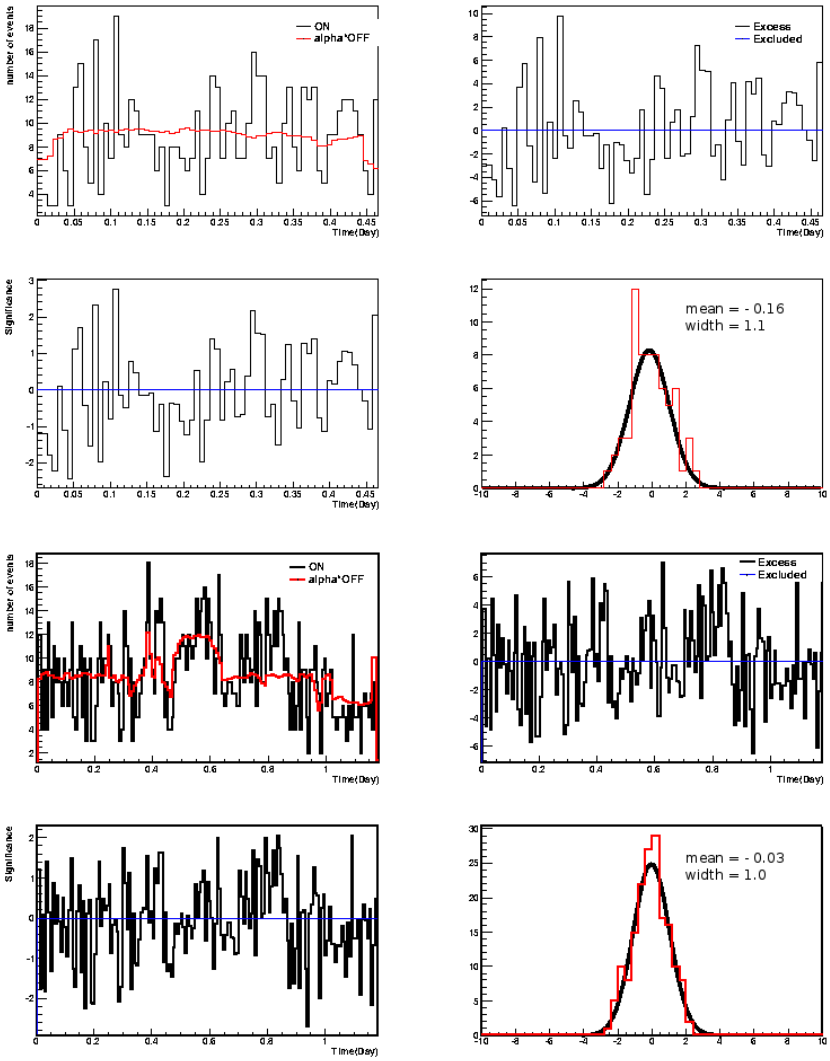

Figure 7.15: On-off test results for year 2008 (top) and 2012 (bottom). A time bin of 10 mins is set. For each subplot,top left is the number of events in the on bin (black line) and the number of events in the off bin (red line). Top right is the excess plot, which is nOn - α nOff. Bottom left is the significance of each bin. Bottom right is the significance distribution of each bin. Both years follow normal distribution.

7.6 Discussion

Using the dataset I which consists of 8 years of data, a strong signal has been detected from the GC central point position. The energy spectrum is best described by a power law with exponential cutoff. The index of found to be $\Gamma = 2.16 \pm 0.03\text{stat} \pm 0.11\text{syst}$ and the cutoff energy $E_{cut} = 14.16 \pm 2.66_{stat} \pm 2.41_{syst}$ TeV. For dataset II, the spectrum can be fit by a power law with an index $\Gamma = 2.20 \pm 0.05_{stat} \pm 0.11_{syst}$. Due to lack of statistics in the high energy regime, no energy cutoff is observed.

On short time scales, i.e. runwise, the overall lightcurves of both datasets show strong hints of variability from the χ^2 test. However, transient tests based on photon arrival times rather than the flux do not reveal such strong hints. Sgr A* remained stable from 2004 - 2012, which is the period covered by dataset I. For dataset II, which was taken around the pericentre passage time of G2, no evident flares were detected. This agrees with other findings dedicated to G2 in other wavebands (see Section 2.3 for details). G2 has been found to hold a central star inside, so it is likely that it resisted the force of gravity from the supermassive black hole and did not induce any increase in accretion rate. These results suggest that the source is non-variabile in the VHE regime. In the next step, other tests based on flux like Rayleigh test and Spectral Power Density can be applied to check for variability.

The lack of variability in the GeV and TeV regime found by Fermi and HESS and the frequent flaring activities in the IR and X-ray bands suggest that γ-ray emission has a different emission mechanism and regions. One natural explanation is that the IR and X-rays emission are generated close to the central black hole, while the γ-ray emission originates from a broader region and is emitted during the diffusion of the relativistic protons through the interstellar medium surrounding the central black hole.

To explain the broadband spectrum of the GC, different mechanisms have been invoked. For the emission in millimeter and shorter wavelengths, i.e. near- IR and X-ray flares, stochastic acceleration of electrons interacting resonantly with the turbulent magnetic field in the vicinity of Sgr A* ($\sim$ 20 Schwarzschild radii of Sgr A*) have been discussed by Liu et al. [138]. Electron energy is immediately re-radiated if there is large synchrotron and synchrotron self-Comptonized losses. The authors showed that protons are also accelerated in the same region, and they are accreted on the the black hole. By interacting inelastically with the interstellar medium, neutral pions are produced which later decay to form gamma rays. This model would also reproduce the IR and X-ray flaring [140].

This hadronic model predicts an energy cut-off in the γ-ray spectrum which reflects the energy cut-off in the primary proton spectrum. Assuming the strength of the cutoff β to be one (as did in Section 7.3), it would correspond to a energy cut-off of $\sim$ 400 TeV.

Other models explaining the TeV emission include Aharonian & Neronov [139]. This model is energy dependent and involves diffusion of protons to ouside of the central few parsecs of the Galaxy. A spectral break is predicted by this model due to competition between injection and escape of protons outside the vicinity of the GC.

Using combined Fermi-Lat and HESS data, a model [86] involving constant injection of relativistic protons for 10^4 years can explain the spectral energy distribution of the two telescopes. Since the duration of constant injection is longer than the diffusion time, the energy spectrum is expected to be steady. The TeV emission is due to high-energy protons escaping quasi-rectilinearly. The time is too short to suffer any spectral deformation. At low energies, fully trapped protons are also undistorted in the spectrum

since energy is independent of the pp cross-section. For particles having energies in between, they are not fully trapped and becomes diffusively steepened providing the transition between the two limiting cases.

This model can explain the combined spectral energy distribution of the Fermi and HESS data well. Since the TeV protons in this model left the source about ~ 10 years ago, variability in the TeV regime on ~ 10 year timescales is allowed. However, no variability in this work is noted using data from 2004 – 2014.

The PWN G359.95–0.04 is invoked in models leptonic models by Wang et al. [141] and Hinton & Aharonian [142]. The TeV emission is due to inverse Compton scattering of electrons of energies up to 100 TeV. This PWN model implies constant flux as the timescale for PWN changes is typically centuries to millennia. Another later model explaining the GeVTeV spectrum is by Kusunose & Takahara [143]. Within this model, the GeV emission is due to inverse Compton scattering from electrons injected during NIR/X-ray flares of the central source. The TeV emission comes from the nearby PWN G359.95-0.04. A hybrid leptonic-hadronic model developed by Guo et al. 2013 attributes the TeV emission to collisions of cosmic rays with the surrounding gas and GeV emission to IC scattering of electrons accelerated near the GC.

The above-mentioned models can predict the absence of variability and allow a cut-off in the γ-ray energy spectrum. They are possible scenarios to explain the strong TeV signal detected by HESS in the GC region. Due to lack of statistics in the high energy regime, the errors are large. Future generation Cherenkov telescopes having higher sensitivity, larger collection area and lower systematics should better constrain the spectrum at the high energy end of the spectrum. Thus, models can be better constrained.

7.7 Effect of Diffuse Emission on Lightcurves

This analysis aims to see the effect of diffuse emission on the lightcurves. Normally, for lightcurves reconstruction, off regions from above plane, below plane and on plane are chosen without any distinction. In order to study the effect of diffuse emission, off regions are chosen from 5 different regions to see how the flux estimation is affected. These 5 regions are

1. above plane (galactic latitude > 1)
2. below plane (galactic latitude < -1)
3. on plane (-1< galactic latitude < 1) (which is "middle" in the plots)
4. outside plane (galactic latitude < -1 or galactic latitude > 1)
5. All (no distinction in the choice of off regions)

Regions with galactic latitude +1 and -1 are respectively defined as "above" and "below" plane because diffuse emission becomes insignificant outside this region [137].

Fig. 7.16 shows the latitude distribution of the off regions for all runs. The off regions are more often found in the below plane region.

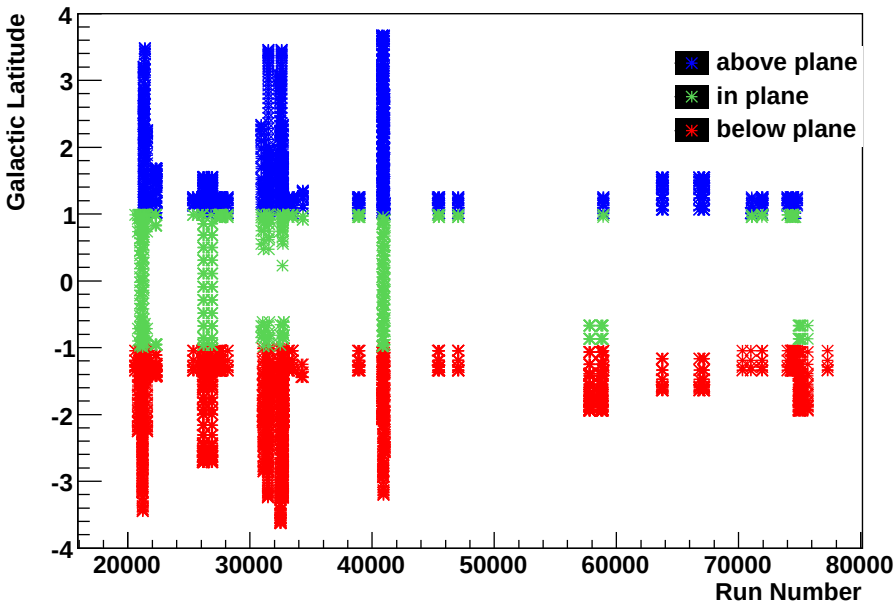

Figure 7.16: Latitude distribution of off regions for all runs.

Fig. 7.17 show the differential runwise lightcurves, i.e. lightcurves with off regions chosen from a particular region - lightcurves with off regions chosen with no distinction. For the top left, for example, it is the lightcurves with off regions only from above plane minus the lightcurves with off regions chosen with no distinction in the region. The percentage change in flux when choosing off regions from all regions to only a particular region is listed in Table 7.6. As can be seen from Fig. 7.17 and Table 7.6, “middle minus all” shows the largest deviation. The flux change in percentage is 0.05%. This is expected because the diffuse emission mainly lies within latitude ±1. Since the change in flux is very small no matter where the off regions are chosen from, the impact on the measured flux is minimal.

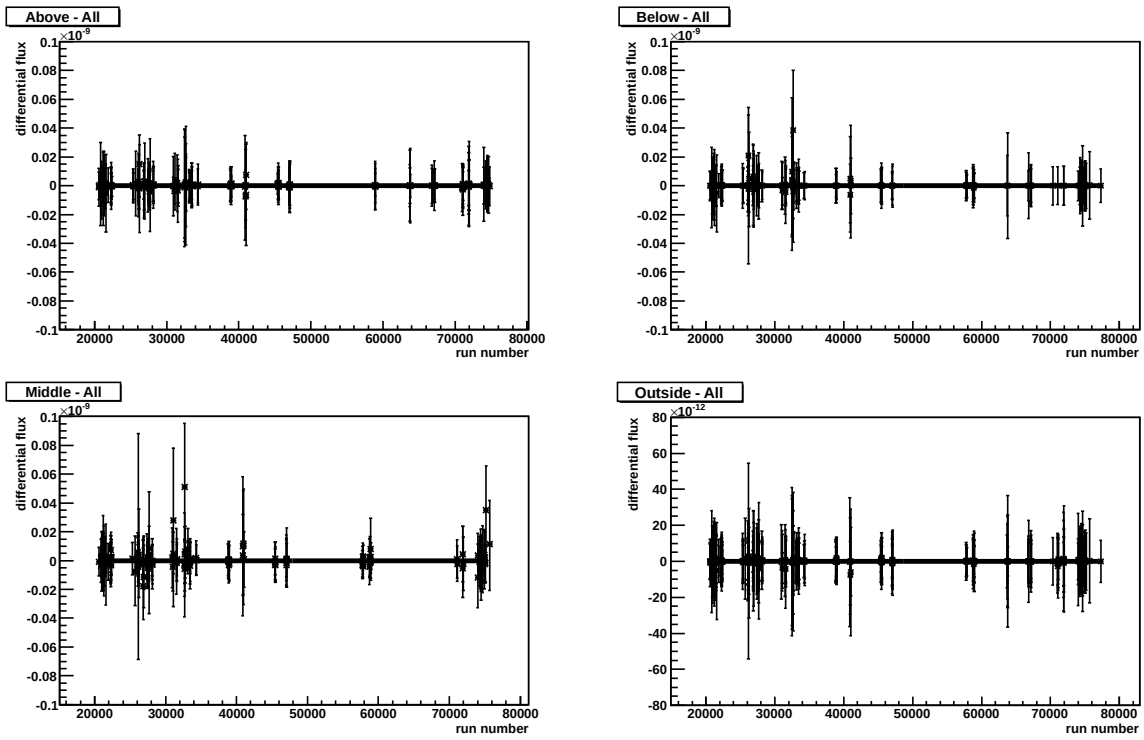

Figure 7.17: Differential lightcurves of Sgr A*, i.e. lightcurves with off regions selected from a particular region minus lightcurves selected from all regions. The horizontal line is the mean value for the data set. Top left: lightcurves with off regions from above plane - lightcurves with off regions from all. Top right: lightcurves with off regions from below plane - lightcurves with off regions from all. Bottom left: lightcurves with off regions from middle plane - lightcurves with off regions from all. Bottom right: lightcurves with off regions from outside plane - lightcurves with off regions from all. As can be seen, "Middle - All" shows the larges deviation. This is expected since diffuse emission mainly comes from the in plane region.

Table 7.6: A table of the change in percentage in flux when choosing off regions from different regions

Differential Lightcurves	Percentage change in flux(%)
Above - All	0.01
Middle - All	0.05
Below - All	0.04
Outside - All	0.002

Chapter 8

CTA - the next generation ground-based Cherenkov telescope

During the last two decades, the field of TeV γ-ray astronomy has made rapid development and has become a branch of modern astronomy. This field is also interesting for physicists as it provides them with a chance to study energies beyond the limits of present and future particle accelerators. From TeV observations, constraints can be put on the intrinsic spectrum of emitting particles and thus more information on the nature of the particles and acceleration mechanisms can be revealed. They also have an impact on modern cosmology. Fundamental issues like dark matter, Lorentz invariance violation and evaporation of primordial black holes can be explored by means of TeV observations.

For Galactic Centre research, γ-ray emission has been detected from HESS J1745-290. The earliest study made by HESS [144], was within 7" coincident with Sgr A*. Due to the complexity of the GC region, a solid identification could not be made until later [145], when systematic and statistical errors improved to such an extent that Sgr A East could be excluded as the major γ-ray source in this region. However, since there is no variability found between γ-ray and X-ray emission, HESS J1745-290 cannot be firmly assiciated with Sgr A*. The lack of variability may be either due to the insufficient sensitivity of the instrument or different emission regions between γ-ray and X-ray. The GC γ-ray emission may also be of hadronic origin stemming from a region farther away from the GC itself (e.g. Ferriere (2012)) or even due to dark matter (e.g. [144] [147]). In order to probe the nature of GC γ-ray emission, a more advanced instrument with better sensitivity, angular resolution and broader energy range is a must. This calls for more advanced technology. CTA (Cherenkov Telescope Array) is the next-generation state-of-the-art Cherenkov telescope. It not only has better angular and energy resolution, but also larger effective area and wider field of view which allow observations of much lower fluxes at higher energies, enabling the study of short time scale variability. It is particularly good for detecting transient phenomena since its sensitivity is 10 times higher compared to H.E.S.S. (see Fig. 8.1 for the predicted sensitivity). In this section, a brief introduction to CTA is given.

8.1 An Introduction to CTA

CTA is a multinational project involving more than 200 institutes from over 30 countries. The aim of the project is to build a new generation ground-based gamma-ray instrument in the energy range from some tens of GeV to over 100 TeV. The low energies will have overlap with Fermi, allowing simultaneous observations for better understanding of γ-ray sources. Fermi can complement CTA for observations down to MeV energies while CTA will have a sensitivity for short-timescale phenomena that is orders of magnitude higher than that of Fermi. Compared with current Cherenkov telescopes H.E.S.S., Magic and Veritas, CTA will have a flux sensitivity which is a magnitude higher.

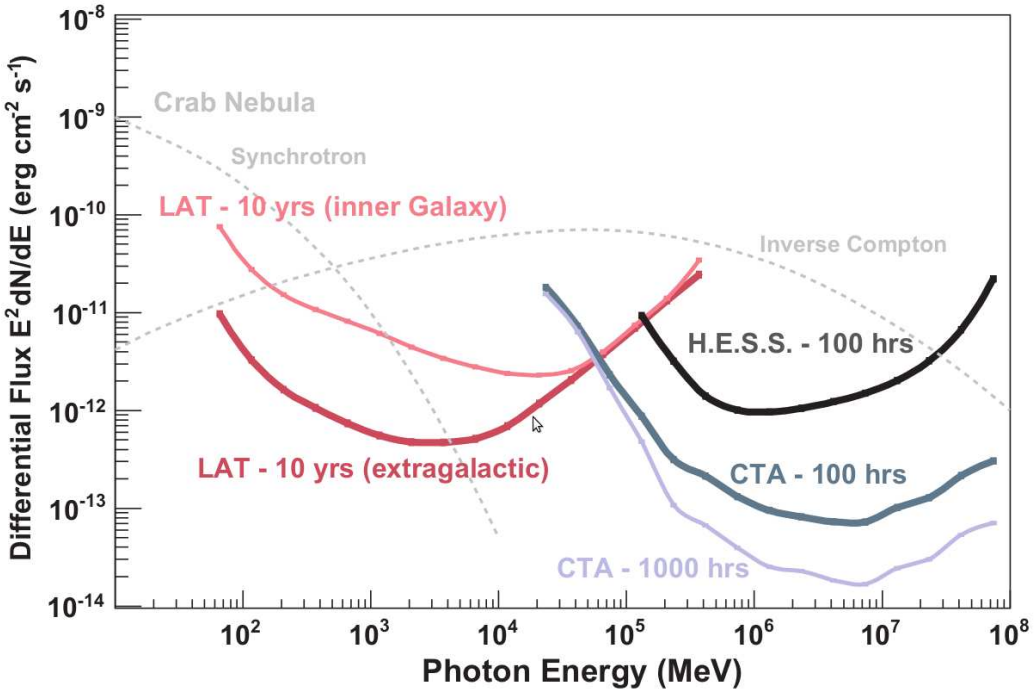

Figure 8.1: Predicted sensitivity of CTA compared with other high energy telescopes. The sensitivity is defined as the dimmest source radiation flux needed for a detection with a significance of 5 standard deviations. Image taken from [148].

This advanced instrument is expected to largely increase the number of detectable objects and the work requires the collaboration with scientists working in other wavelength ranges. Thus, it is proposed as an open observatory. Moreover, releasing data to the public and supporting their use can maximize the scientific return of an observatory.

CTA will consist of two arrays of Imaging Atmospheric Cherenkov telescopes. One is the main site at the Southern Hemisphere which aims to cover the full energy range and concentrate on galactic sources. The other is at the Northern Hemisphere whose aim is to study extragalactic objects like AGNs at the lowest possible energies. The physics program of CTA is not only high energy astrophysics but also cosmology and fundamental physics.

As of September 2015, the CTA Resource Board is in contract negotiations for hosting CTA on the European Southern Observatory (ESO) Paranal grounds in Chile and at the Instituto de Astrofisica de Canarias (IAC), Roque de los Muchachos Observatory in La Palma, Spain.

8.2 Design Concept

Current IACTs adopts a stereoscopic principle by viewing a shower with four telescopes at the same time at most. However, since the whole array is within the light pool, the number of γ-rays detected are limited. With tens of telescopes for CTA, the collection area on ground is greatly increased, allowing the detection of a large number of γ-rays. This also provides a larger number of views of each cascade, improving the angular resolution and better suppressing background events.

For each CTA site in the southern and northern hemispheres, 50-100 telescopes per

site will be placed (Fig. 8.2). This ensures full sky coverage. Since CTA is designed to cover a wide energy range from tens of GeV to some 10 TeV and achieve a higher sensitivity, a combination of telescopes of three sizes are required. The large ones are for the lowers energies, medium ones for the core energy range and small ones for the highest energies. At the southern site, all three types of telescope with different mirror sizes are placed to achieve full energy range while the northern site will only have the two larger telescope types. A possible layout derived from Monte-Carlo simulations is shown in Fig. 8.3.

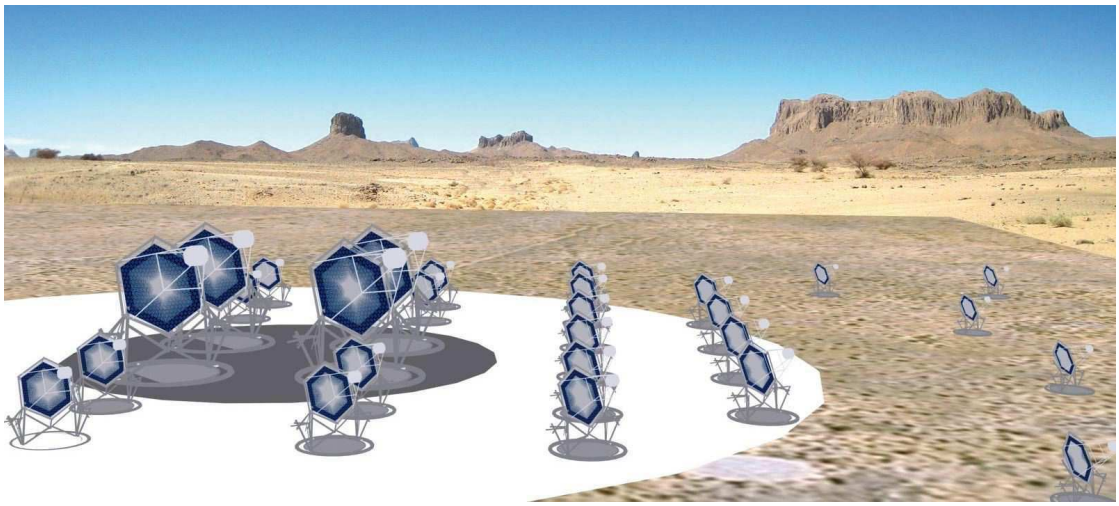

Figure 8.2: Artist view of CTA (not to scale). Image taken from [149].

A brief description of the three types of telescopes is given here.

• Large-Size Telescopes(LSTs):

They are designed to detect low energy photons within the energy range from a few tens of GeV to about a hundred GeV. At low energies, event rates are high and sensitivity is low due to insufficient background rejection. Thus, the area of this part of the array can be relatively small, $\sim$ 10,000 m^2. Efficient photon detection can be reached with a few large telescopes. CTA will deploy an array of 3 to 4 telescopes of a 23-metre dish with a FoV of 4-5°, spaced about 100m apart. The design concept is shown in Fig. 8.4.

• Medium-Size Telescopes (MSTs):

They are designed for the core energy range, i.e. $\sim$100 GeV to 1 TeV, having a 10-12 metre dish with a FoV of 6-8°. Current IACTs operate at this energy range. CTA can achieve better sensitivity by deploying a large number of telescopes to increase area and improve the quality of shower reconstruction. It is the first time that the array size is larger than the Cherenkov light pool. This ensures uniform sampling across the light pool and optimum distance between shower images and the shower axis (about 70-150 m). Two possible designs for an MST is illustrated in Fig. 8.5.

• Small-Size Telescopes (SSTs):

They are designed to operate above 10 TeV and consist of a large number of small telescopes having a 4-6 metre dish with a FoV around 10°. At such a high energy range, the number of γ rays is small but the light yield is large, which means the showers can be detected well beyong the Cherenkov light pool. In order to significantly improve the sensitivity at the highest energies, a large collection area of the order of 10 km^2 is needed. This means the telescopes are spread over a large area. Fig. 8.6 shows three possible designs for SSTs.

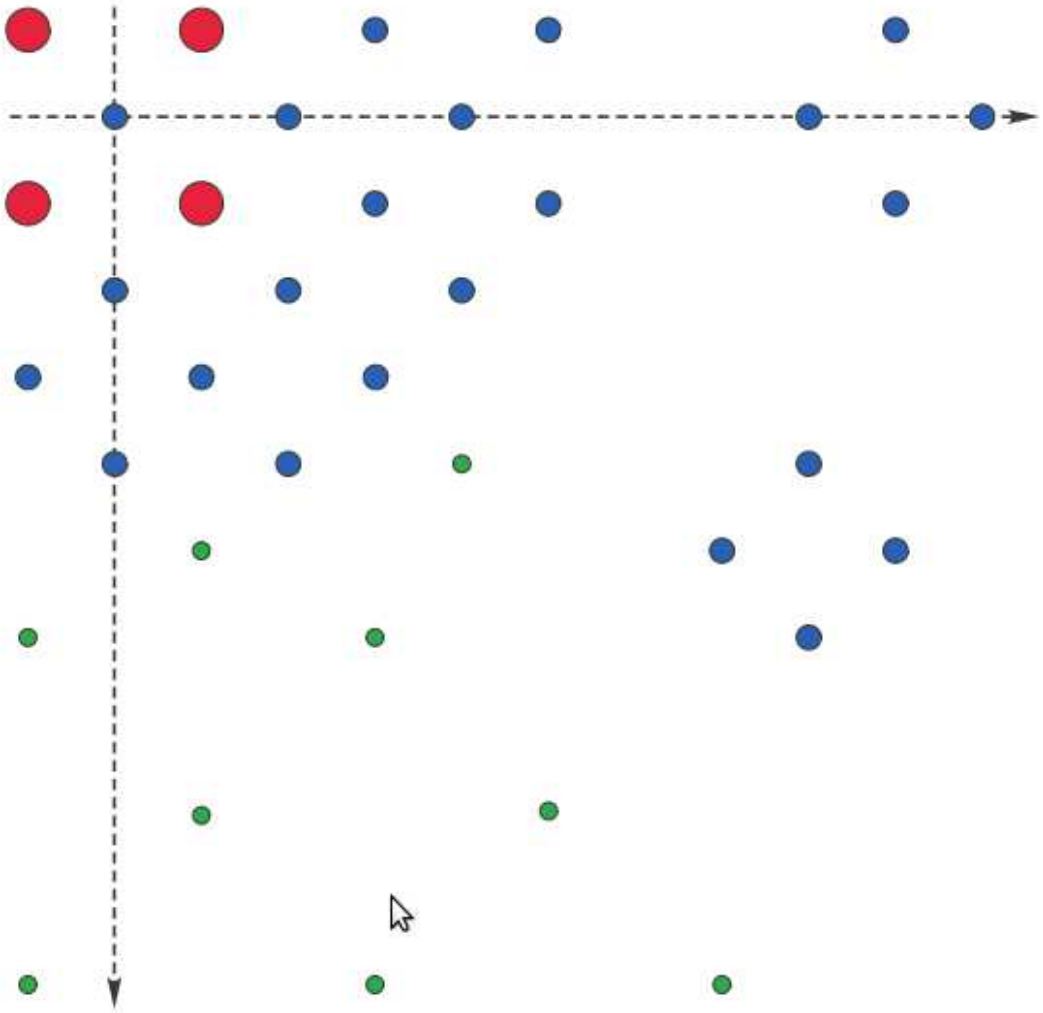

Figure 8.3: A quadrant of possible array schemes providing excellent sensitivity over an extended energy range, as suggested by the Monte Carlo studies. Near the upper left corner, the centre of the installation is shown. Clusters of telescopes of the 12 m class are shown at the perimeter in the upper right part. In the lower left part, the wide-angle telescopes of the 3-4m class are optional. Image taken from [149].

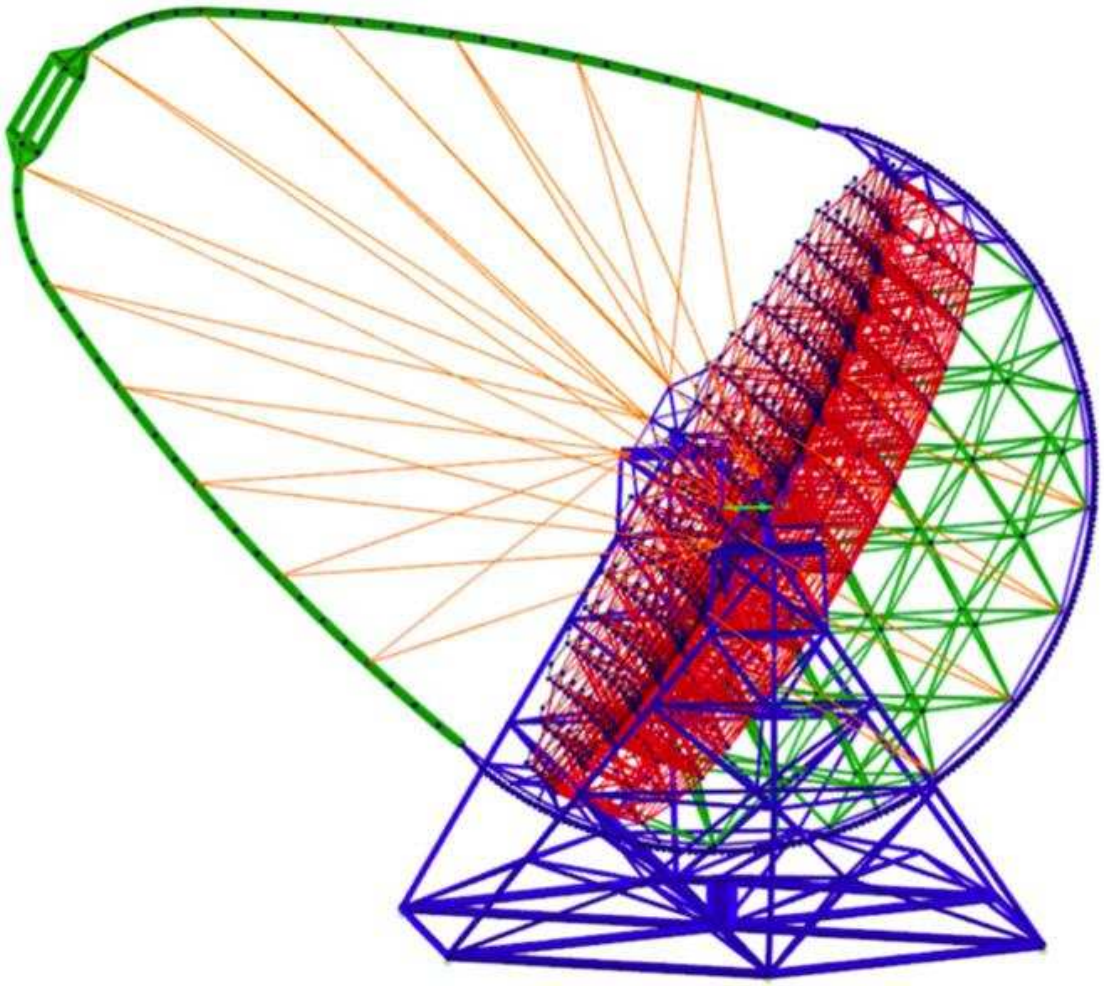

Figure 8.4: Design concept for an LST of CTA. The diameter is 23m, FoV 4.5° and there are 2500 pixels of 0.1° diameter. Image taken from [150].

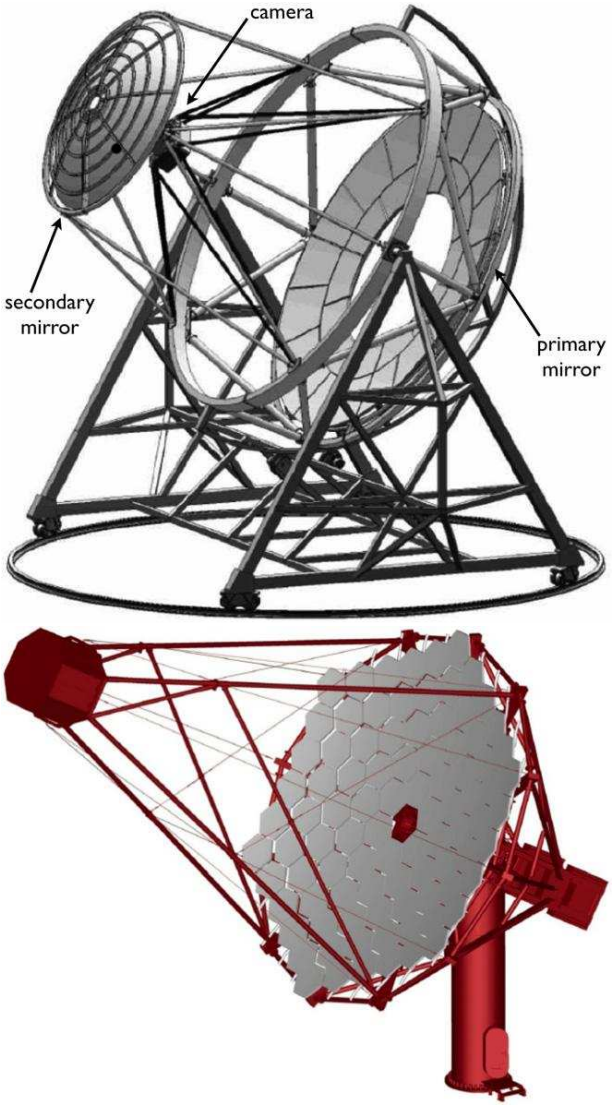

Figure 8.5: (Left) Design concept for a Schwarzschild-Couder dual-mirror MST. Close to the secondary mirror there is a compact camera. The FoV is 8° and the number of square pixel is 11000, each having a side length of 0.067°. Image taken from [150].

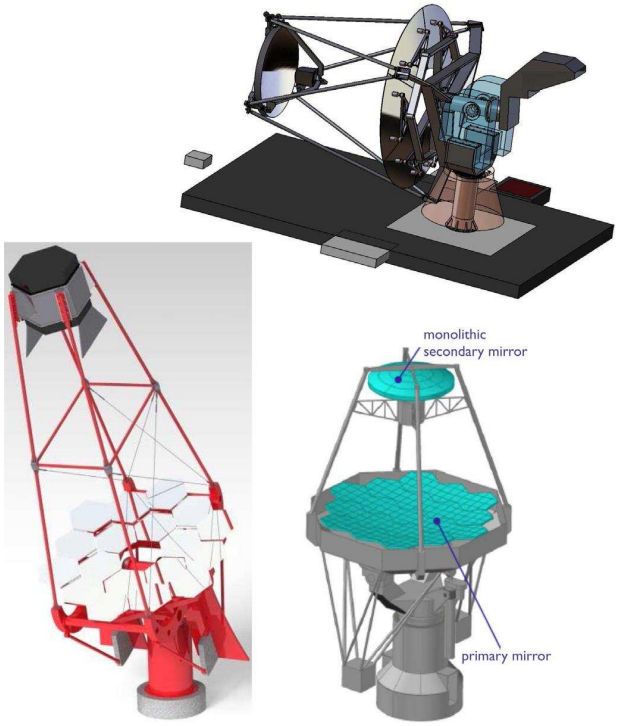

Figure 8.6: Three possible designs for SSTs. The dish diameter is about 4m, FoV about 8-10°, number of pixels 1300-2000 and pixel size 0.2-0.3°. Bottom left: Traditional Davies-Cotton design with f/D = 1.4 and a large camera. Top and bottom right: Schwarzschild-Couder dual-mirror optics. Image taken [150].

8.3 Performance

In order to test the performance of CTA, Monte Carlo simulations have been performed assuming the following:

- The southern site has 4 LSTs, 24 MSTs and 72 SSTs. The total area covered is $\sim$ 4 km^2.
- The northern site has 4 LSTs and 15 MSTs. The total area covered is ~ 0.4 km^2.
- The source is point-like with a spectral shape similar to that of the Crab Nebula.
- The source is placed at the centre of the FoV and at a zenith angle of 20°.

Sensitivity: CTA will be about an order of magnitude more sensitive than any current IACT in the same energy range. This will allow the exploration of suspected γ-ray sources and in-depth study of known sources. Below (Fig. 8.7) is the differential energy flux sensitivity in five independent logarithmic bins per decade of energy. In each bin the required confidence level is 5σ.

Angular Resolution: Though existing IACTs can resolve extended sources, they cannot resolve the fine structures visible in other wavelengths. For energies above 1 TeV, CTA can reach angular resolutions of less than 2 arc minutes by selecting a subset of γ-ray induced cascades, which is a factor of 5 better than current instruments. Fig 8.8 illustrates the change in the 68% containment radius (as mentioned in Chapter 4) with energies.

Energy Resolution: CTA not only covers a wide energy range but also has better energy resolution and lower statistical errors. This is vital in distinguishing between key hypotheses such as leptonic or hadronic models of γ rays from SNRs. This also contributes to the line detection from dark matter clusters. In Fig. 8.9, the energy

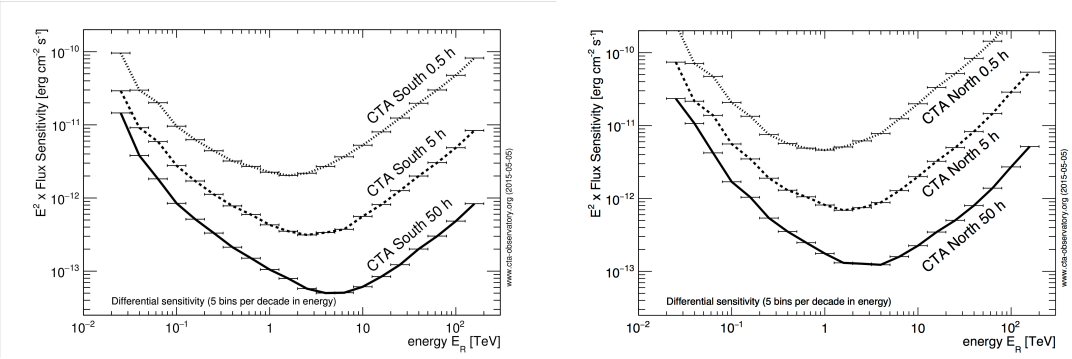

Figure 8.7: Differential energy flux sensitivity for the southern (left) and northern (right) sites. Image taken from [151].

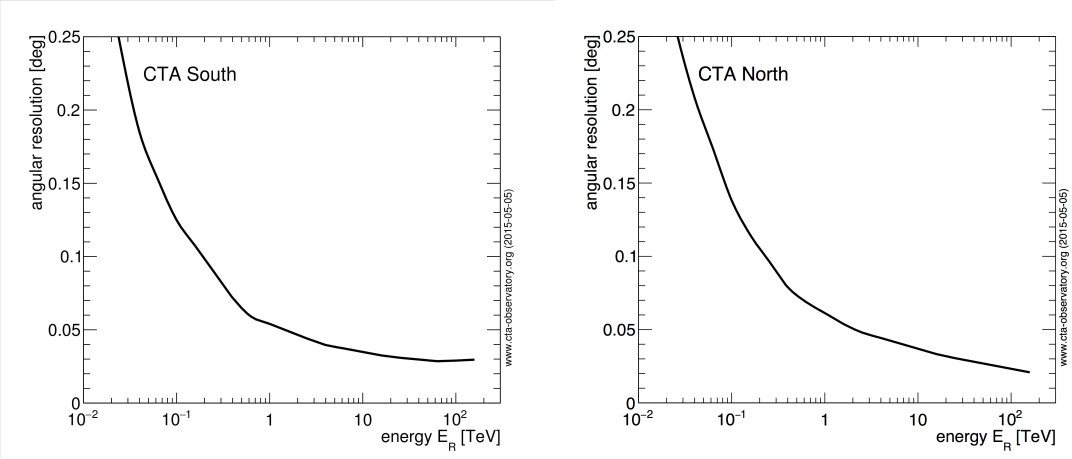

Figure 8.8: The 68% containment radius for the southern (left) and northern (right) sites. Image taken from [151].

resolution is defined as the half width of the ±34% interval around the most probable reconstructed energy, divided by the most probable reconstructed energy.

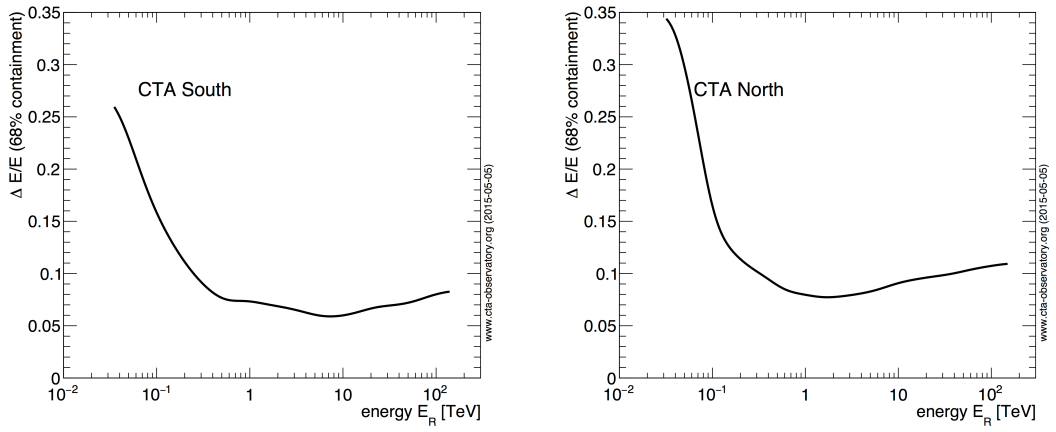

Figure 8.9: Energy resolution for the southern (left) and northern (right) sites. Image taken from [151].

8.4 Outlook

CTA is a worldwide project which is already considered one of the leading large observatories of this decade. The idea dates back to 2005. It was originally promoted by HESS and MAGIC members. It soon became apparent that IACT can have higher sensitivity and a wider energy range with an array of a large number (≈100) of telescopes of different sizes.

CTA has been highly reviewed in Science Roadmaps in Europe and around the world. It is highly ranked in future projects of ApPEC, ASPERA and ASTRONET. Additionally, CTA is a prioritized project for the present decade in the Decadal Survey of the US National Academy of Sciences [152].

CTA can provide answers to long-standing questions in a number of science areas. It is going to be the first large open observatory of the extreme universe beyond the GeV range. It is certainly worth the effort, as CTA will provide a good science return in astrophysics, particle physics, cosmology and fundamental physics, and lead to a bright future for ground-based gamma ray astronomy.

Bibliography

[1] E. Rutherford and E. Andrade, "The wavelengths of soft X-rays from Radium B," Philos. Mag. **27**, 854 (1959).

[2] J. Clay, "The Earth-magnetic effect and the corpuscular nature of ultra-radiation," Proc. Roy. Acad. Amsterdam **35**, 1282 (1932).

[3] H. Yukawa, "On the Interaction of Elementary Particles. I," Proc .Phys.-Math Soc Jpn **17**, 48 (1935).

[4] E. Gardner and C. Lattes, "Production of Mesons by the 184-Inch Berkeley Cyclotron ," Science **107**, 270 (1948).

[5] E. Feenberg and H. Primakoff, "Interaction of Cosmic-Ray Primaries with Sunlight and Starlight," Phys. Rev. **73**, 449 (1948).

[6] S. Hayakawa, "Propagation of the cosmic radiation through the interstellar space," Prog. Theo. Phys **8**, 571 (1952).

[7] G. Hutchinson, Phil. Mag. **43**, 847 (1952).

[8] P. Morrison, "On gamma-ray Astronomy," Nuovo Cimento 7 **6**, 858 (1958).

[9] R.A. Ong, "Very high-energy gamma-ray astronomy," Physics Reports **305**, 93 (1998).

[10] J. Weekes, "Very high energy gamma-ray astronomy," Physics Reports **160**, 1 (1988).

[11] W.L. Kraushaar, G.W. Clark, and G. Garmire, "Preliminary results of gamma-ray observations from OSO-3," Can. J. Phy. **46**, S414 (1968).

[12] C. E. Fichtel, R. C. Hartman, D. A. Kniffen, et al., "High-energy gamma-ray results from the second small astronomy satellite," A&A **198**, 163 (1975).

[13] R. C. Lamb, C. W. Akerlof, M. F. Cawley, et al., "Observations of TeV photons at the Whipple Observatory," AIPC **220**, 47L (1991).

[14] M. Punch, C. W. Akerlof, M. F. Cawley, et al., "Detection of TeV photons from the active galaxy Markarian 421," Nature **358**, 477 (1992).

[15] J. Haefner, "New improved Sum-Trigger system for the MAGIC telescopes," ICRC Proceedings **9**, 251 (2011).

[16] B. M. Gaensler and P. O. Slane, "The Evolution and Structure of Pulsar Wind Nebulae," ARA&A **44**, 17 (2006).

[17] A. Spitkovsky, "Particle Acceleration in Relativistic Collisionless Shocks: Fermi Process at Last?," ApJ **682**, 5 (2008).

[18] L. Sironi and A. Spitkovsky, "Particle Acceleration in Relativistic Magnetized Collisionless Electron-Ion Shocks," ApJ **726**, 75 (2011).

[19] E. Amato and J. Arons, "Heating and Nonthermal Particle Acceleration in Relativistic, Transverse Magnetosonic Shock Waves in Proton-Electron-Positron Plasmas," ApJ **653**, 325 (2006).

[20] A. Stockem, F. Fiuza, and R. A. Fonseca, "Acceleration in Perpendicular Relativistic Shocks for Plasmas Consisting of Leptons and Hadrons," ApJ **755**, 68 (2012).

[21] Y. E. Lyubarsky, "Fast magnetosonic waves in pulsar winds," MNRAS **339**, 765 (2003).

[22] S. P. Clay, "Supernova Remnants at High Energy," ARA&A **46**, 89 (2008).

[23] K. W. Weiler and R. A. Sramek, "Supernovae and Supernova Remnants," ARA&A **26**, 295 (11988)C. E. Fichtel, R. C. Hartman, D. A. Kniffen, et al., "High-energy gamma-ray results from the second small astronomy satellite," A&A **198**, 163 (1975).

[24] F. Aharonian, A.G. Akhperjanian, A.R. Bazer-Bachi, et al., (H.E.S.S. Collaboration), "A detailed spectral and morphological study of the gamma-ray supernova remnant RX J1713.7-3946 with HESS," A&A **449**, 223 (2006).

[25] F. Aharonian, A.G. Akhperjanian, A.R. Bazer-Bachi, et al., (H.E.S.S. Collaboration), "H.E.S.S. Observations of the Supernova Remnant RX J0852.0-4622: Shell-Type Morphology and Spectrum of a Widely Extended Very High Energy Gamma-Ray Source," ApJ **661**, 236 (2007).

[26] F. Aharonian, A.G. Akhperjanian, A.R. Bazer-Bachi, et al., (H.E.S.S. Collaboration), "Primary particle acceleration above 100 TeV in the shell-type supernova remnant RX J1713.7-3946 with deep HESS observations," A&A **464**, 235 (2007).

[27] D. Caprioli, "Understanding hadronic gamma-ray emission from supernova remnants," JCAP **5**, 26C (2011).

[28] E. G. Berezhko, L. T. Ksenofontov, and H. J. Voelk, "Confirmation of strong magnetic field amplification and nuclear cosmic ray acceleration in SN 1006," A&A **80**, 885 (2003).

[29] D. Böck, "Observations of active galactic nuclei from radio to gamma rays," JCAP **PhD Thesis**, (2012).

[30] L. Maraschi, G. Ghisellini, and A. Celotti, "A jet model for the gamma-ray emitting blazar 3C 279," ApJ **397**, L5 (1992).

[31] S.D. Bloom and A.P. Marscher, "An Analysis of the Synchrotron Self-Compton Model for the Multi–Wave Band Spectra of Blazars," ApJ **461**, 657 (1996).

[32] C. D. Dermer, R. Schlickeiser, and A. Mastichiadis, "High-energy gamma radiation from extragalactic radio sources," A&A **256**, L27 (1992).

[33] M. Sikora, M. C. Begelman, and M. J. Rees, "Comptonization of diffuse ambient radiation by a relativistic jet: The source of gamma rays from blazars?," ApJ **421**, 153 (1994).

[34] G. Ghisellini, F. Tavecchio, and M. Chiaberg, "Structured jets in TeV BL Lac objects and radiogalaxies. Implications for the observed properties," A&A **432**, 401 (2005).

[35] K. Mannheim and P. L. Biermann, "Gamma-ray flaring of 3C 279 - A proton-initiated cascade in the jet?," A&A **253**, 21 (1992).

[36] A. Dar and A. Laor, "Hadronic Production of TeV Gamma-Ray Flares from Blazars," ApJ **478**, L5 (1997).

[37] J. H. Beall and W. Bednarek, "On the Hadronic Beam Model for Gamma-Ray Production in Blazars ," ApJ **510**, 188 (1999).

[38] F. Aharonian, *Very high energy cosmic gamma radiation*, 3rd ed. (World Scientific, 2004).

[39] M. Pohl and R. Schlickeiser, "On the conversion of blast wave energy into radiation in active galactic nuclei and gamma-ray bursts ," A&A **354**, 39 (2000).

[40] F. Aharonian, "TeV gamma rays from BL Lac objects due to synchrotron radiation of extremely high energy protons," New Astronomy **5**, 377 (2000).

[41] A. Mücke, R. J. Engel, R. Rachen, et al., "BL Lac objects in the synchrotron proton blazar model," Astroparticle Physics **18**, 593 (2007).

[42] P. Reig, " Be/X-ray binaries," Ap&SS **332**, 1R (2011).

[43] I. F. Mirabel, "Gamma-ray binaries," Ap&SS **309**, 267 (2007)F. Aharonian, A.G. Akhperjanian, A.R. Bazer-Bachi, et al., (H.E.S.S. Collaboration), "Primary particle acceleration above 100 TeV in the shell-type supernova remnant RX J1713.7-3946 with deep HESS observations," A&A **464**, 235 (2007).

[44] A. Kawachi, T. Naito, and J. R. Patterson, "A Search for TeV Gamma-Ray Emission from the PSR B1259-63/SS 2883 Binary System with the CANGAROO-II 10 Meter Telescope," ApJ **607**, 949 (2004).

[45] R. H. D. Corbet and M. Kerr, "Hunting for New Gamma-ray Binaries - Technique Development," Proceedings of the 2009 Fermi Symposium **eConf Proceedings C091122**, arXiv:1001.471 (2010).

[46] P. C. Gregory, "Bayesian Analysis of Radio Observations of the Be X-Ray Binary LS I +61 303 ," ApJ **575**, 4 (2002).

[47] F. Aharonian, A.G. Akhperjanian, A. R. Bazer-Bachi, et al., (H.E.S.S. Collaboration), "3.9 day orbital modulation in the TeV γ-ray flux and spectrum from the X-ray binary LS 5039," A&A **460**, 743 (2006).

[48] J. Casares, M. Ribó, and I. Ribas, "A possible black hole in the γ-ray microquasar LS 5039," MNRAS **365**, 899 (2005).

[49] T. Piron, "The physics of gamma-ray bursts," Reviews Of Modern Physcis **76**, (2005).

[50] F. Aharonian, A.G. Akhperjanian, K. Aye, et al., (H.E.S.S. Collaboration), "Discovery of the binary pulsar PSR B1259-63 in very-high-energy gamma rays around periastron with HESS," A&A **442**, 1 (2005).

[51] F. Aharonian, A.G. Akhperjanian, K. Aye, et al., (H.E.S.S. Collaboration), "Energy dependent γ-ray morphology in the pulsar wind nebula HESS J1825-137," A&A **460**, 365 (2006).

[52] W. Cui and A. Konopelko, "Chandra View of the Unidentified TeV Gamma-Ray Source HESS J1804-216," ApJ **665**, L83 (2007).

[53] C. Chang, A. Konopelko, and W. Cui, "Search for Pulsar Wind Nebula Associations with Unidentified TeV γ-Ray Sources ," ApJ **682**, 1177 (2008).

[54] A. Atoyan, J. Buckley, and H. Krawczynski, "A Gamma-Ray Burst Remnant in Our Galaxy: HESS J1303-631," ApJ Letters **642**, L153 (2006).

[55] D. Lynden-Bell and M. J. Rees, "On quasars, dust and the galactic centre," MNRAS **152**, 461 (1959).

[56] B. Balick and R. L. Brown, "Intense sub-arcsecond structure in the galactic center," ApJ **194**, 265 (1959).

[57] R. L. Brown, "Precessing jets in Sagittarius A - Gas dynamics in the central parsec of the galaxy," ApJ **262**, 110 (1982).

[58] R. L. Brown, K. J. Johnston, and K. Y. Lo, "High resolution VLA observations of the galactic center," ApJ **250**, 155 (1981).

[59] R. L. Brown, K. J. Johnston, and K. Y. Lo, "High resolution VLA observations of the galactic center," ApJ **250**, 155 (1981).

[60] D. M. Watson, J. W. V. Storey, C. H. Townes, et al., "Far-infrared /O III/ and /N III/ line emission from galactic H II regions and planetary nebulae," A&A **250**, 605 (1981).

[61] F. K. Baganoff, Y. Maeda, M. Morris, et al., "Chandra X-Ray Spectroscopic Imaging of Sagittarius A* and the Central Parsec of the Galaxy," A&A **591**, 891 (2003).

[62] A. M. Ghez, S. Salim, N. N. Weinberg, et al., "Measuring Distance and Properties of the Milky Way's Central Supermassive Black Hole with Stellar Orbits," A&A **689**, 1044 (2008).

[63] S. Gillessen, F. Eisenhauer, S. Trippe, et al., "Monitoring Stellar Orbits Around the Massive Black Hole in the Galactic Center," A&A **629**, 1075 (2009).

[64] G. Becklin and E. E. Neugebauer, "2.2-micron map of the central 1 deg of the galactic center ," PASP **90**, 657 (1978).

[65] M. J. Reid, "The distance to the center of the Galaxy," ARA&A **31**, 345 (1993).

[66] G. C. Bower, H. Falcke, R. M. Herrnstein, et al., "Detection of the intrinsic size of Sagittarius A* through closure amplitude imaging," Science **304**, 704 (2004).

[67] S. Doeleman, J. Weintroub, A. Rogers, et al., "Event-horizon-scale structure in the supermassive black hole candidate at the Galactic Centre," Nature **455**, 78 (2008).

[68] Z. Q. Shen, K. Y. Lo, M. C. Liang, et al., " A size of 1 AU for the radio source Sgr A* at the centre of the Milky Way," Nature **438**, 62 (2005).

[69] M. J. Reid, K. M. Menten, R. Genzel, et al., "The Position, Motion, and Mass of Sgr A*," Astronomische Nachrichten **Supplementary Issue 1,**, 505 (2003).

[70] F. Yuan, Z. Q. Shen, and L. Huang, "Testing the Radiatively Inefficient Accretion Flow Model for Sagittarius A* Using the Size Measurements," ApJ **642**, 45 (2006).

[71] J. Cuadra, S. Nayakshin, and V. Sprinkle, "Galactic Centre stellar winds and Sgr A* accretion," MNRAS **366**, 358 (2006).

[72] A. Eckart, R. Schödel, M. García-Marín, et al., "Simultaneous NIR/sub-mm observation of flare emission from Sagittarius A*," Nature **492**, 337 (2008).

[73] R. Narayan and I. Yi, "Advection-dominated Accretion: Underfed Black Holes and Neutron Stars," ApJ **452**, 710 (1995).

[74] F. Yuan, E. Quataert, and R. Narayan, "Nonthermal Electrons in Radiatively Inefficient Accretion Flow Models of Sagittarius A*," Rev. Mod. Phys. **598**, 301 (2003).

[75] H. Falcke and S. Markoff, "The jet model for Sgr A*: Radio and X-ray spectrum," A&A **362**, 113 (2000).

[76] F. Yuan, S. Markoff, and H. Falcke, "A Jet-ADAF model for Sgr A*," A&A **383**, 854 (2002).

[77] A. Miyazaki, T. Tsutsumi, and M. Miyoshi, "Flares of Sagittarius A* at Multimeter Wavelengths," , ArXivAstrophysics e-prints:astro-ph/0512625 (2005).

[78] R. Genzel, T. O. Schodel, and A. Eckart, "Near-infrared flares from accreting gas around the supermassive black hole at the Galactic Centre," Nature **425**, 934 (2003).

[79] A. Eckart, F. K. Baganoff, and R. Schödel, "The flare activity of Sagittarius A*. New coordinated mm to X-ray observations," A&A **450**, 535 (2006).

[80] D. Porquet, N. Grosso, and P. Predehl, "X-ray hiccups from Sagittarius A* observed by XMM-Newton. The second brightest flare and three moderate flares caught in half a day," A&A **488**, 549 (2008).

[81] F. Yusef-Zadeh, H. Bushouse, and C. D. Dowell, "A Multiwavelength Study of Sgr A*: The Role of Near-IR Flares in Production of X-Ray, Soft γ-Ray, and Submillimeter Emission," ApJ **644**, 198 (2006).

[82] F. Yusef-Zadeh, M. Wardle, and C. Heinke, "Simultaneous Chandra, CSO, and VLA Observations of Sgr A*: The Nature of Flaring Activity," ApJ **682**, 361 (2008).

[83] A. Eckart, M. García-Marín, S. N. Vogel, et al., "Millimeter to X-ray flares from Sagittarius A*," A&A **537**, 52 (2012).

[84] N. Degenaar, J. M. Miller, J. Kennea, et al., "he X-Ray Flaring Properties of Sgr A* during Six Years of Monitoring with Swift," ApJ **769**, 155 (2013).

[85] G. Ponti, B. De Marco, M. R. Morris, et al., "Fifteen years of XMM-Newton and Chandra monitoring of Sgr A*: Evidence for a recent increase in the bright flaring rate," arXiv:150702690P (2015).

[86] M. Chernyakova, D. Malyshev, F. Aharonian, et al., "The high-enbergy, arcminute-scale galactic center gamma-ray source," ApJ **726**, 60 (2011).

[87] F. Aharonian, A.G. Akhperjanian, K.M. Aye, et al., (H.E.S.S. Collaboration), "Very high energy gamma rays from the direction of Sagittarius A*," A&A **425**, 13 (2004).

[88] F. Aharonian, A.G. Akhperjanian, G. Anton, et al., (H.E.S.S. Collaboration), "Spectrum and variability of the Galactic center VHE γ-ray source HESS J1745-290," A&A **503**, 817 (2009).

[89] F. Aharonian, A.G. Akhperjanian, U. Barres de Almeida, et al., (H.E.S.S. Collaboration), "Simultaneous HESS and Chandra observations of Sagitarius A* uring an X-ray flare," A&A **492**, 25 (2008).

[90] S. Gillessen, R. Genzel, T. K. Fritz, et al., "A gas cloud on its way towards the supermassive black hole at the Galactic Centre," Nature **481**, 51 (2012).

[91] A. Burkert, M. Schartmann, and C. Alig, "Physics of the Galactic Center Cloud G2, on its Way towards the Super-Massive Black Hole," ApJ **750**, 58 (2012).

[92] M. Schartmann, A. Burkert, C. Alig, et al., "Simulations of the Origin and Fate of the Galactic Center Cloud G2," ApJ **755**, 155 (2012).

[93] J. Guillochon, A. Loeb, and M. MacLeod, "Possible Origin of the G2 Cloud from the Tidal Disruption of a Known Giant Star by Sgr A*," ApJ **786**, 12 (2014).

[94] R. A. Murray-Clay and A. Loeb, "Disruption of a proto-planetary disc by the black hole at the milky way centre," Nature Communication **3**, 1049 (2012).

[95] J. Miralda- Escudé, "A Star Disrupted by a Stellar Black Hole as the Origin of the Cloud Falling toward the Galactic Center," ApJ **756**, 86 (2012).

[96] R. Narayan, F. Özel, and L. Sironi, "Radio Synchrotron Emission from a Bow Shock around the Gas Cloud G2 Heading toward the Galactic Center," ApJ **757**, 20 (2012).

[97] T. Saitoh, J. Makino, and Y. Asaki, "Flaring up of the Compact Cloud G2 during the Close Encounter with Sgr A* in Summer 2013," PASJ **66**, 1 (2014).

[98] F. Yusef-Zadeh and M. Wardle, "Signatures of an Encounter Between the G2 Cloud and a Jet from Sgr A," ApJ **770**, 21 (2013).

[99] P. Anninos, P. C. Fragile, and J. Wilson, "3D Moving-Mesh Simulations of Galactic Center Cloud G2," ApJ **759**, 132 (2012).

[100] S. Gillessen, R. Genzel, and T. K. Fritz, "New Observations of the Gas Cloud G2 in the Galactic Center," ApJ **763**, 78 (2013).

[101] K. Phifer, T. Do, and L. Meyer, "Keck Observations of the Galactic Center Source G2: Gas Cloud or Star?," ApJ **773**, 13 (2013).

[102] S. Gillessen, R. Genzel, and T. K. Fritz, "Pericenter Passage of the Gas Cloud G2 in the Galactic Center," ApJ **774**, 44 (2013).

[103] J. L. Hora, G. Witzel, and M. L. Ashby, "SPITZER/IRAC OBSERVATIONS OF THE VARIABILITY OF Sgr A* AND THE OBJECT G2 AT 4.5 μm," ApJ **793**, 120 (2014).

[104] M. Tsuboi, Y. Asaki, and O. Kameya, "No Microwave Flare of Sagittarius A* around the G2 Periastron Passing," ApJ **798**, 6 (2015).

[105] G. C. Bower, S. Markoff, and J. Dexter, "Radio and Millimeter Monitoring of Sgr A*: Spectrum, Variability, and Constraints on the G2 Encounter," ApJ **802**, 69 (2015).

[106] G. Witzel, A. Ghez, and M. Morris, "G2's closest approach to the Galactic Center black hole," AAS **225**, 102 (2015).

[107] Y. Clay, "Pair production and bremsstrahlung of charged leptons," Rev. Mod. Phys. **46**, 4 (1974).

[108] W. Heitler, *The Quantum Theory of Radiation*, 3rd ed. (Oxford University Press, London, 1954).

[109] K. Bernlohr, "Monte Carlo images of air shower, http://www.mpi-hd.mpg.de/hfm/ bernlohr/HESS" (2000).

[110] I. E. Tamm and I. M. Frank, "Coherent Radiation of Fast Electrons in a Medium," Doklady AN SSSR **14**, 109 (1937).

[111] T. C. Heitler, *Very High Energy Gamma-Ray Astronomy*, 3rd ed. (IOP Publishing, Bristol, 2003).

[112] V. Fonseca, "Status and Results from the HEGRA Air Shower Experiment," Ap&SS **263**, 377 (1998).

[113] D. Berg, *A detailed study of the gamma-ray supernova remnant RX J1713.7-3946 with HESS*, Diploma thesis, University of Heidelberg, Heidelberg (2006).

[114] M. Wiedner, *Atmospheric Water Vapour and Astronomical Millimetre Interferometry* , Diploma thesis, University of Cambridge, Cambridge (1998).

[115] M. Cornils and E. Gillessen, "The optical system of the H.E.S.S. imaging atmospheric Cherenkov telescopes. Part II: mirror alignment and point spread function," Astroparticle Physics **20**, 129 (2003).

[116] P. Vincent, J. P. Denaca, J. F. Huppert, et al., "Performance of the H.E.S.S. Cameras," Proceedings of the 28th International Cosmic Ray Conference , 2887 (2003).

[117] S. Funk, G. Hermann, J. Hinton, et al., "The trigger system of the H.E.S.S. telescope array," Astroparticle Physics **22**, 285 (2004).

[118] C. Borgmeier, N. Komin, M. de Naurois, et al., "The Central Data Acquisition System of the H.E.S.S. Telescope System," Proceedings of the 28th International Cosmic Ray Conference , 2891 (2003).

[119] A. Balzer, M. Füβling, M. Gajdusc, et al., "The H.E.S.S. Central Data Acquisition System," Astroparticle Physics **54**, 67 (2007).

[120] M. de Naurois, *Ouverture d'une nouvelle fenêtre astronomique sur l'Univers non thermique*, Diploma thesis, Ecole polytechnique, Cedex (2012).

[121] J. Hillas, "Cerenkov light images of EAS produced by primary gamma," International Cosmic Ray Conference 3 , 445 (1985).

[122] S. Funk, *A new population of very high-energy γ-ray sources detected with H.E.S.S. in the inner part of the Milky Way*, Diploma thesis, University of Heidelberg, Heidelberg (2005).

[123] S. Ohm, C. van Eldik, and K. Egberts, "γ/hadron separation in very-high-energy c-ray astronomy using a multivariate analysis method," AStroparticle Physics **31**, 383 (2009).

[124] A. Hoecker, P. Speckmayer, and J. Stelzer, "TMVA - Toolkit for Multivariate Data Analysis," ArXiv Physics e-prints , (2007).

[125] L. Breiman, J. Friedman, and C. J. Stone, "Classification and Regression Trees," Rev. Mod. Phys. **Wadsworth**, Stamford (1984).

[126] D. Bowser-Chao and D. L. Dzialo, "Comparison of the use of binary decision trees and neural networks in top-quark detection," Phys. Rev. D **47**, 1900 (1993).

[127] T. P. Li and Y. Q. Ma, "Analysis methods for results in gamma-ray astronomy," ApJ **272**, 317 (1983).

[128] G. Rowell, "A new template background estimate for source searching in TeV gamma -ray astronomy," A&A **410**, 389 (2003).

[129] W. A. Rolke, A. M. López, J. Conrad, et al., "Limits and confidence intervals in the presence of nuisance parameters," NIMPA **551**, 493 (2005).

[130] F. Brun, *echerche de sources ténues ou transitoires dans les régions centrales de la Galaxie avec H.E.S.S. Application à l'étude de la région du vestige de supernova W49B.. High Energy Astrophysical Phenomena*, Diploma thesis, Université Pierre et Marie Curie - Paris VI,< tel-00645861>, Paris (2011).

[131] J. Prahl, "A fast unbinned test on event clustering in Poisson processes," arXiv:astro-ph/9909399 , (1999).

[132] W. A. Taylor , "Change-Point Analysis:A Powerful New Tool For Detecting Changes, http://www.variation.com/cpa/tech/changepoint.html" .

[133] A. O'Faoláin de Bhróithe for the VERITAS Collaboration , "A search for short-term variability in the very high energy γ-ray emission from the Crab nebula," arXiv:1210.3723 (2012).

[134] J. Hahn, "Ensuring long-term stability of data quality selection for H.E.S.S. under challenging atmospheric conditions," H.E.S.S. internal note **75**, 96 (2012).

[135] F. Aharonian, A. G. Akhperjanian, A. R. Bazer-Bachi, et al., (H.E.S.S. Collaboration), "Observations of the Crab nebula with HESS," A&A **457**, 899 (2006).

[136] F. Aharonian, A. G. Akhperjanian, G. Anton, et al., (H.E.S.S. Collaboration), "Spectrum and variability of the Galactic center VHE γ-ray source HESS J1745-290," A&A **503**, 817 (2009).

[137] A. Abramowski, F. Aharonian, F. Ait Benkhali, et al., (H.E.S.S. Collaboration), "Diffuse Galactic gamma-ray emission with H.E.S.S.," PhRvD **90**, 122007 (2014).

[138] S. Liu, F. Melia, F. Petrosian, et al., "Stochastic Acceleration in the Galactic Center HESS Source," ApJ **647,** 1099 (2006).

[139] F. Aharonian and A. Neronov, "High-Energy Gamma Rays from the Massive Black Hole in the Galactic Center," ApJ **619,** 306 (2005).

[140] A. Atoyan and C. Dermer, "TeV emission from the Galactic center black hole plerion," ApJ **617,** 123 (2004).

[141] Q. D. Wang, F. L. Lu, and E. V. Gotthelf, "G359.95-0.04: an energetic pulsar candidate near Sgr A*," MNRAS **367**, 937 (2006).

[142] J. Hinton and F. Aharonian, "Inverse Compton Scenarios for the TeV Gamma-Ray Emission of the Galactic Center," ApJ **657,** 302 (2007).

[143] M. Kusunose and F. Takahara, "A leptonic model of steady high-energy gamma-ray emission from Sgr A*," ApJ **748,** 34 (2012).

[144] F. Aharonian, A. G. Akhperjanian, A. R. Bazer-Bachi, et al., (H.E.S.S. Collaboration), "HESS Observations of the Galactic Center Region and Their Possible Dark Matter Interpretation," PhRvL **97**, 1102 (2006).

[145] C. van Eldik, O. Bolz, and I. Braun, "Localising the H.E.S.S. Galactic Centre point source," arXiv:0709.3729 , (2007).

[146] K. Ferriére, "Interstellar gas within 10 pc of Sagittarius A*," A&A **540**, 50 (2012).

[147] A. Abramowski, F. Acero, F. Aharonian, et al., (H.E.S.S. Collaboration), "Search for a Dark Matter Annihilation Signal from the Galactic Center Halo with H.E.S.S.," PhRvL **106p**, 1301 (2011).

[148] S. Funk and J. Hinton, "Comparison of Fermi-LAT and CTA in the region between 10–100 GeV ," Astroparticle Physics **43,** 348 (2013).

[149] M. Actis, G. Agnetta, F. Aharonian, et al., (CTA Consortium), "Design concepts for the Cherenkov Telescope Array CTA: an advanced facility for ground-based high-energy gamma-ray astronomy," Experimental Astronomy **32**, 193 (2011).

[150] B. S. Acharya, M. Actis, T. Aghajani, et al., (CTA Consortium), "Introducing the CTA concept," Astroparticle Physics **43**, 3 (2013).

[151] "https://portal.cta-observatory.org/" .

[152] "http://sites.nationalacademies.org/bpa/BPA049810"
.

Acknowledgements

Thank God! I finally completed my PhD thesis.

The first person to thank is always Chan Yuen Han, though she doesn't know about it. During my PhD study, many thanks to little Tianzi for sharing everyday life. Thanks to little Miss Poon for spicing up my life with fights. My gratitude to Yeung Kwai Fook for hearing me out whenever I need.

Thanks a lot to Aion, Nachi and Francois who offered valuable help to my work. Thanks to everyone in the group and my other friends in the institute and Heidelberg. You made my life more meaningful here.

Special thanks to those who have run with me. My life here would be very different without you. You helped me achieve each of my marathon day dreams.